Physical Environmental Electrochemistry: Electrochemical Properties of Natural Organic Matter and Iron Powders

James Thomas Nurmi
B.A., Gustavus Adolphus College, 1997

A dissertation presented to the faculty of the
OGI School of Science & Engineering,
Oregon Health & Science University,
in partial fulfillment of the
requirements for the degree
Doctor of Philosophy
in
Environmental Science and Engineering

October 2005

This dissertation "Physical Environmental Electrochemistry: Electrochemical Properties of Natural Organic Matter and Iron Powders" by James T. Nurmi has been examined and approved by the following Examination Committee:

Dr. Paul G. Tratnyek, Dissertation Advisor
Professor

Dr. Richard L. Johnson
Professor

Dr. James E. Amonette
Research Scientist
Pacific Northwest National Laboratory

Dr. William Fish
Professor
Portland State University

ACKNOWLEDGEMENTS

I would like to give the most genuine recognition and appreciation to my advisor Dr. Paul G. Tratnyek for allowing me to pursue my research interests. His ability to balance guidance with what his student's interests are is a wonderful and productive model which I will take wherever I go. There have been many PhD, masters, college, high school students, professors and high school teachers, and friends in the lab throughout the last several years that have impacted my life in different ways. I would like to acknowledge one person in particular for his friendship and guidance on many of life's intricacies. Thank you Dr. Joel Z. Bandstra.

DEDICATION

I would like to dedicate this to my family, Amber and my son, James Daniel Nurmi.

Table of Contents

Acknowledgements ii
Dedication iii
Table of Contents iv
List of Tables vii
List of Figures viii
Abstract xi

Section 1.0. **Overview of Physical Environmental Electrochemistry** 1
1.1. Environmental Processes 2
1.1.1. Complex Environmental Systems 3
1.2. Principles of Electrochemistry 3
1.2.1. Electrochemical Techniques 8
1.2.1.1. Voltammetry 9
1.2.1.2. Qualitative Voltammetry 10
1.2.1.3. Quantitative Voltammetry 11
1.3. Applications of Physical Environmental Electrochemistry 13
1.3.1. Electrochemical Properties of NOM and Fractions of NOM 13
1.3.2. Iron-H_2O-Contaminant Electrochemistry 18
1.4. References 22
Section 2.0. **Electrochemical Properties of Natural Organic Matter (NOM), Fractions of NOM, and Model Biogeochemical Electron Shuttles** 34
2.1. Cyclic Voltammetry of NOM with Macorelectrodes 34
2.1.1. Abstract 34
2.1.2. Introduction 35
2.1.3. Experimental Section 37
2.1.4. Results and Discussion 39
2.1.4.1. Qualitative CV of NOM 39
2.1.4.2. Quantitative CV of NOM 42

2.1.4.3. CV of Model Compounds 44
2.1.5. Correlation Analysis 45
2.1.6. Implications 47
2.1.7. Acknowledgements 48
2.1.8. References 50
2.1.9. Supporting Information 65
2.2. Square wave and Cyclic Voltammetry with Microelectrodes 79
2.2.1. Abstract 79
2.2.2. Introduction 79
2.2.3. Material and Methods 81
2.2.4. Results and Discussion 82
2.2.5. Acknowledgements 84
2.2.6. References 85
Section 3.0. **Electrochemical Properties of Micron and Nano Sized Iron Powders** 96
3.1. Packed Powder Electrodes for Characterizing the Reactivity of Iron Powders in Borate Solutions 96
3.1.1. Abstract 96
3.1.2. Introduction 97
3.1.3. Experimental 99
3.1.4. Results and Discussion 102
3.1.4.1. Preliminary Characterization 102
3.1.4.2. Effect of Rotation Rate 103
3.1.4.3. Varying Cavity Volume 104
3.1.4.4. Estimating Current Density 105
3.1.4.5. Implications 106
3.1.4.6. Acknowledgements 107
3.1.5. References 108
3.2. Characterization and Properties of Metallic Iron and Iron-Oxide Nanoparticles: Spectroscopy, Electrochemistry, and Kinetics 121

3.2.1. Abstract 121
3.2.2. Introduction 122
3.2.3. Experimental 125
3.2.4. Results and Discussion 130
3.2.5. Implications 139
3.2.6. Acknowledgements 140
3.2.7. References 141
3.2.8. Supporting Information 161
Biographical Sketch 171

LIST OF TABLES

Table 1.1. Electrochemical parameters used in voltammetric studies of NOM and fractions of NOM 27

Table 1.2. Electrochemical parameters used in electrochemical studies of Fe-H_2O-contaminant systems 28

Table 2.1. Summary of electrochemical data. 56

Table 2.2. Summary of NOM properties. 57

Table 2.3. Electrochemical parameters used in voltammetric studies of NOM. 88

Table 3.1. Supplier characteristics of iron particles. 148

Table 3.2. Summary of physical properties. 149

Table 3.3. Particle surface compositions determined by XPS. 150

Table 3.4. Mass balance data for CT and products. 151

LIST OF FIGURES

Figure 1.1. Possible biogeochemical electron transfer pathways of NOM. 29

Figure 1.2. General pathways of an electrode reaction... 30

Figure 1.3. Three examples of cyclic voltammograms of NOM under different conditions.. 31

Figure 1.4. The columns represent a division of NOM grouping based on the qualitative shape of the voltammogram (Nurmi, 2002 32

Figure 1.5. Redox ladder showing possible electrons donors, mediator and acceptors. 33

Figure 2.1. Chemical structures of NOM model quinones.....58

Figure 2.2. CVs of NOM-PP under nonaqueous conditions in (A) DMF and (B) DMSO.....59

Figure 2.3. CVs of (A) NOM-GT and (B) NOM-CH. 60

Figure 2.4. Effect of (A) scan rate and (B) concentration on CVs of NOM-PP. 61

Figure 2.5. Rotating disk electrode experiment. 62

Figure 2.6. CVs of (A) AQDS and (B) menadione. 63

Figure 2.7. Redox ladder. Figure based on values in Table 1. 64

Figure 2.8 Voltammetry of the model compound, menadione.....89

Figure 2.9. Voltammetry of NOM-GT.....90

Figure 2.10. Voltammetry of NOM-PP.....91

Figure 2.11. All NOM and NOM fractions with all electrochemical techniques. 92

Figure 2.12. Peak potentials for all NOM and NOM model compounds for all Echem techniques. 93

Figure 2.13. Reference electrode potentials showing how the Fc/Fc^{+} relates to standard reference electrode potentials (SHE).....94

Figure 2.14. Redox ladder showing possible electrons donors, mediator and acceptors.. 95

Figure 3.1. Diagram of the exterior and interior dimensions of the powder disk electrode (PDE) developed for use in this study. 114

Figure 3.2. Current vs. potential plot of anodic polarization curves for conventional stationary disk electrodes ($SD_{Fe}E$ and $SD_{Pt}E$), and two stationary powder disk electrodes ($SP_{FeIc}D_{Fe}E$ and $SP_{FeIc}D_{Pt}E$) in anaerobic aqueous borate (pH = 8.4, 0.19 M). 115

Figure 3.3. Current vs. potential plot of anodic polarization curves for conventional rotating disk electrodes ($RD_{Fe}E$ and $RD_{Pt}E$), and two rotating powder disk electrodes ($RP_{FeIc}D_{Fe}E$ and $RP_{FeIc}D_{Pt}E$) in anaerobic aqueous borate (pH = 8.4, 0.19 M).....116

Figure 3.4. Current vs. potential plot of anodic polarization curves for the $RP_{FeIc}DE$ in anaerobic aqueous borate (pH = 8.4, 0.19 M) and various rotation rates.....117

Figure 3.5. A. Current vs. potential plot of anodic polarization curves for the $RP_{FeIc}DE$ in anaerobic aqueous borate (pH = 8.4, 0.19 M) using various amounts of iron powder under stationary conditions (0 rpm). Scan rate = 0.1 mV/s. B. Same data plotted as log absolute current vs. potential.....118

Figure 3.6. A. Current vs. potential plot of anodic polarization curves for the $RP_{FeIc}DE$ in anaerobic aqueous borate (pH = 8.4, 0.19 M) using various amounts of iron powder under hydrodynamic conditions (3000 rpm). Scan rate = 0.1 mV/s. B. Same data plotted as log absolute current vs. potential.....119

Figure 3.7. A. Current density ($\mu A\ cm^{-2}$) vs. potential plot of anodic polarization curves for the $RP_{FeIc}DE$ in anaerobic aqueous borate (pH = 8.4, 0.19 M) under stationary conditions (0 rpm). Scan rate = 0.1 mV/s. B. Current density (μA cm-2) vs. potential plot of anodic polarization curves for the $RP_{FeIc}DE$ in anaerobic aqueous borate (pH = 8.4, 0.19 M) under hydrodynamic conditions (3000 rpm). Scan rate = 0.1 mV/s. 120

Figure 3.8. TEMs of Fe^{H2}. (A) Low magnification image of as-received sample, (B) Higher resolution of image of irregularly-shaped metal particle, (C) Higher resolution image of oxide shell around metal particle, (D) Low resolution image of flash-dried sample. 152

Figure 3.9. TEMs of Fe^{BH}. (A) Low magnification image of as-received sample, (B) Higher resolution image of metal particle, (C) Dark field image of metal particle highlighting small metal crystallites in particle, (D) Low resolution image of flash-dried sample. (E) Higher resolution image of flash-dried sample showing spreading of coating layer between particles. 156

Figure 3.10. Log absolute current vs. potential plot from anodic polarization of stationary powder disk electrodes packed with various iron and iron oxide powders. At scan rate = 0.1 mV/s in anoxic aqueous borate (pH = 8.4).....157

Figure 3.11. Surface area normalized rate constants (k_{SA}) vs. mass load normalized rate constants (k_M), for disappearance of benzoquinone (BQ) in batch experiments. Diagonal lines are contours for representative values of ρ_a ($m^2\ g^{-1}$). For both types of nano-Fe^0, k_{SA} is shown for high and low ρ_a values (given in the legend). High values of ρ_a are from Table 1, Low values or ρ_a are BET measurements from this study. The resulting ranges of rate constants are shaded. 158

Figure 3.12. Surface area normalized rate constants vs. mass load normalized rate constants, for the disappearance of carbon tetrachloride (CT). Diagonal lines are contours for representative values of ρ_a ($m^2\ g^{-1}$). For both types of nano-Fe^0, k_{SA} is shown for high and low ρ_a values (given in the legend). High values of ρ_a are from Table 1, Low values or ρ_a are BET measurements from this study. The resulting ranges of rate constants are shaded. 159

Figure 3.13. Yield of chloroform (Y_{CF}) vs. iron type (Fe^{EL}, Fe^{BH}, Fe^{H2}). The range of Y_{CF} for each iron type reflects the wide range of experimental conditions tested (pH, buffer, age and handling of the iron, etc.). 160

Abstract

Physical Environmental Electrochemistry: Electrochemical Properties of Natural Organic Matter and Iron Powders

James T. Nurmi

OGI School of Science and Engineering, 2005

Supervising Professor: Paul G. Tratnyek

Electron transfer is ubiquitous in nature. A thorough understanding of the rates and mechanisms of electron transfer is vital to the scientific study of natural systems. It is also important for the successful design and implementation of engineered systems that rely on electron transfer (i.e., permeable reactive barriers filled with Fe^0). Since electrochemistry is the science that deals with the relationship between electricity and chemical changes, it is well suited for the study of systems in which electron transfer is important. This dissertation details the electrochemical study of two important, and different environmental systems.

The first part of this dissertation deals with the redox properties of natural organic matter (NOM), fractions of NOM, and model biogeochemical electron shuttles. Several electrochemical techniques and experimental designs were adapted in order to obtain the best resolution of voltammograms of NOM. The peak potentials for various NOM fractions were collected and related to various electron donors and electron acceptors, given as a redox ladder. A significant result of this study was the observation that the voltammogram of an unfractionated NOM sample gave several peaks, indicating that several redox active species or moieties are present in the sample. This led us to

hypothesize that there may be a continuum of potentials associated with redox active groups in NOM.

The second environmental system that was studied in this dissertation was that of the Fe^0-H_2O-contaminant system. Much work has been done on characterizing the rates and mechanisms of how Fe^0 reduces various contaminants. Most of these studies use high grade iron or polished Fe^0 disk/coupon/wire electrodes. While these studies have provided a great deal of understanding of this system, the rates and mechanisms of iron mediated reduction by particles used in the field may be different. In order to get at important aspects of this system that are not represented in batch or column experiments, we designed, fabricated, and validated a powder disk electrode (PDE) that is able to hold various sizes of iron particulate (micro to nano).

In order to determine if our PDE would give electrochemically interpretable results, we started by packing the PDE with electrolytic Fe^0 (FeIc). We found that by varying scan rate, rotation rate, and cavity volume: (i) the resulting voltammogram was due to the iron powder, not the underlying disk material, (ii) the cathodic reaction ($2H^+ + 2e^- \rightarrow H_2(g)$) is kinetically limited, and (iii) iron dissolution is affected by the mass transport of solutes (probably Fe^{2+}) out of the cavity pore space.

For the study of nano-iron powders (Fe^{H2}, Fe^{BH}), we combined batch, spectroscopic and electrochemical approaches to characterize the properties of these nano iron samples. Fe^{H2} is a two-phase material consisting of 40 nm α-Fe^0 (made up of crystals approximately the size of the particles) and Fe_3O_4 particles of similar size or larger containing reduced sulfur; whereas Fe^{BH} is mostly 20-80 nm metallic Fe particles (aggregates of <1.5 nm grains) with an oxide shell/coating that is high in oxidized boron. The Fe^{BH} particles further aggregate into chains. We found that both nano iron samples with Fe^0 cores gave more cathodic corrosion potentials (E_{corr}'s) than either the polished iron disk or the PDE packed with Fisher electrolytic iron.

Section 1.0. Overview of Physical Environmental Electrochemistry

The term environmental electrochemistry has been used in a variety of scientific and engineering contexts. For the purposes of this chapter, several examples of environmental electrochemical studies from various fields will be given in order to highlight the differences between engineering applications of electrochemistry, analytical environmental electrochemistry, and physical environmental electrochemistry.

Engineering applications range from electrolysis of various organic and inorganic substances to a relatively new environmental technology called electrokinetics. Electrolysis uses the passing of a current through a conductive solution in order to change, usually decompose, a substance in solution. There have been many studies, dating back to the pioneers of electrochemistry, in which electrolysis was used to decompose or make compounds in solutions for either remediation or commercial purposes A recent example of electrolysis for remediation is the decomposition of TNT in water by using various types of cathode materials [1].

Electrokinetic remediation involves the application of either a direct current or an electric potential to a system in order to create an electric field between two electrodes in a contaminated sample. The mechanisms of contaminant removal induced by applying a potential or current between electrodes include transport, sorption, precipitation, dissolution, and electrolysis [2-4].

In contrast to the engineering applications above, electrochemical techniques can also be used to determine the composition or properties of environmental systems. In the

sub-discipline of analytical chemistry, a collection of techniques designed and used to determine the composition of a given sample. For instance, analytical environmental electrochemistry has the intent to develop techniques to measure the composition of a soil, sediment, or water sample. Much progress has been made on the fabrication of electrodes and design of electrochemical systems that allow for the determination of various compounds, such as metals, in soils, sediments, and waters [5-8].Thus, electrochemical techniques are well suited for determining concentrations of species in various environmentally relevant systems.

Physical chemistry often focuses on the determination of the thermodynamic or kinetic properties of materials, including electrochemical potentials and reaction rate constants. Physical environmental electrochemistry often must also contend with the complexity of environmental systems. While the majority of environmental electrochemical studies fall under the purview of analytical chemistry, comparatively few studies have used electrochemistry to probe the physico-chemical properties of natural systems. Most of those that have been published to date are reviewed in this chapter.

The following sections are intended to educate the reader on the principles of: (i) electrochemistry, (ii) complex environmental processes, and (iii) physical environmental electrochemistry. This will be accomplished with several examples that combine the techniques and theory of electrochemistry in order to better understand the properties and processes of complex environmental systems.

1.1. Environmental Processes

The majority of environmental reactions that take place under aqueous conditions are either oxidation-reduction (redox), hydrolysis, or acid-base reactions [9]. Of these three, this chapter is mainly concerned with redox reactions. Redox reactions can be broken into two categories: oxidation and reduction. These two categories will be discussed and are accompanied with simplified examples.

1.1.1. Complex Environmental Systems

In nature, multiple oxidation, reduction, and electron shuttling reactions often occur together. Figure 1.1 exemplifies how redox reactions occur in an environmental system. The arrows in Figure 1.1 represent redox reactions. The oblong shape in the lower left represents an iron-reducing bacterium, such as *Geobacter metallireducens*. It has been demonstrated that this bacterium and various other bacteria can donate electrons to various species in solution or onto complexed compounds, such as U^{6+} [10]. Other studies have shown that these bacteria may also be able to donate electrons to moieties/species found in natural organic matter (NOM). The resulting reduced NOM may then reduce a compound such as Fe^{3+}(s) or possibly even U^{6+}(aq) depending on the redox potentials of the species in the NOM.

Electron transfer from abiotic systems has also been shown to be important in natural complex systems. The object in the upper right of Figure 1.1 represents an iron particle. The arrows in the upper right of Figure 1.1 show that Fe^0 reduces TNT to TAT in a complex set of mechanisms, and that NOM may react with Fe^0 in a similar manner as was discussed with the bacterium. Much work has been done on the mechanisms and kinetics of Fe^0 reduction of various contaminants, yet it is still not known why some iron particles behave differently than others.

In all cases, it is apparent that electron transfer is important in understanding how environmental systems function. Since electron transfer is the most important reaction mechanism in environmental systems, electrochemistry is well suited for the study of these complex systems. In the next section, a short introduction to the principles of electrochemistry will be given.

1.2. Principles of Electrochemistry

Electrochemistry is the study of electron transfer reactions between electrodes and reactant molecules usually in solution. Most electrochemical studies involve the development and application of techniques to probe the rate and mechanisms of various

reactions. Figure 1.2 shows the general pathways of a typical electrode reaction. Note that the mechanisms and processes are equivalent to those that are involved in redox reactions at environmental surfaces (Figure 1.1). Because of this, the use of electrochemical techniques is well suited to the study of complex environmental systems.

Figure 1.2 shows that an oxidant in the bulk solution (Ox_{bulk}) can diffuse into the interfacial region, potentially undergo chemical reactions, adsorb to the surface of the electrode, receive an electron from the electrode (become reduced), and then diffuse back out into the bulk solution. Note that the same processes occur between either a bacterium or a metal particle as shown in Figure 1.1.

In the case of a Pt electrode, in order for an electron transfer to occur, a substance in solution must be present that can either accept or donate an electron to/from the electrode. In the case where the electrode itself reacts, such as during corrosion of an Fe^0 electrode, the dissolution of Fe^0 to Fe^{2+} will cause a flow of electrons. These are two types of electrodes that have been used to study the properties, rates, and mechanisms of environmental systems.

Reactions at the electrode surface are heterogeneous and occur in the interfacial region between the electrode and solution where the charge distribution can be different than that of the bulk solution. This interfacial region can influence electrode processes, such as when adsorption of an organic substance occurs at the surface of an electrode. For most cases, this complexity is minimized by reducing the size of the interfacial region by addition of a supporting electrolyte and/or by rotating the electrode.

The electrode can act as either a sink (oxidation) or source (reduction) for electrons to or from species in solution, as in:

$$O + ne^- \rightarrow R \qquad (1)$$

Where O represents an oxidant and R represents a reductant. Electrochemical studies usually use inert working electrode materials such as Hg, Pt, Au, or glassy carbon.

Alternatively, if the working electrode is made of a material that undergoes corrosion processes, then the electrode itself will generate an electrochemical response, as in:

$$M \rightarrow M^{n+} + ne^- \quad (2)$$

Where M represents a metal and n is the number of electrons transferred.

The transfer of an electron to or from the electrode ultimately depends on the energy of the electron orbitals of the acceptor and donor. In the electrode, this is the highest filled orbital; in a metal, it is called the Fermi level [11]; and in a soluble species, it is the frontier orbital of the valence electron to be given or received. For a reduction or oxidation at an electrode, a minimum/maximum energy exists that the electrode must obtain before transfer can occur, which is often called an over-potential [12].

The pathways discussed above can arise in two ways depending on whether the electrode potential is allowed to come to equilibrium with the solution, as in equilibrium electrochemistry or whether the electrode potential is controlled, as in dynamic electrochemistry. In the former case, the potential established at an electrode under equilibrium conditions is given by the Nernst equation:

$$E = E^{0'} + RT/nF \ln[Ox]/[Red] \quad (3)$$

This equation describes the electrode potential (E) as a function of the standard redox potential ($E^{0'}$) and the concentrations of the oxidized and reduced forms of redox active substances in solution.

An experimental technique used frequently for the measurement of overall redox conditions (Eh or pE) in environmental systems usually employs an inert Pt electrode (or occasionally a C or Au electrode) in which the potential is left uncontrolled. Many investigations and publications have been devoted to the discussion of this type of study and in the validity and interpretation of the data [13]. The interpretation of Eh measurements is often difficult because of the complexity of environmental systems. In soils, sediments, and water, it is reasonable to believe that there exist multiple redox

labile compounds or moieties, many of which may not reach equilibrium with a Pt electrode.

When an electrode is placed in a solution that contains many redox active compounds, the resulting electrode potential will be a mixed potential. This potential is determined by not only the standard potentials of the various redox active compounds in solution but also the kinetics of these compounds reacting with the electrode surface. For instance, it has been shown that many redox active organic compounds react slowly with Pt electrode, thus the resulting measured potential may not be an accurate or meaningful representation of the redox conditions in the sample.

In electrolytic studies, the potential at the working electrode is held at a constant value that causes a current to flow. The current induces the exchange of electrons between the electrode and molecules in solution. The transfer of electrons can be in either direction, depending on the applied potential. For the reductive electrolysis of Fe^{3+} to Fe^{2+}, the magnitude of the current (i) is given by:

$$I = AFJ \qquad (4)$$

where,

A = the electrode area (cm^2)

F = Faraday constant (96,485 C mol^{-1})

J = the flux of Fe^{3+} reaching the electrode surface (moles cm^{-2} s^{-1})

This last term can be thought of as the quantity of material reacting at the electrode area per second. It can be related to traditional homogeneous rate constants: $j = k_0 [Fe^{3+}]_0$, where k_0 is the heterogeneous rate constant for the electron transfer reaction and $[Fe^{3+}]_0$ is the concentration of the reactant at the electrode surface. Note that the kinetics are assumed to be first order in Fe^{3+} concentration. By passing a current through the cell, thus reducing Fe^{3+} to Fe^{2+} at the electrode surface, a large difference arises between equilibrium electrochemistry and electrolysis. This results in a difference in Fe^{3+} concentration between the electrode surface and bulk solution. Because of this,

electrolytic currents may be dependant on the mass transport of reactants and products to or from the electrode surface, and/or the rate (k_0) of the heterogeneous electron transfer (kinetics) which is controlled by the electrode potential.

Dynamic electrochemistry is different from the above because the potential at the electrode surface is controlled and the resulting current response is measured. In the previous section, it was shown that the electrode kinetics can be controlled by the electrode potential (eq. 3). In dynamic electrochemistry, the potential is varied, thus the relationship between the heterogeneous rate constant for the electron transfer and the potential must be quantified.

The current for the oxidative and reductive half reactions is described by eq. 5 and 6.

$$i_c = FAk_{red}[O]_0 \tag{5}$$

$$i_a = FAk_{ox}[R]_0 \tag{6}$$

where $k_{red}[O]_0$ and $k_{ox}[R]_0$ are the fluxes of material to the electrode surface. The net current is the sum of both cathodic and anodic current, $i = i_a + i_c$, thus:

$$i = FA(k_{ox}[R]_o - k_{red}[O]_o) \tag{7}$$

It is usually assumed that electrodic reactions behave analogously to chemical rate processes and can therefore be described using the transition state model. Applying transition state theory gives the rate of the reduction reaction as:

$$k_{red} = k^0_{red}\exp(-\alpha F\eta/RT) \tag{8}$$

and the rate of the oxidation reaction as:

$$k_{ox} = k^0_{ox}\exp((1-\alpha)F\eta)/RT) \tag{9}$$

where α is the charge transfer coefficient, and η is the overpotential . By substituting these two equations into the net current equation, and assuming the solution is well mixed

so the bulk concentration equals the electrode surface concentration, we obtain the final relationship for the net current (i) at the working electrode:

$$i = i_0(\exp((1-\alpha)F\eta/RT)-\exp(-\alpha F\eta/RT) \quad (10)$$

This is the Butler-Volmer equation. This equation describes how the observed net current varies as a function of overpotential (η) and transfer coefficient (α). As can be seen from this equation, when the overpotential (η) is zero, no current flows. When i_0 is large (as in reversible cases), small overpotentials are needed to drive the reaction and current flows in both anodic and cathodic directions. In cases where the i_0 is small (as in irreversible cases), high overpotentials are needed to induce current flow.

The above discussion considers the rate of electron transfer reactions at the electrode/solution interface (recall Figure 1.2). However, there are other physical processes that may occur that could influence the overall kinetics of any particular reaction (Figure 1.2). One of the most important of these processes is the mass transfer of the reactant molecule from bulk solution to the electrode surface and the diffusion of products away from the electrode surface. However, for the purposes of this chapter, we refer the reader to more in depth discussion of mass transport [12] and will assume that mass transfer limitations are minimal, which can be achieved by using hydrodynamic working electrodes (electrodes that are rotated).

1.2.1. Electrochemical Techniques

The majority of electrochemical techniques used in the study of environmental systems fall into three categories::

- Potentiometry: equilibrium electrochemistry; potential differences are measured between two electrodes;
- Amperometry: dynamic electrochemistry; a constant potential is applied and the current response is measured;

- Voltammetry: dynamic electrochemistry; a potential is applied in various waveforms and the current response is measured.

As was discussed above, many studies have used potentiometry to measure Eh/pE's of various environmental systems, but because of the complexity of these systems, the results can be difficult to interpret. Amperometry is mostly used for electrolysis or for specific sensors designed to measure certain species in solution. Voltammetry allows for the study of any redox labile species in solution as long as the background current and individual current responses can be separated. In this chapter, we are concerned with probing the physical chemical properties of environmental systems and will therefore focus on voltammetry.

1.2.1.1. Voltammetry

In a typical voltammetry experiment, three electrodes are used. The potential is ramped between a working electrode and a reference electrode. When the potential is strong enough to either oxidize or reduce a substance in solution, the current flows and is measured between the working electrode and a counter electrode.

Working electrodes often are made of noble metals, such as platinum or gold. Other materials have been used in environmental systems, such as the hanging drop mercury electrode and glassy carbon electrodes. Different electrode materials offer varying "windows" in which you can analyze a sample before reducing or oxidizing the solvent. By varying the solvent, the "window" can also be adjusted. For instance, when using a Pt electrode in water, the window ranges from approximately -1.0 V vs. Ag/AgCl to +1.0 V vs. Ag/AgCl. While in DMSO, the window ranges from -1.5 V vs. Ag/Ag^{+} to +0.8 V vs. Ag/Ag^{+}.

Another important variable in voltammetry is the shape and current sampling of the applied potential. The simplest case is called linear sweep voltammetry (LSV) or cyclic voltammetry (CV). In LSV, the potential is ramped linearly in one direction while sampling the current response at each linear step in potential. CV works the same way,

only the potential is ramped back to the beginning after getting to some end point (switching potential).

In differential pulse voltammetry (DPV), the potential is ramped by using pulses and the current is measured at the end of each pulse. A similar technique called square wave voltammetry (SWV) offers even more sensitivity. In SWV, the potential is ramped using square waves in which the potential pulse is applied in both the positive (anodic) and negative (cathodic) direction and the current is sampled at the end of each pulse. The net current is the total current response for both anodic and cathodic currents and is thus amplified. The SWV technique offers the most sensitivity and is also much faster to run than the above techniques.

Other types of studies combine the use of amperometry and voltammetry together, such as in the use of mercury covered gold electrodes for the quantification of trace metals. In this case, a constant potential is applied to the electrode (amperometry) in order to pre-concentrate trace metals onto the mercury, then a DPV or SWV is used to determine the concentration of the trace metals.

1.2.1.2. Qualitative Voltammetry

In order to demonstrate how voltammograms are interpreted, consider a system that consists of a reversible redox couple A/B. The qualitative interpretation of voltammograms is often based on their shapes. In this system, a LSV will give a single peak, either an anodic or cathodic peak depending on which direction the scan was ramped, and a CV will give both an anodic and cathodic peak representing the one electron oxidation and reduction of A and B.

From the Butler-Volmer equation, one would expect the current to increase exponentially with increasing over-potential, yet what is observed are peaks. This is because the increase in net current is not only due to reaction rate (k) but also to the concentration of the redox labile species at the electrode surface. As the potential becomes larger, k increases but at the same time, electrolysis consumes A or B and the

concentration of A or B decreases at the surface, which is only partially replenished by diffusion from bulk solution. This is what causes the peak.

If an unknown system is studied using voltammetry and multiple peaks are obtained, this indicates that there are multiple redox labile species in solution. For instance, it is quite easy to compare a voltammogram of unknown samples (such as natural organic matter) to a standard quinone mixture (see example below). One must be careful, however, not to over interpret such data because multiple redox labile species may give similarly shaped voltammograms. Usually, LSV and CV are good initial tests to determine whether there is any redox activity in the sample.

1.2.1.3. Quantitative Voltammetry

There are several quantitative variables that can be determined from a voltammogram. The potential and current at which the peak occurs are the peak potential (E_p) and the peak current (i_p), respectively. The potential at half the peak height is called the half-peak potential ($E_{p/2}$) and is often considered to be approximately equal to the formal redox potential of the species being studied as long as it is reversible. As in the case above, where we described the qualitative interpretation of voltammograms based on their shapes, quantitative data can also be tabulated and compared. For example, E_p's and i_p's can be used in order to try to elucidate what compounds are giving the redox characteristics in the unknown sample. An irreversible compound will give half-peak potentials that over estimate the true redox potential.

Voltammetry can also be used to determine whether a compound is reversible or irreversible. In the reversible case, the peak potential (E_p) is constant and independent of scan rate. For irreversible compounds, E_p shifts cathodically for reduction reactions and anodically for oxidation reactions.

Quantitatively, for a reversible process:

$$|E_p - E_{p/2}| = 2.20(RT/F) \qquad (11)$$

whereas for the irreversible electron transfer:

$$|E_p - E_{p/2}| = 1.86(RT/\alpha F) \quad (12)$$

The peak current is also larger for reversible couples than for irreversible couples at the same scan rate and for the same concentration. In CV, the difference between E_p^{ox} and E_p^{red} can also give clues as to whether a compound is reversible or irreversible. In the case of a reversible species, the peak potentials are separated by approximately 59 mV and are independent of the scan rate. If n electrons are transferred in a reversible electrode process, the separation becomes:

$$|E_p^{ox} - E_p^{red}| = 2.218(RT/nF) \quad (13)$$

Note that the terms reversible and irreversible refer to limiting cases depending on whether the electrode kinetics are fast or slow relative to the mass transport conditions. Intermediate cases do occur, and are called quasi-reversible, and exhibit properties in-between reversible and irreversible cases.

As with LSV, quantitative data can be obtained with DPV and SWV, but one major difference arises. Due to the way the current is sampled in SWV, the peak potential for reversible systems is used as an estimation of the formal redox potential while $E_{p/2}$ is used for CV.

The brief discussion of the qualitative and quantitative aspects of voltammetry above should give the reader a starting point for understanding how to interpret and use voltammetric techniques. It is beyond the scope of this chapter to deal with the more sophisticated analysis and techniques that have been developed over the last several years. Instead, we will now consider some applications of electrochemistry to the field of environmental chemistry.

1.3. Applications of Physical Environmental Electrochemistry

As was discussed in the introduction, the majority of environmental electrochemical studies fall under the purview of analytical chemistry in which electrochemical techniques are used to determine concentrations of trace metals, etc. Few studies have used electrochemistry in order to probe the physical chemical properties of natural systems. One area of environmental interest where electrochemistry has been used to probe the physical properties is in the study of natural organic matter. Another, more recent area of interest is in the properties of metallic iron. The following sections will review the current understanding of these two systems and demonstrate how electrochemistry can be used to study the physical properties of complex environmental systems.

1.3.1. Electrochemical Properties of NOM and Fractions of NOM

It is well known that NOM can act as a reducing agent (reductant), and that this is central to the role that NOM plays in the biogeochemical cycling of carbon. More recently, it has been reported that NOM plays a role as an electron shuttle in biogeochemical cycles (Figure 1.1). For example, several studies have shown that the addition of NOM to cultures of iron-reducing bacteria can increase the rate of dissimilatory iron reduction [14]. These effects have been attributed to polyphenolic (especially hydroquinonoid) moieties that comprise a portion of NOM [15]. There are, however, other moieties that may contribute to the overall redox activity of NOM (e.g., complexed metals [16]), and this complexity has been one of the main impediments to the development of chemically exact descriptions of redox processes involving NOM.

Early studies on the redox properties of NOM and fractions of NOM most often used voltammetric techniques in which a hanging mercury drop was used as the working electrode. It appears that there was consensus at the time that the humic fraction was not electro-reducible on the mercury drop electrode [17] even though humic-like oxidation products from bituminous coal are electro-reducible, apparently because the humic

fraction contains nitro groups [18]. It turns out that NOM and NOM fractions act mainly as surface active substances and suppress voltammetric responses [19]. Few details of these efforts have been reported because the results suggest only adsorption and not characteristic redox reactions e.g., [19, 20].

More recently, there have been attempts to obtain redox properties of NOM and NOM fractions using solid-state working electrodes in conjunction with various potential wave forms, such as linear sweep voltammetry (LSV), cyclic voltammetry (CV), differential pulse voltammetry (DPV), and square wave voltammetry (SWV). Table 1.1 summarizes the materials and conditions used in several published attempts to use voltammetric methods to characterize the redox properties of NOM.

Many studies have focused on the redox properties of the decomposition products of rice straw, manure, and rice paddy NOM [21, 22]. In general, these electrochemical studies produce voltammograms with relatively good peak definition but do not attempt to determine redox potentials or what substances are producing the peaks in the voltammograms. Yu et al. [23-25] used LSV to study the anaerobic decomposition products of rice straw and vetch. The voltammogram for the vetch sample gave higher net currents and several ill-defined peaks compared to the voltammogram of the rice straw decomposition products. The lack of definition in the peak shapes did not allow for a determination of half-wave potentials but did show that the concentration of reducing substances was the highest at the stage of most vigorous decomposition. Similarly, Ding ([21, 22] and references cited therein) used DPS to study the decomposition products of tree leaves. By using DPS, voltammograms were produced that had better defined peaks. The change in peak height was observed as various treatments were done on the tree leaf solution. They found that an oxidation peak at around 0.5 V vs. SCE did not change after passing the solution through a cation-exchange column. When the solution was passed through an anion-exchange column, the oxidation peak disappeared. They concluded that whatever the reducing substances were, they must be negatively charged and could be adsorbed by soils and iron oxides. Under similar conditions, Ding et al. [26] also showed

that the adsorption of these reducing substances to goethite, Rhodic Ferralsol, Ali-Haplic Acrisol, and Cambisol were 8.15, 4.08, 2.26, and 1.86 cmol kg^{-1}, respectively. This could indicate that the first step in the interaction between NOM and iron/iron oxides is an adsorption step followed by an electron transfer.

This was demonstrated by obtaining a DPS voltammogram of a solution of pine needle decomposition products which gave several moderately defined peaks ranging from –0.05 to +0.69 mV vs. Ag/AgCl. After this solution was reacted with various soils, the lowest (more reduced) peaks disappeared and a large anodic peak appeared which turned out to be Mn^{2+}. They also demonstrated that the manganese oxides were reduced much faster by these reducing substances than the iron oxides. In another paper by Ding in 1991 [21], they found that the use of a glassy carbon working electrode in conjunction with DPS gave relatively well defined peaks for solutions of pine needle and bamboo decomposition products. They were unable to correlate any redox potentials to any specific compound.

Another example of a study that employs electrochemical methods to determine properties and mechanisms of complex systems is a recent report by Liu et al. [27]. They used cyclic voltammetry to determine the reaction mechanism involved in wood decay. They showed that there is a redox cycle involving Cu^{2+}, a quinone, and excess H_2O_2 which leads to a continuous regeneration of Cu^{2+} and production of OH radicals. They show evidence indicating that a chelator-mediated Fenton reaction is favored inside the wood cell wall.

Helburn and McCarthy [28] reported CVs of a humic acid (HA) fraction from peat using conditions that are summarized in Table 1.1. CVs that are representative of their results are reproduced in Fig. 1.3A. At the switching potentials (where the sweep is reversed), the presence of HA resulted in more current, which Helburn and McCarthy ascribed to NOM-catalyzed oxidation and reduction of the solvent (in this case water). Beyond this, their CVs are essentially featureless, so they provide no evidence for a redox reaction at the electrode involving the HA.

Motheo and Pinhedo [29] recently reported a study of HA oxidation using dimensionally stable anodes consisting of mixtures of Ru, Ir, and Ti oxides deposited on a Ti substrate. Under the conditions of their study (Table 1.1), CVs of a peat HA were essentially featureless for a range of electrode compositions (Fig. 1.3B). The results do show, however, significantly greater current with electrodes containing iridium, but this electrode apparently did not produce the greatest oxidation of the HA after extended electrolysis.

In Nurmi et al. [30] cyclic voltammetry was successfully used to obtain some redox properties of natural organic matter (NOM). Using a stationary platinum working electrode, minimal concentrations of electrolyte, and dimethyl sulfoxide (DMSO) as the solvent, Figure 1.3C shows two pairs of oxidation and reduction peaks for a fraction of Georgetown NOM that is enriched in polyphenolic moieties (NOM-PP). Applying this method to other fractions of Georgetown NOM, and to samples of NOM from a wide range of other sources, gave cyclic voltammograms (CVs) that generally contained fewer distinguishing features than those obtained with NOM-PP. For comparison, CVs were also obtained using our method on six quinone model compounds: anthraquinone-2,6-disulfonate (AQDS), lawsone, juglone, menadione, menaquinone-4, and ubiquinone-5. It was shown that the CVs of these model quinones were similar in shape to the CV of NOM-PP, consistent with the notion that quinones are the dominant redox-active moieties associated with NOM-PP. Quantitative analysis of the peaks in these CVs showed that the peak potentials (E_p) were separated by more than 0.059 V and that the peak currents (i_p) were linearly related to the square root of the scan rate ($\nu^{0.5}$) and concentration (C) for both NOM-PP and the model quinones. Equivalent results were obtained with a rotating Pt disk electrode. This seems to indicate that NOM-PP and the model quinones undergo similar sequences of two one-electron, quasi-reversible, diffusion controlled, electron transfers at the Pt electrode surface in DMSO.

More recently, we have obtained more data using the experimental protocol listed in the last column of Table 1.1 [31]. Figure 1.4 shows the type of data obtained using

several electrochemical techniques. The columns in Figure 1.4 are representative of the classification system used in Nurmi (2002) which was based on the shape of the CVs. Each row shows the data obtained using different techniques. The top row shows data obtained for various NOM's with the techniques developed in Nurmi, 2002. The second row is data obtained using a micro-electrode with a linear potential waveform. The third row gives data obtained using a micro-electrode and a square wave potential waveform. From top to bottom the number of peaks that can be identified increases. Recall that peaks are indicative of redox active compounds or moieties. The potential at which the peak occurs can be related to the redox potential for that compound or moiety. The peak potential (E_p) when using SWV is indicative of the formal redox potential of whatever moiety or compound is giving the current response. Note that in Figure 1.4, the NOM-GT sample gave the most peaks. This is probably due to the fact that NOM-GT is a raw NOM sample that has undergone minimal treatments and thus may contain the most redox active moieties or compounds. It appears that NOM contains more than a single redox labile moiety/compound and thus attributing a single redox potential is misleading. This will be further discussed below.

Also note that the NOM-PP fraction gave the best defined set of peaks and is most similar to the quinone model compounds. Since the procedure for obtaining NOM-PP is meant to concentrate the polyphenolic fractions of NOM, and that quinone moieties are polyphenols, the electrochemical response obtained from NOM-PP is most probably due to quininoid moieties.

Although it is difficult to relate these results to Nernstian standard potentials vs. the standard hydrogen electrode (SHE) under aqueous conditions, it is clear that the apparent formal potential for NOM-PP lies between the corresponding potentials for menadione and juglone and well above that of AQDS.

It appears, from the studies of Yu et al. [8], Ding et al. [21, 22], and Nurmi et al. ([31] and unpublished data), that raw NOM gives multiple peaks indicative of multiple redox active compounds or moieties. Although we have shown that the NOM-PP fraction

of NOM-GT qualitatively and quantitatively resembles quinonoid species, it is clear that this is not the only redox labile species in NOM. In the past, many studies have attributed a single redox potential to NOM, either assuming it is a quinone or by measuring it using Eh or voltammetry. We propose that instead of attributing a single redox potential to NOM, a redox continuum exists in natural systems. Figure 1.5 demonstrates how the various peak potentials (formal redox potentials) relate to known and measured redox potentials for various NOM fractions and environmentally relevant contaminants. A redox continuum would allow for multiple compounds to exist and be redox active depending on the system.

In many ways, a redox continuum that exists in environmental systems may act similarly to electron transport systems (ETS) found in all living things. One of the main differences would be the level of organization of the various electron transfer shuttles. In living things, the electron shuttles are organized in ways that maximize efficiency of electron transfer [32]. In environmental systems that contain various electron transfer shuttles, they are likely to be more diffuse and unstructured. However, there exists the possibility that several electron transfer shuttles could exist within the structure of a humic molecule which could imply some level of organization.

1.3.2. Iron—H_2O—Contaminant Electrochemistry

The literature that accompanies the field of iron electrochemistry, especially with respect to corrosion, is massive and beyond the scope of this paper. For purposes of this dissertation, only studies that involve iron coupled to the degradation of an environmentally relevant contaminant will be discussed. Table 1.2 gives the experimental parameters of several studies using electrochemical techniques to probe iron mediated reduction of various contaminants.

One of the founders of electrochemistry worked on problems that now play a prominent role in physical environmental electrochemistry. Fritz Haber (1868-1934) introduced controlled potential electrolysis and elucidated the mechanism of nitrobenzene

reduction at the surface of an iron electrode. At the time, nitrobenzene reduction was of interest because of the need for dyestuff precursors. Today, we use this same system to degrade nitrobenzene and many other environmental groundwater contaminants with iron metal [33].

Electrochemical model systems allow direct monitoring and control of redox reactions at the iron-solution interface, and a number of studies have taken this approach to study contaminant reduction by iron metal. In experiments similar to Haber's, others have studied the electrochemistry of iron reactions with various contaminants. Scherer et al. developed an alternative method to study the kinetics of contaminant reduction by iron metal. Scherer et al. [34-36] used a polished, high purity, iron rotating disk electrode to determine the contribution of mass transfer to contaminant reduction kinetics and derived mixed-potential diagrams for the interfacial electron transfer resulting from simultaneous aqueous corrosion of iron and reduction of contaminants. The electrochemical design included using a Fe^0 rotating disk electrode ($RD_{Fe}E$). By controlling the rotation of the electrode, the mass-transport of oxidant to the electrode surface could be controlled. Fitting the Butler-Volmer equations for the three reactions involved in this system,

$$Fe^0 \rightarrow Fe^{2+} + 2e^- \quad (14)$$

$$2H_2O + 2e^- \rightarrow H_2(g) + 2OH^- \quad (15)$$

$$RCl + H^+ + 2e^- \rightarrow RH + Cl^- \quad (16)$$

they determined rate constants for each of the half reactions above and were able to demonstrate that the kinetics of carbon tetrachloride reduction at an oxide-free iron electrode was limited by reaction kinetics vs. mass-transport. In a subsequent study, Scherer et al. [35] demonstrated that the kinetics of nitrobenzene reduction were dependant on rotation rate indicating that mass transport processes were important to consider when designing a permeable reactive barrier filled with Fe^0.

The mechanisms of Fe^0 mediated reduction of contaminants have also been investigated. It has been well documented that Fe^0 acts as a reductant, donating electrons

to oxidants such as CCl_4, TCE etc., but it has also been hypothesized that hydrogen atoms formed at the Fe^0 surface may be involved in reactions with contaminants in solution. Farrell et al. [37-39] used iron disk and wire electrodes to show that PCE is reduced mainly by electron transfer at low and neutral pH. In contrast, TCE is reduced via hydrogen atoms at low pH and both electron transfer and hydrogen atoms at neutral pH's. Farrell hypothesized that the differences observed in reaction rates between PCE and TCE may be due to the differences in reduction pathways. Contaminant reduction by iron may be due to hydrogen atom transfer as well as electron transfer, and the relative importance of these reactions varies with contaminant structure.

Other studies have combined electrochemical techniques with spectroscopy in order to study the surface evolution of Fe in solutions of contaminants. Odziemkowski et al. [40-43] applied Raman spectroscopy to characterize the films that form on iron electrodes; demonstrating, among other things, that auto-reduction of the air-formed passive film on iron contributes to the rapid reduction kinetics that are observed for many dissolved contaminants. Others have used electrochemical methods to investigate effects of buffers [44], mass transport [45], and reactive metals or metal oxides other than iron [46-49].

Since iron particles used in PRBs are considered to be covered in iron oxides, Logue et al. [49] measured the rates of CCl_4 and nitrobenzene reduction at iron oxide coated gold electrodes. By varying the amount of Fe^{2+} in the oxide, it was shown that the rates of CT and NB reduction were independent of Fe^{2+} concentration but directly related to the oxide thickness suggesting that reaction occurred at the oxide/electrode interface, not the solution/oxide interface.

The examples given above on the electrochemical aspects of the corrosion of iron metal have been studied using polished disks, wires, Fe^{3+} oxide coated Au and iron coupon electrodes, but these model systems do not represent many characteristics of the granular iron used in environmental remediation applications. To address this issue, Nurmi et al. [50] modified a rotating disk electrode with a cavity that accommodates a

wide range of iron powders. By comparison with conventional Fe^0 and Pt^0 disk electrodes, we found that the powder disk electrodes (PDEs) packed with un-pretreated, < 147 μm granular iron give anodic polarization curves that are unaffected by the underlying disk material and are consistent with a large electro-active surface area of iron that is initially coated with an air-formed passive film. This design will ultimately allow for the electrochemical study of the reduction of aqueous environmental contaminants by relevant iron powders. It turns out that cavity size and rotation rate have synergistic effects that suggest that most of the iron powder is electro-active, hydrogen evolution in the active region is kinetically limited, and iron dissolution in the active region is affected by mass transport of solutes in the cavity pore space and the formation of a passivating film.

Recently, the PDE developed in the above study was used to obtain anodic polarization curves for various nano-iron preparations [51]. By comparing various types of iron powders ranging in oxide composition and size, it was shown that the E_{corr} as determined from a LSV was dependant on the valence state of the iron oxide powder packed into the PDE. Not surprisingly, maghemite nano-powder gave the most positive E_{corr} with magnetite next, and then the Fe^0 nano-powder with the most negative E_{corr}'s. Interestingly, the nano-Fe^0 powders gave more negative E_{corr}'s than either the polished Fe^0 disk or PDE packed with the Fischer electrolytic Fe. This cathodic shift in E_{corr} may be the result of either thermodynamic or kinetic processes of the nano iron. E_{corr}'s are dependant on both the intrinsic redox potential of the material as well as the rate of anodic and cathodic reactions at the iron surface [52]. Whether this shift in E_{corr} is due to the reduced dimensionality of the nano Fe^0 or to some other characteristic of these materials is still unclear and under further investigation.

1.4. References

[1] Rodgers, J. D.; Bunce, N. J. Electrochemical treatment of 2,4,6-Trinitrotoluene and related compounds *Environ Sci Technol* **2001**, *35*, 406-410.

[2] Acar, Y. B.; Alshawabkeh, A. N. Principles of electrokinetic remediation *Environ. Sci. Technol.* **1993**, *27*, 2638-2647.

[3] Wick, L. Y.; Mattle, P. A.; Wattiau, P.; Harms, H. Electrokinetic transport of PAH-degrading bacteria in model aquifers and soil *Environ Sci Technol* **2004**, *38*, 4596-4602.

[4] Lesage, S.; Brown, S.; Millar, K. Vitamin B12-catalyzed dechlorination of perchloroethylene present as residual DNAPL *Ground Water Monit. Rem.* **1996**, 76-85.

[5] Rajeshwar, K.; Ibanez, J. G. *Environmental Electrochemistry*; Academic Press: San Diego, 1997.

[6] Sequeira, C. A. C., Ed. *Environmental Oriented Electrochemistry*; Elsevier Publishing Company, 1994.

[7] Taillefert, M.; Rozan, T. F., Eds. *Environmental Electrochemistry: Analyses of Trace Element Bigeochemistry (Acs Symposium Series)*; American Chemical Society, 2002.

[8] Yu, T. R.; Ji, G. L. *Electrochemical Methods in Soil and Water Research*; Pergamon Press: New York, 1993.

[9] Mackay, D.; Boethling, R. S. *Handbook of Property Estimation Methods for Chemicals: Environmental and Health Sciences*; Lewis: Boca Raton, FL, 2000.

[10] Lovley, D. R.; Phillips, E. J. P. Reduction of uranium by *Desulfovibrio desulfuricans* *App. Environ. Microbiol.* **1992**, *58*, 850-856.

[11] Vetter, K. J. General Kinetics of Passive Layers on Metals *Electrochimica Acta* **1971**, *16*, 1923-1937.

[12] Bard, A. J.; Faulkner, L. R. *Electrochemical Methods. Fundamentals and Applications*; 2nd ed.; Wiley: New York, 2001.

[13] Grundl, T. A review of the current understanding of redox capacity in natural, disequilibrium systems *Chemosphere* **1994**, *28*, 613-626.

[14] Lovley, D. R.; Fraga, J. L.; Blunt-Harris, E. L.; Hayes, L. A.; Phillips, E. J. P.; Coates, J. D. Humic substances as a mediator for microbially catalyzed metal reduction *Acta Hydrochim. Hydrobiol.* **1998**, *26*, 152-157.

[15] Scott, D. T.; McKnight, D. M.; Blunt-Harris, E. L.; Kolesar, S. E.; Lovley, D. R. Quinone moieties act as electron acceptors in the reduction of humic substances by humics-reducing microorganisms *Environ. Sci. Technol.* **1998**, *32*, 2984-2989.

[16] Struyk, Z.; Sposito, G. Redox properties of standard humic acids *Geoderma* **2001**, *102*, 329-346.

[17] Kolthoff, I. M.; Lingane, J. J. *Polarography*; 2nd ed.; Wiley: New York, 1952.

[18] Cody, A. F. M., S. R.; Kinney, C. R. Polarograohy of humic acid-like oxidation products of bituminous coal *Analytical Chemistry* **1955**, *27*.

[19] Lucena-Conde, F.; Gonzalez-Crespo, A. In *7th International Congress of Soil Science*: Madison, WI, 1960; pp 59-65.

[20] Lindbeck, M. R. Y., J. L. Polarography and coulometry in dimethylsulfoxide, of nitric acid oxidation products from soul humic acid *Soil Sci.* **1966**, *101*, 366-372.

[21] Ding, C. P. W., J. H. In *Electrochemical Methods in Soil and Water Research*; Yu, T. R. J., G. L., Ed.; Pergammon Press: Oxford, 1993; pp 366-412.

[22] Ding, C. P. L., Z. G.; Yu, T.R. *Soil Sci.* **1982**, *134*, 252-257.

[23] Yu, T.-R. In *Proceedings of Symposium on Paddy Soil*; Insitute of Soil Science, A. S., Ed.; Science Press: Beijing, 1981; pp 95-106.

[24] Yu, T.-R., Ed. *Physical Chemistry of Paddy Soils*; Science Press: Beijing, 1985.

[25] Yu, T. R.; Ji, G. L. *Electrochemical Methods in Soil and Water Research*; Pergamon: Tarrytown, NY, 1993.

[26] Chang-pu, D.; Zhi-guang, L. In *Proceedings of Symposium on Paddy Soil*; Institute of Soil Science, A. S., Ed.; Science Press: Beijing, 1981; pp 251-254.

[27] Liu, R.; Goodell, B.; Jellison, J.; Amirbahman, A. Electrochemical study of 2,3-dihydroxybenzoic acid and its interaction with Cu(II) and H2O2 in aqueous solutions: implications for wood decay *Environ. Sci. Technol.* **2005**, *39*, 175-180.

[28] Helburn, R. S.; MacCarthy, P. Determination of some redox properties of humic acid by alkaline ferricyanide titration *Anal. Chim. Acta* **1994**, *295*, 263-272.

[29] Motheo, A. J.; Pinhedo, L. Electrochemical degradation of humic acid *Sci. Total Environ.* **2000**, *256*, 67-76.

[30] Nurmi, J. T.; Tratnyek, P. G. Electrochemical properties of natural organic matter (NOM), fractions of NOM, and model biogeochemical electron shuttles *Environ. Sci. Technol.* **2002**, *36*, 617-624.

[31] Nurmi, J. T.; Tratnyek, P. G. In *Proceedings of the 20th Anniversary Conference of the International Humic Substances Conference (IHSS), 21-26 July 2002, Northeastern University, Boston, MA*, 2002; pp 58-60.

[32] Brock, T. D.; Madigan, M. T. *Biology of Microorganisms*; 6 ed., 1991.

[33] Tratnyek, P. G.; Scherer, M. M.; Johnson, T. J.; Matheson, L. J. In *Chemical Degradation Methods for Wastes and Pollutants: Environmental and Industrial Applications*; Tarr, M. A., Ed.; Marcel Dekker: New York, 2003; pp 371-421.

[34] Scherer, M. M.; Westall, J. C.; Ziomek-Moroz, M.; Tratnyek, P. G. Kinetics of carbon tetrachloride reduction at an oxide-free iron electrode *Environ. Sci. Technol.* **1997**, *31*, 2385-2391.

[35] Scherer, M. M.; Johnson, K.; Westall, J. C.; Tratnyek, P. G. Mass transport effects on the kinetics of nitrobenzene reduction by iron metal *Environ. Sci. Technol.* **2001**, *35*, 2804-2811.

[36] Scherer, M. M.; Westall, J. C.; Tratnyek, P. G. Discussion on "Electrochemical and Raman spectroscopic studies of the influence of chlorinated solvents on the corrosion behaviour of iron in borate buffer and in simulated groundwater" [*Corrosion Science* 42 (2000) 1921-1939] *Corr. Sci.* **2001**, *44*, 1151-1157.

[37] Farrell, J.; Melitas, N.; Li, T. Electrochemical and column investigation of iron-mediated reductive dechlorination of trichloroethylene and perchloroethylene *Environ. Sci. Technol.* **2000**, *34*, 2549-2556.

[38] Li, T.; Farrell, J. Electrochemical investigation of the rate-limiting mechanisms for trichloroethylene and carbon tetrachloride reduction at iron surfaces *Environ. Sci. Technol.* **2001**, *35*, 3560-3565.

[39] Wang, J.; Farrell, J. Investigating the role of atomic hydrogen on chloroethene reactions with iron using Tafel analysis and electrochemical impedance spectroscopy *Environ. Sci. Technol.* **2003**, *37*, 3891-3896.

[40] Bonin, P. M. L.; Jedral, W.; Odziemkowski, M. S.; Gillham, R. W. Electrochemical and Raman spectroscopic studies of the influence of chlorinated solvents on the corrosion behaviour of iron in borate buffer and in simulated groundwater *Corr. Sci.* **2000**, *42*, 1921-1939.

[41] Bonin, P. M. L.; Odziemkowski, M. S.; Gillham, R. W. Influence of chlorinated solvents on polarization and corrosion behaviour of iron in borate buffer *Corr. Sci.* **1998**, *40*, 1391-1409.

[42] Bonin, P. M. L.; Odziemkowski, M. S.; Reardon, E. J.; Gillham, R. W. In situ identification of carbonate-containing green rust on iron electrodes in solutions simulating groundwater *J. Solut. Chem.* **2000**, *29*, 1061-1074.

[43] Odziemkowski, M. S.; Schuhmacher, T. T.; Gillham, R. W.; Reardon, E. J. Mechanism of oxide film formation on iron in simulating groundwater solutions: Raman spectroscopic studies *Corr. Sci.* **1998**, *40*, 371-389.

[44] Lavine, B. K.; Auslander, G.; Ritter, J. Polarographic studies of zero valent iron as a reductant for remediation of nitroaromatics in the environment *Microchem J.* **2001**, *70*, 69-83.

[45] Bigg, T.; Judd, S. J. Electrochemical monitoring of water remediation by metallic iron *J. Appl. Electrochem.* **2001**, *31*, 1339-1344.

[46] Warren, K. D.; Arnold, R. G.; Bishop, T. L.; Lindholm, L. C.; Betterton, E. A. Kinetics and mechanism of reductive dehalogenation of carbon tetrachloride using zero-valence metals *J. Haz. Mat.* **1995**, *41*, 217-227.

[47] Liu, Z.; Arnold, R. G.; Betterton, E. A.; Festa, K. D. Electrolytic reduction of CCl_4—Effects of cathode material and potential on kinetics, selectivity, and product stoichiometry *Environ. Eng. Sci.* **1999**, *16*, 1-13.

[48] Liu, Z.; Betterton, E. A.; Arnold, R. G. Electrolytic reduction of low molecular weight chlorinated aliphatic compounds: structural and thermodynamic effects on process kinetics *Environ. Sci. Technol.* **2000**, *34*, 804-811.

[49] Logue, B. A.; Westall, J. C. Kinetics of reduction of nitrobenzene and carbon tetrachloride at an iron-oxide coated gold electrode *Environ. Sci. Technol.* **2003**, *37*, 2356-2362.

[50] Nurmi, J. T.; Bandstra, J. Z.; Tratnyek, P. G. Packed powder electrodes for characterizing the reactivity of granular iron in borate solutions *J. Electrochem. Soc.* **2004**, *151*, B347-B353.

[51] Nurmi, J. T.; Tratnyek, P. G.; Sarathy, V.; Baer, D. R.; Amonette, J. E.; Pecher, K.; Wang, C.; Linehan, J. C.; Matson, D. W.; Penn, R. L.; Driessen, M. D. Characterization and properties of metallic iron nanoparticles: spectroscopy, electrochemistry, and kinetics *Environ. Sci. Technol.* **2005**, *39*, 1221-1230.

[52] Bockris, J. O. M.; Khan, S. U. M. *Surface Electrochemistry. A Molecular Level Approach*; Plenum: New York, 1993.

Table 1.1. Electrochemical parameters used in voltammetric studies of NOM and fractions of NOM.

Properties	Yu 1985, [8]	Ding, 1991 [21, 22]	Helburn, 1994 [28]	Motheo, 2000 [29]	Nurmi, IHSS, 2002 [31]	Nurmi, unpublished
Working electrode	GC	GC,CPE, CFbE	Au Wire	$Ti/Ir_nTi_nO_2$	Pt disk	Pt microelectrode
Counter electrode	Pt		Au Wire	Steel	Pt wire	Pt wire
Reference electrode	SCE	Ag/AgCl	SCE	SCE	Ag/Ag^+	Ag/Ag^+
Potential Wave Form	LSV	DPS	LSV	LSV	LSV	LSV and SWV
Scan Rate		2 mV/s	500 mV/s	50 mV/s	10 mV/s	1.0-100 mV/s
Solvent	H_2O	H_2O	H_2O	H_2O	DMSO	DMSO
Electrolyte		NH_4Ac	0.5 M KCl	0.1 M KCl	1.0 mM $NaClO_4$	1.0 mM $NaClO_4$
NOM conc.			3 g/L	30 mg/L	90 mg/L	90 mg/L
NOM type	Rice straw/vetch decomp. products		Glenamoy Ireland HA	Mogi Guacu River peat HA	Various NOM	Various NOM

Table 1.2. Electrochemical parameters used in electrochemical studies of Fe-H_2O-contaminant systems.

Properties	Haber	Gillham	Scherer	Farrel	Ponder	Nurmi
Working electrode	Fe wire	Fe wire	Fe disk	Fe Wire	GC	PDE
Iron Type					Nano Fe	FeIc, Fe^{III}, Fe^{II2}
Counter electrode	Pt	Steel	Pt	Au Wire	Pt disk	Pt disk
Reference electrode	Ag/AgCl	SCE	Ag/AgCl	SCE	Ag/Ag^+	Ag/Ag^+
Potential Wave Form	LSV	LSV	LSV	LSV/EIS	LSV	LSV
Scan Rate		50 mV/s		500 mV/s	10 mV/s	1.0-100 mV/s
Solvent	H_2O	H_2O	H_2O	H_2O	H_2O	H_2O
Electrolyte	Borate	0.1 M KCl	Borate	0.5 M KCl	1.0 mM Borate	1.0 mM Borate

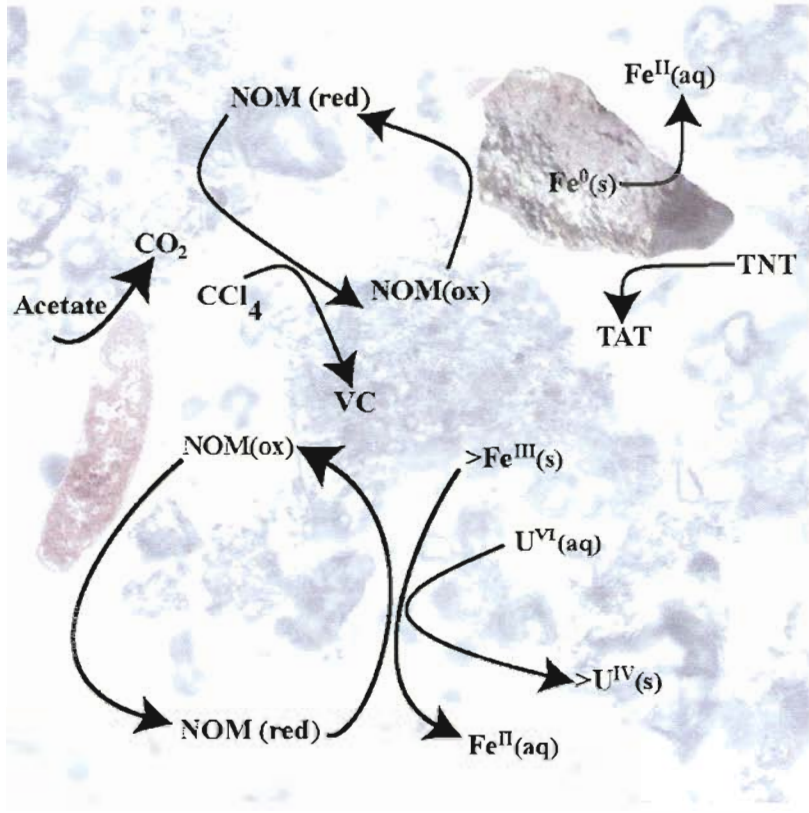

Figure 1.1. Possible biogeochemical electron transfer pathways of NOM. The oblong species on the left represents a bacterium such as *G. metallireducens*. The object in the upper right represents an iron particle.

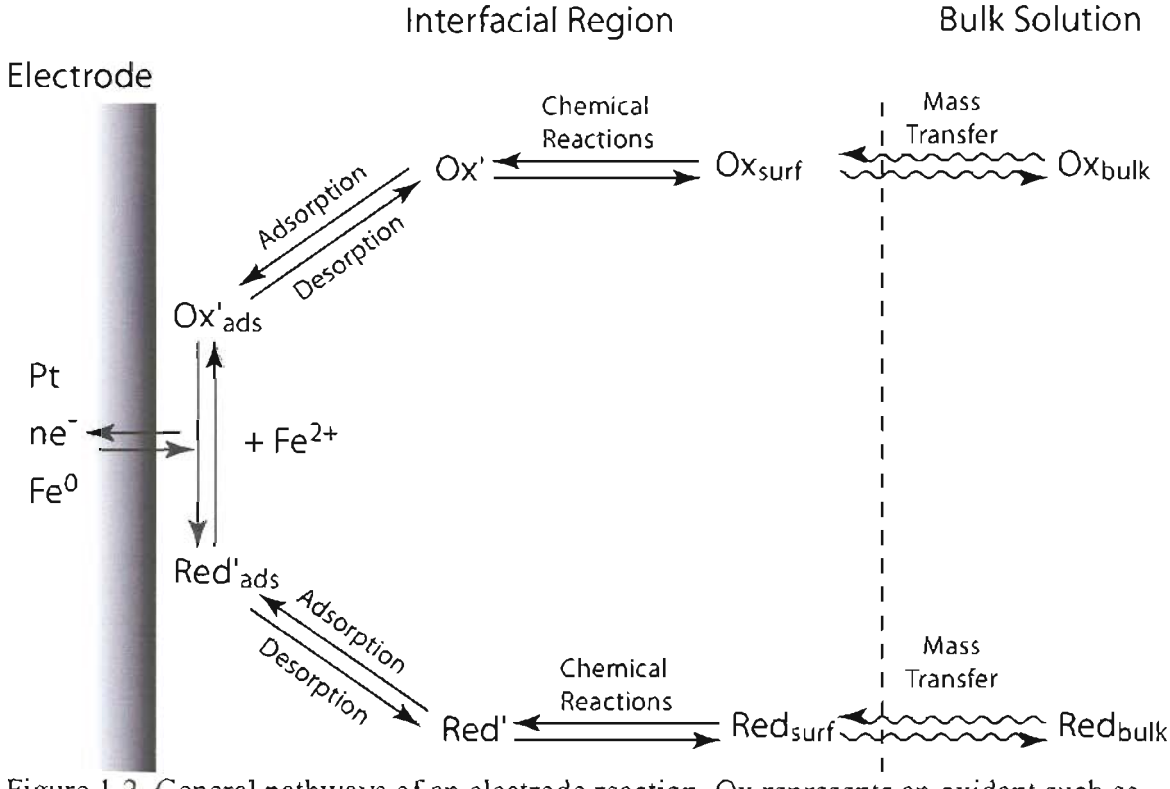

Figure 1.2. General pathways of an electrode reaction. Ox represents an oxidant such as CCl_4 and Red represents a reductant.

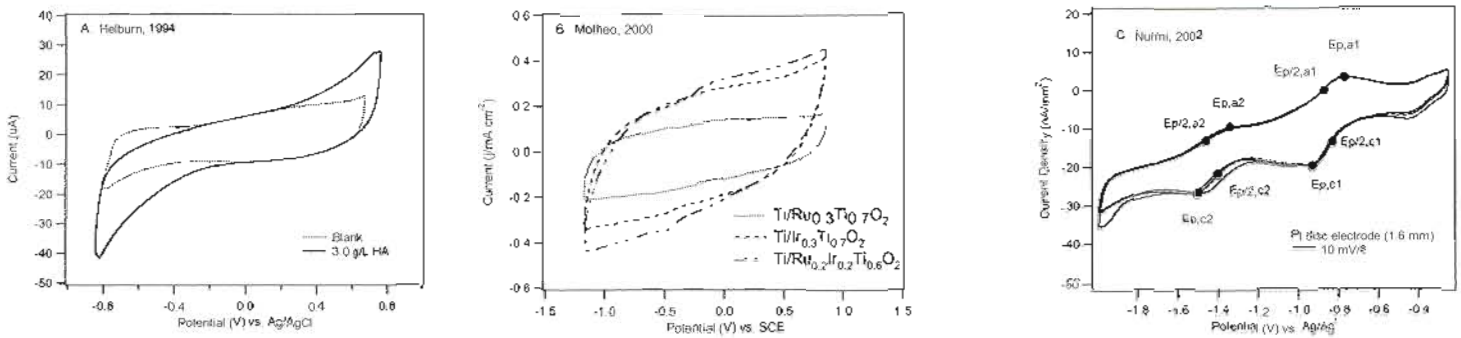

Figure 1.3. Three examples of cyclic voltammograms of NOM under different conditions. In A and B, CVs were obtained under aqueous conditions. In C, the experiment was done in DMSO.

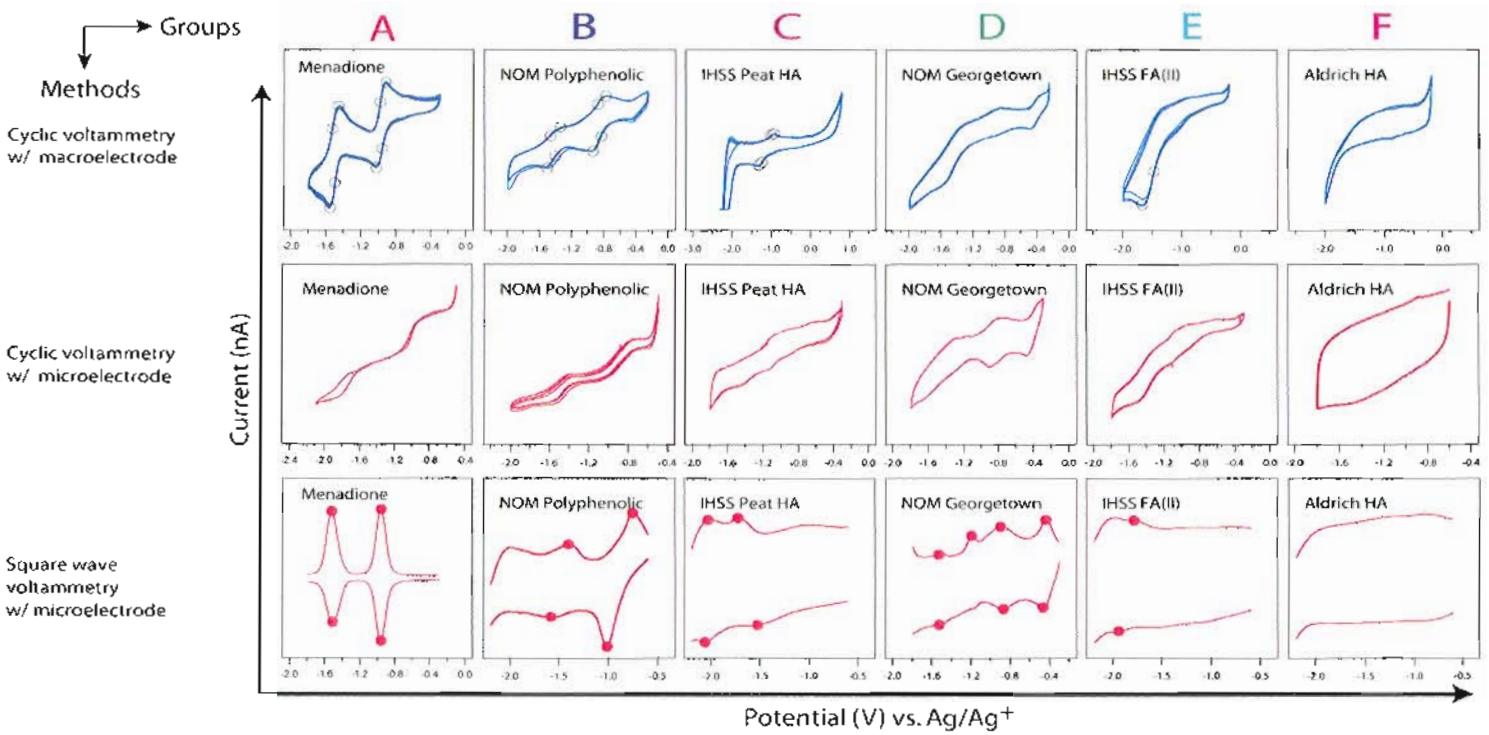

Figure 1.4. The columns represent a division of NOM grouping based on the qualitative shape of the voltammogram [31]. The rows represent increasing complexity of electrochemical technique. Note that more peaks appear in the third row vs. the top two rows.

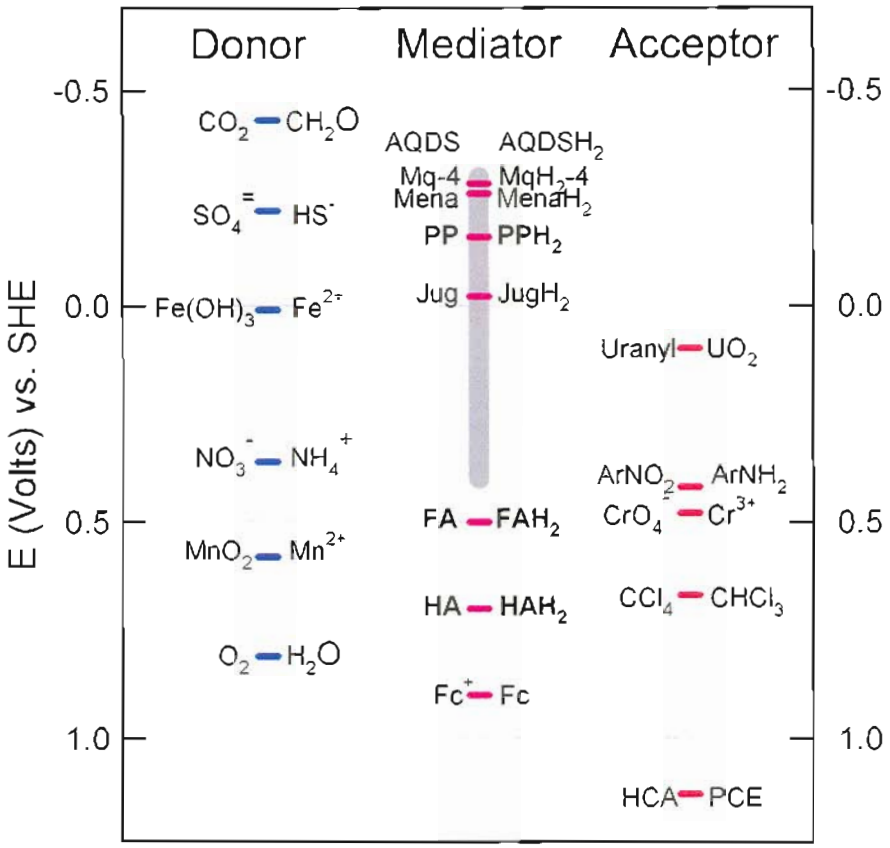

Figure 1.5. Redox ladder showing possible electrons donors, mediators, and acceptors. PP stands for the NOM-PP fraction and the gray bar represents the range of peaks observed for the un-fractionated NOM-GT sample.

Section 2.0. Electrochemical Properties of Natural Organic Matter (NOM), Fractions of NOM, and Model Biogeochemical Electron Shuttles[1]

2.1. Cyclic Voltammetry of NOM with Macroelectrodes

2.1.1. Abstract

In this study, cyclic voltammetry was used to characterize the redox properties of natural organic matter (NOM). Using a stationary platinum working electrode, minimal concentrations of electrolyte, and dimethyl sulfoxide (DMSO) as the solvent, we were able to resolve two pairs of oxidation and reduction peaks for a fraction of Georgetown NOM that is enriched in polyphenolic moieties (NOM-PP). Applying our method to other fractions of Georgetown NOM, and to samples of NOM from a wide range of other sources, gave cyclic voltammograms (CVs) that generally contained fewer distinguishing features than those obtained with NOM-PP. For comparison, CVs were also obtained using our method on six quinone model compounds: anthraquinone-2,6-disulfonate (AQDS), lawsone, juglone, menadione, menaquinone-4, and ubiquinone-5. The CVs of these quinones were similar in shape to the CV of NOM-PP, consistent with the notion that quinones are the dominant redox-active moieties associated with NOM. Quantitative

[1] Reproduced with permission from Nurmi, J. T.; Tratnyek, P. G. Electrochemical properties of natural organic matter (NOM), fractions of NOM, and model biogeochemical electron shuttles *Environ. Sci. Technol.* **2002**, *36*, 617-624. Copyright 2005 American Chemical Society.

analysis of the peaks in these CVs showed that the peak potentials (E_p) were separated by more than 0.059 V, and that the peak currents (i_p) were linearly related to the square root of the scan rate ($\nu^{0.5}$) and concentration (C) for both NOM-PP and the model quinones. Equivalent results were obtained with a rotating Pt disk electrode. From this we conclude that NOM-PP and the model quinones undergo similar sequences of two one-electron, quasi-reversible, diffusion controlled, electron transfers at the Pt electrode surface in DMSO. Although it is difficult to relate these results to Nernstian standard potentials vs. the standard hydrogen electrode (SHE) under aqueous conditions, it is clear that the apparent formal potential for NOM-PP lies between the corresponding potentials for menadione and juglone, and well above that of AQDS. Attempts to derive correlations between E_p and i_p for the NOMs with quantifiable electrode response and other measurable properties of NOM (including trace metal content and UV-Vis absorbance) did not yield any strong relationships.

2.1.2. Introduction

Numerous studies have suggested that natural organic matter (NOM) contributes to biogeochemical redox processes by shuttling electrons from donors to acceptors. In most cases, the mediation of electron transfer in environmental systems has been attributed to redox-active groups that are associated with NOM (quinonoid moieties (e.g., [1] and complexed metals (e.g., [2]), but a variety of relatively simple biogenic solutes could also be involved (e.g., extracellular cytochromes [3], porphyrins [4, 5], and quinones [6]). The relative significance of all these putative electron shuttles in natural systems is still unclear.

Over the last 10 years, considerable evidence has accumulated that the quinone moieties in NOM can contribute to the reduction of organic contaminants such as alkyl halides and nitro aromatics (e.g., [7-9]). More recently, the role of quinones in the redox activity of NOM has been the subject of increased interest because of indications that they can stimulate the reduction of ferric oxides by iron reducing bacteria. It has even

been proposed that the "quinone shuttle" effect can be manipulated to reduce contaminants that are sequestered in small pores where bacteria cells are excluded [10].

To obtain a more detailed understanding of the role that NOM plays in biogeochemical redox process, it would be desirable to know more about the identity and properties of the specific functional groups that determine the redox activity of NOM. Most recent progress in this area has come from spectroscopic analyses of NOM (e.g., with electron paramagnetic resonance spectroscopy [11] and kinetic studies using NOM model compounds such as anthraquinone-2,6-disulfonate (AQDS), lawsone, and juglone [11-16]. However, these approaches provide only indirect information on the redox properties of NOM.

The direct approach for characterizing the redox properties of NOM is to apply electrochemical techniques, but previous efforts in this area have met with limited success. For example, Helburn et al. reported mostly featureless cyclic voltammograms (CVs) of NOM and NOM fractions in water using a gold working electrode [17]. Perhaps the most successful studies that are relevant to the electrochemical properties of NOM have described the effects of NOM on polarography of dissolved metals in natural waters [18, 19]. These studies generally find that NOM (and its fractions) adsorb at the mercury drop but do not produce a direct electrode response [18, 20-22]. This lack of electrode-activity that is attributable to NOM alone facilitates electrochemical studies of metal complexation with NOM, but makes it difficult to investigate the electrochemical properties of NOM directly.

We recently described preliminary results using an electrochemical method that gives characteristic CVs for many samples of NOM, NOM fractions, and model quinones [23]. In this report, we present the details of our method and its validation, the results obtained with an expanded range of NOM samples and model compounds, and an analysis of what these results reveal about the redox activity of NOM. The CVs we have obtained range from featureless (esp. with Aldrich humic acid) to having two rather well-defined pairs of peaks (esp. with a fraction of Georgetown NOM that has been enriched in polyphenolic moieties). The latter are qualitatively very similar to the CVs obtained

with a wide range of model ortho-quinones (Fig. 2.1). Many of the CVs were sufficiently well-defined to extract quantitative characteristics such as the peak potentials (E_p), half-peak potentials ($E_{p/2}$), and peak currents (i_p). Further analysis with these parameters—or derivatives of these parameters such as peak separations (ΔE_p) and peak current ratios (i_p^{red}/ i_p^{ox})—allowed us to determine electrode kinetics, relative potentials, and other electrochemical characteristics for NOM from a wide variety of sources and preparations. Finally, the qualitative and quantitative characteristics of the CVs of NOM are compared to more commonly determined properties such as specific UV absorbance (SUVA) and metals content.

2.1.3. Experimental Section

Reagents. The NOM and fractions of NOM used in this study were primarily samples obtained from Baohua Gu (Oak Ridge National Laboratory). He obtained the raw material (NOM-GT) by reverse osmosis of brown water from a wetland pond in Georgetown, SC, and isolated the humic and fulvic fractions by solubility in acid and base [24]. The resulting fulvic acid was further separated on a column of cross-linked polyvinyl pyrrolidone polymer [25] into two fractions: the retentate (NOM-PP), which should be enriched in polyphenolic material, and the eluate (NOM-CH), which should consist of carbohydrates, proteins, amino acids, and other soluble salts. A detailed characterization of these materials has recently been reported, based on UV/Vis, FTIR, NMR, fluorescence, and EPR spectroscopies [26, 27].

Other NOM fractions were obtained from the International Humic Substance Society (IHSS), including fulvic acid standard II (FA(II)), soil humic acid (S-HA), peat humic acid (P-HA) and peat fulvic acid (P-FA). George Aiken (US Geological Survey, Boulder, CO) provided the Suwannee River fulvic acid (SR-FA) and Lake Fryxell fulvic acid (LF-FA). Y. Chin (Ohio State University) provided the Pine Barrens NOM (PB-NOM), D. Macalady (Colorado School of Mines) provided the Manuka NOM (MN-NOM), and J. Coates (Southern Illinois University) provided the San Diego Harbor humic acid (SD-HA). Aldrich humic acid (AL-HA) was obtained from Aldrich and used

as received. Various characterizations of these NOMs have been reported previously (e.g., [28-33]).

The model compounds anthraquinone-2,6-disulfonic acid (AQDS), 5-hydroxy-1,4-naphthoquinone (juglone), 2-hydroxy-1,4-naphthoquinone (lawsone), 2-methyl-3-(3,7,11,15-tetramethyl-2,6,10,14-hexadecatetraenyl)-1,4-naphthoquinone (menaquinone-4), 2,3-dimethoxy-5-methyl-6-[3-methyl-2-butenyl]-1,4-benzoquinone (ubiquinone-5), 2-methyl-1,4-naphthoquinone (menadione), and dicyclopentadienyliron (ferrocene) were obtained from Sigma or Aldrich and were used as received. The structures of the quinone model compounds are given in Fig. 2.1.

All stock solutions of NOM were prepared by dissolving the freeze-dried material directly into organic or aqueous solvents. The organic solvents, dimethyl sulfoxide (DMSO) and dimethyl formamide (DMF), were purchased from Sigma (ACS Reagent grade, <0.1% and <0.15% H_2O respectively). For electrolytes KCl (ACS Reagent), NaClO4 (ACS Reagent grade 99% purity), and $AgNO_3$ were obtained from Aldrich, Sigma, and Bioanalytical Systems Inc., respectively.

Voltammetry. Cyclic voltammograms (CVs) were obtained with a potentiostat (Pine Model AFCBP1) and a three-electrode cell (BAS). After considerable experimentation in aqueous solution (1.0 mM KCl electrolyte, 1.6-mm dia. Pt disc working electrode or 3.0-mm dia. glassy carbon working electrode, Pt wire counter electrode, Ag/AgCl reference electrode) and preliminary testing in DMF (conditions same as for DMSO, see below), it was determined that the best results were obtained using DMSO. The preferred conditions were: 1.0 mM $NaClO_4$ electrolyte, 1.6-mm dia. Pt disc working electrode, Pt wire counter electrode, and Ag/Ag^+ reference electrode. All electrode potentials are reported vs. the Ag/Ag^+ reference electrode, unless noted otherwise, and currents are reported in accord with IUPAC convention (anodic current is positive and cathodic current is negative).

Between each set of scans, the working electrode was polished (1.0 μ and 0.25 μ diamond polishing paste), washed and sonicated with water and methanol, and allowed to dry. To remove oxygen, test solutions were purged in the cell with high purity Ar for 15

minutes before each set of scans. CVs were usually initiated by scanning cathodically starting at -0.25 V. Hydrodynamic rotating disk electrode (RDE) experiments were performed with the same conditions but with a 3.0 mm dia. Pt disc rotating electrode (Pine). Background scans were performed prior to every experimental treatment, and proper performance of the overall system was periodically verified by reproducing CVs for ferrocene/ferricenium ion.

Spectroscopy. UV/Vis spectra were recorded on a Perkin Elmer Lambda 20 spectrometer. A 1-cm quartz cuvette was used and the samples were scanned from 190 nm to 800 nm. For this, the NOM fractions were prepared to be 10 mg C L^{-1} with deionized water and then adjusted to pH = 7.0 with a weak solution of sodium hydroxide. A deionized water sample was used as a blank.

ICP-MS. The samples were analyzed by inductively coupled plasma mass spectrometry (ICP-MS) using a Perkin Elmer Elan 6100. Spex CertiPrep ICP/MS grade standard solutions were used to calibrate the instrument for all elements of interest. Ultrapure water (18.3 Mohm cm) from a Barnstedt Nanopure system was used for standard preparation.

2.1.4 Results and Discussion

2.1.4.1 Qualitative Cyclic Voltammetry of NOM.

Effect of Solvent. Previous electrochemical studies of NOM have generally reported CVs with little or no useful structure [17, 34]. We got similar results with aqueous solutions of NOM-PP using a glassy carbon working electrode (Supporting Information, Fig. S1). A Pt working electrode gave a more featurefull CV for aqueous NOM-PP (Supporting Information, Fig. S2), but these features are largely spurious: the cathodic peaks are due to the adsorption of hydrogen and the anodic peaks are due to the subsequent oxidation of the adsorbed hydrogen [35]. The large hydrogen response that we observed with aqueous NOM on Pt is presumably due to reduction of protons. This background caused us to investigate aprotic solvents.

In comparison to aqueous solvent systems, aprotic non-aqueous solvents are often preferred for organic electrochemistry because they offer increased solubility for hydrophobic substances, longer life-times for free radical intermediates, and wider potential ranges that can be studied without interference from redox reactions involving the solvent [36, 37]. Most of this work has been done with DMF or DMSO, so we tried both of these organic solvents with NOM-PP. DMF gave what appeared to be a pair of waves, but without definition as peaks (Fig. 2.2A). In contrast, DMSO gave CVs with sufficiently-well resolved peaks to merit further investigation (Fig. 2.2B). DMSO containing small amounts of H_2O as cosolvent gave results similar to those in aqueous solution (Supporting Information, Fig. S2), so binary combinations of these solvents were not investigated further.

The observed effects of solvent on the CVs of NOM-PP are consistent with the generic advantages of aprotic non-aqueous solvents noted above, although the specifics of how solvents influence the interaction of NOM with Pt electrodes in DMSO will require further investigation. For example, the improved separation of peaks is consistent with stabilization of phenoxy radical intermediates in the absence of a proton donor, but we have not yet obtained direct evidence for the existence of these radicals in our system. It is also likely that solvation in DMSO results in the relaxation of the tertiary (and possibly quaternary) macromolecular structure of NOM [38, 39], thereby making more redox-active moieties accessible to the electrode surface. However, very little seems to be known about the conformational structure of NOM in solvents like DMSO. Finally, it is possible that the improved CVs for NOM in DMSO are due to molecular interactions at the electrode-solvent interface that are specific to this particular system. It is known, for example, that the response of model quinones on Pt electrodes is improved in DMSO because strong chemisorption of DMSO to Pt out-competes the formation of comparatively unreactive surface complexes between the quinone moieties and Pt [40]. If quinones are the redox-active moieties in NOM, then this effect might contribute to the improved electrode response we see in DMSO.

Interpretation of the CVs. The major features of the CV of NOM-PP in DMSO are labeled in Fig. 2.2B. Each cycle was started at -0.25 V, ramped linearly to a more negative potential (cathodic sweep), then to a more positive potential (anodic sweep), and back to the starting potential. On the first cathodic sweep, a sufficiently negative potential was eventually reached to transfer electrons from the electrode to redox-active moieties associated with NOM, and this results in a sharply more negative (cathodic) current. Under diffusion controlled conditions, the material available to be reduced at the electrode interface is rapidly used up, resulting in less cathodic current, which forms a peak in the CV (1C in Fig. 2.2B). At still more negative potentials, the sequence is repeated, forming a second cathodic peak (2C). On the anodic sweep, electrons are transferred from the NOM to the electrode, resulting in two anodic peaks (2A and 1A).

In most cases, the potential was cycled between –0.25 and –2.0 V four times. The sharp increase in current at the switching potentials (potentials at which the scan is reversed) is due to solvent breakdown. The agreement among the current responses for these potential cycles indicates that the redox-active moieties of NOM-PP do not undergo significant chemical side-reactions that produce non-electroactive species.

Although not as well defined as the CVs for NOM-PP, the unfractionated NOM-GT (Fig. 2.3A) gave CVs in DMSO that suggest at least one pair of waves. The CV for NOM-CH (Fig. 2.3B) does not show features that can be interpreted reliably. The differences between the CVs of NOM-PP vs. NOM-GT and NOM-CH suggest that the procedure used to obtain the NOM-PP fraction does enrich some of the redox-active functionality associated with the parent material. This supports results from a separate study of these NOM fractions, wherein spectroscopic data was used to conclude that the NOM-PP fraction contained the highest concentrations of phenolic and ketonic functional groups (26, 27).

CVs of NOM from a wide variety of other sources are provided as Supporting Information. All of the NOM fractions studied produced a current response at the electrode surface, but most gave only weakly defined CVs. The collective data set can be grouped into 5 categories based on the shape of their CVs. The most well-defined CVs

(those most resembling the CVs of the model quinones discussed below) include NOM-PP, P-FA, and PB-NOM. P-HA and LF-FA gave CVs that showed a single pair of peaks. SR-FA and FA(II) gave only a single well defined cathodic peak. The unfractionated NOM-GT, NOM-CH, S-HA, SD-HA, and MN-NOM samples gave CVs that were less well-defined, but for which several peaks were apparent. AL-HA makes up the last category: its CV showed no definition and no apparent redox response.

Possible explanations for the differences among the CVs of NOM include: (i) differences in NOM structure due to differences in origin, (ii) variable degrees of electrode passivation due to differences in adsorbtivity of NOM on Pt, and (iii) overlapping mixed electrode potentials due to the range of redox-active moieties associated with NOM. The possible role of variations in metal content and aromaticity are addressed below in the section on correlation analysis. It is interesting that only Aldrich humic acid (AL-HA) gave no current response at all, as others have noted previously that this material can be atypical of NOM [41].

2.1.4.2. Quantitative Cyclic Voltammetry of NOM:

Stationary electrode results. Electrochemical reversibility is an operational concept that is dependent on the properties of the compound as well as the experimental parameters used. CVs of reversible (Nernstian) electrochemical reactions typically exhibit pairs of cathodic and anodic peaks where the difference between peak potentials (ΔE_p) is 0.059/n V (where n is the number of electrons transferred) and the ratio of the anodic and cathodic peak currents (i_p^A/i_p^C) is close to unity [36, 42]. Under these conditions, the half-wave potential ($E_{1/2}$), the potential midway between E_p^C and E_p^A, is an accurate measure of the formal redox potential ($E^{o'} = (E_p^A+E_p^C)/2$). Furthermore, the i_p's should conform to the Randles-Sevcik equation ($i_p = (2.69x10^5)n^{3/2}AD^{0.5}C\nu^{0.5}$, where A is the area of the electrode surface (cm^2); D is the diffusion coefficient ($cm^2\ s^{-1}$); C is concentration (mole cm^{-3}); and ν is the scan rate ($V\ s^{-1}$). This relationship predicts that i_p will increase linearly with $\nu^{0.5}$ and C, and these two relationships are commonly used as

tests for reversibility [36, 42]. Additionally, the CV reflects diffusion controlled electrode reactions (and complicating side reactions are absent) when each E_p is independent of v.

The value of ΔE_p that we observed for NOM-PP (Table 2.1) is larger than the theoretical value of 0.059 V for reversible one-electron transfer. Instead, it falls within the range that is typical of quasi-reversible reactions [36, 42]. Quasi-reversible reactions—which are fairly common in organic electrochemistry—usually exhibit kinetics of electron transfer that are slower than is required for a reversible reaction, but fast enough to give a well-defined pair of anodic and cathodic peaks. However, in this case, quasi-reversibility could also be due to minor side reactions of the oxidized or reduced moieties or conformational changes brought on by changes in speciation. The increased ΔE_p's observed for the NOM-PP fraction along with the model quinones could also be due to uncompensated solution resistance.

The effects of v and C on the CV for NOM-PP are shown in Fig. 2.4. The four values of E_p are slightly dependent on v, plots of i_p versus $v^{0.5}$ are linear ($r^2 = 0.999$ for all four peaks, data not shown), and a plot of i_p for the first cathodic wave versus C is also linear ($r^2 = 0.998$, also not shown). Taken together, these results suggest that the peaks in the CV of NOM-PP reflect quasi-reversible one-electron transfer with diffusion controlled kinetics. Note, however, that values of i_p could not be determined for some values of E_p , due mainly to uncertainties in estimating a baseline current, and these cases result in values of i_p that are missing from Table 2.1.

Hydrodynamic Electrode Results. Hydrodynamic electrodes, such as the rotating disk electrode (RDE), allow control of reactant mass transport to the electrode surface. Under conditions where the profile of reactant concentration across the boundary layer is at steady-state, electron transfers are manifest as steps rather than peaks [43]. Figure 2.5A shows CVs for NOM-PP over a range of electrode rotation rates. As expected, the RDE gave larger current steps at faster rotation rates due to increased flux of NOM to the electrode surface. The RDE also gave larger overall currents than the stationary electrode (due to its larger diameter and increased mass transport of reactant to the electrode) and more negative peak potentials (presumably due to indeterminate differences in electrode

composition and surface condition). For comparison with the RDE results obtained with NOM-PP, Fig. 2.5B shows the CVs for a model quinone, menadione. In this case, the two steps are certainly due to two one-electron transfers (see below). The results in Fig. 2.5A, and the comparison with results in Fig. 2.5B, reinforce conclusions drawn based on stationary electrode data (Fig. 2.2-2.4), that the electrode response of NOM-PP reflects two one-electron transfers most probably involving quinonoid moieties.

2.1.4.3. Cyclic Voltammetry of Model Compounds

In order to help relate the redox activity we observed with NOM fractions to specific redox-active functional groups, we studied a variety of model ortho-quinones using our experimental protocol. We chose several quinones that have been used previously as NOM model compounds and others that are known to be involved in respiratory processes. Anthraquinone-2,6-disulfonate (AQDS) was among the first model quinones used to represent NOM (12). Two naphthoquinones were included, juglone and lawsone, because they also have been used as NOM model compounds (13). Menaquinone and ubiquinone were included in this study because these isoprenyl quinones are involved in cellular respiration and photosynthesis. These isoprenyl quinones have been associated with cellular exudates from *Shewanella putrefaciens* and may serve as extracellular electron shuttles [44].

The CVs for AQDS and menaquinone-4 are shown in Fig. 2.6. Both are typical of CVs reported by others for quinones in aprotic solvents [45]. In each case, the two pairs of peaks reflect sequential single electron transfers with an intermediate semiquinone radical (i.e., $Q + e^- \leftrightarrow Q^{\bullet -}$ and $Q^{\bullet -} + e^- \leftrightarrow Q^{=}$). Two sets of well-defined peaks were also observed for the other model quinones, and these CVs are given as Supporting Information. Quantitative characteristics of these peaks (E_p, $E_{p/2}$, ΔE_p, and i_p^A/i_p^C) are given in Table 2.1. For all the quinone model compounds studied, ΔE_p was > 0.059/n V and therefore in the quasi-reversible range, i_p^A/i_p^C was close to unity, E_p's were weakly dependent on ν, and values of i_p were linearly related to $\nu^{0.5}$ and C (data not shown).

Thus, by all of these criteria, the electrode response of the model quinones was very similar to that of NOM-PP, under the conditions of our study.

There is a vast amount of literature on the electrochemistry of quinones in aprotic solvents [46-49]. Some of the model quinones we studied gave CVs in DMSO with peculiarities that are worthy of note because they may reflect chemical properties that are important under environmental conditions. For example, the first electron transfer for lawsone gave an irreversible peak, which is presumably due to a slow rate of electron transfer with respect to the scan rate [36, 42]. In addition, the second electron transfer for juglone (and to a lesser extent, lawsone) gave a pair of peaks with well-defined shoulders, which probably reflects involvement of the extra hydroxyl group (Fig. 2.1). We did not, however, investigate these observations further.

2.1.5. Correlation analysis

The numerous similarities between the CVs of the model quinones and some fractions of NOM (especially NOM-GT) may be evidence that quinonoid moieties are predominantly responsible for the redox activity of NOM. However, some metal-organic complexes (including porphyrins) give CVs that are qualitatively similar to those that we have observed with the quinone model compounds [50]. To help distinguish between these possibilities, we have performed a correlation analysis among quantifiable electrochemical properties and a variety of other chemical and spectroscopic properties that we determined for the majority of the NOMs surveyed in this study. Most of the data used in this analysis are included in Tables 2.1 and 2.2, and the correlations are summarized in a matrix of scatter plots, which is included as Supporting Information.

For spectroscopic characterization, we used UV/Vis adsorbance because this method is the most widely used for preliminary characterization of NOM [51]. UV-Vis absorbance spectra of NOM usually contain few features except a steep decay in absorbance as wavelength increases above a few hundred nm. However, a variety of quantitative metrics have proven to be useful in characterizing these spectra: including the absorbance at 280 nm (A_{280}), the ratio of absorbances at 254 and 365 nm (E_2/E_3) or

465 and 665 nm (E_4/E_6), and the carbon-normalized UV absorbance at 254 nm (SUVA). In general, higher values of A_{280} and SUVA and lower E_2/E_3, and E_4/E_6 ratios are associated with greater aromaticity and degree of humification [52, 53]. More sophisticated analysis of the UV-Vis absorbance spectra of NOM have been interpreted in terms of electronic transitions that are typical of aromatic compounds [54], and similar but potentially more diagnostic analyses are possible with fluorescence spectra [55-58].

Our results (Table 2.2 and Supporting Information) show that the NOM fraction with the most clearly defined CV (NOM-PP) has a higher A_{280}, lower E_4/E_6 ratio, and higher SUVA than the carbohydrate fraction (NOM-CH). This suggests that the NOM-PP fraction has a higher aromaticity, which is consistent with the expectation that this fractionation was enriched in polyphenols [26, 27]. Other NOM fractions gave UV-Vis absorbance spectra that are quite variable, but the humic fractions generally have higher A_{280} and SUVA numbers and lower E_2/E_3, and E_4/E_6 ratios for the fulvic fractions. However, considering the whole range of NOMs studied, no strong correlations are apparent between the spectroscopic properties and the electrochemical properties.

For characterization of chemical composition, we measured 14 trace metals by ICP-MS for all of the NOMs included in this study. Since samples of NOM can contain variable amounts of trace metals and some of these metals are redox active, it was possible that the electrode activity we observed might correlate with their metal content. Results for the four most relevant metals (Fe, Ni, Zn, Cu) are included in Table 2.2 and the scatter plot matrix is in the Supporting Information. The data for Zinc in P-FA plot as an outlier. The fact that P-FA gave a CV similar to NOM-PP and PB-NOM, indicates that metals did not impart significant electrode activity. This conclusion also appears to be true in general, since there was no correlation between any of the metal contents and degree of electrode response. In future work, we hope to extent this analysis to include data from various assays of putative quinone content of NOM.

2.1.6. Implications

To facilitate comparisons among the electrochemical properties of the NOM samples, fractions of NOM, and NOM model compounds that were included in this study, we have summarized the peak potentials obtained from stationary electrode data in Fig. 2.7. Both E_p's and $E_{p/2}$'s are included for each well-defined peak, and pairs of peaks (cathodic and anodic) are included for each reversible or quasi-reversible electron transfer. Therefore, a compound that exhibits two quasi-reversible electron transfers, such as menaquinone-4 (MQ-4), is represented in Fig. 2.7 by four E_p's and four $E_{p/2}$'s. In many cases, some of the peak potentials are overlapping or not available, so fewer points appear on the plot, but the presentation does facilitate relative comparisons among the compounds studied. In general, the peak potentials that we obtained with samples of NOM are more positive than the corresponding potentials for the model quinones. Only juglone exhibits peak potentials that are typical of most NOMs.

Figure 2.7 can also be used to compare the kinetics of electron transfer among the compounds studied. Since all CVs were taken at the same scan rate, the potential difference between E_p and $E_{p/2}$ for any particular peak reflects the kinetics of the electron transfer that produced that peak. Larger separation between corresponding values of E_p and $E_{p/2}$, and therefore longer horizontal bars in Figure 2.7, indicate slower kinetics of electrode reaction. Although the apparent kinetics of electron transfer are generally similar where two-electron transfers were observed for any one material, there is considerable variability in the kinetics of electron transfer among the NOMs and even among the model quinones. For example, electron transfer involving MQ-4 is comparatively slow, AQDS is fast, and juglone is intermediate. As with the peak potentials, the kinetics of electron transfer for juglone are more representative of most NOMs than the other model quinones.

Perhaps the ultimate outcome of this work would be to derive formal potentials that accurately reflect that aggregate behavior of NOM as if it were a single redox couple, under conditions that were comparable to commonly available formal potentials for other environmentally significant couples. This might allow comparisons between our results

and estimates of the formal potential of NOM developed previously using less direct methods (e.g., [59-62]). Unfortunately, the experimental conditions that we found were necessary to obtain representative formal potentials greatly complicate the problem of making them comparable to potentials under standard environmental conditions. Part of this problem is that our potentials were measured vs. a Ag/Ag^+ reference electrode in DMSO, so they are not directly comparable to potentials measured vs. any of the reference electrodes that are commonly used under aqueous conditions.

An approximate correction for the difference in reference electrodes can be made by normalizing potentials measured in each system to a reference reaction that is well behaved in both solvent systems. Using the pH-independent, reversible one-electron couple ferrocene/ferrocenium as in reference [62], we found that the potential in DMSO vs. Ag/Ag^+ equals the potential in H_2O vs. SHE plus 0.45 V. Applying this correction to peak potentials that we measured for the two-electron transfers to NOM-PP gives estimated formal potentials of –0.4 V and –0.97 V vs. SHE under aqueous conditions. Unfortunately, these numbers are still not directly comparable to formal potentials under environmental conditions, because the effect of pH could not be determined for solutions of DMSO and the effects of solvation on the structure of NOM are unknown. Some of these limitations may eventually be overcome after a wider range of reference reactions have been studied under conditions similar to the method developed in this study.

2.1.7. Acknowledgments

This research was sponsored by the Natural and Accelerated Bioremediation Research (NABIR) Program, Office of Biological and Environmental Research, U.S. Department of Energy, under contract DE-AC05-00OR22725 with the Oak Ridge National Laboratory. Baohua Gu (ORNL), George Aiken (US Geological Survey, Boulder, CO), Donald Macalady (Colorado School of Mines), Yu-Ping Chin (Ohio State University), and John Coates (Southern Illinois University) provided some of the samples of NOM and NOM fractions. Some of the electrochemical data was collected by Jacob Spendelow, with support from the Camille & Henry Dreyfus Foundation. The ICP/MS

analysis were performed by D. Baron at the University of California, Bakersfield, with an instrument acquired with funds from the Air Force Office of Scientific Research. We would also like to thank Petr Zuman and Robin Helburn for useful suggestions at various stages of this project.

2.1.8. References

[1] Lovley, D. R.; Coates, J. D.; BluntHarris, E. L.; Phillips, E. J. P.; Woodward, J. C. Humic substances as electron acceptors for microbial respiration *Nature* **1996**, *382*, 445-448.

[2] Goodman, B. A. In *Iron in Soils and Clay Minerals*; Stucki, J. W., Goodman, B. A., Schwertmann, U., Eds.; Reidel: Dordrecht, 1988; Vol. C217, pp 677-687.

[3] Seeliger, S.; Cord-Ruwisch, R.; Schink, B. A periplasmic and extracellular c-type cytochrome of *Geobacter sulfurreducens* acts as a ferric iron reductase and as an electron carrier to other acceptors or to partner bacteria *J. Bacteriol.* **1998**, *180*, 3686-3691.

[4] Buschmann, J.; Angst, W.; Schwarzenbach, R. P. Iron porphyrin and cysteine mediated reduction of ten polyhalogenated methanes in homogeneous aqueous solution: Product analyses and mechanistic considerations *Environ. Sci. Technol.* **1999**, *33*, 1015-1020.

[5] Lesage, S.; Xu, H.; Durham, L. The occurrence and roles of porphyrins in the environment: Possible implications for bioremediation *Hydrol. Sci.* **1993**, *38*, 343-354.

[6] Glaus, M. A.; Heijman, C. G.; Schwarzenbach, R. P.; Zeyer, J. Reduction of nitroaromatic compounds mediated by *Streptomyces* sp. exudates *Appl. Environ. Microbiol.* **1992**, *58*, 1945-1951.

[7] Dunnivant, F. M.; Schwarzenbach, R. P.; Macalady, D. L. Reduction of substituted nitrobenzenes in aqueous solutions containing natural organic matter *Environ. Sci. Technol.* **1992**, *26*, 2133-2141.

[8] Macalady, D. L.; Ranville, J. F. In *Perspectives in Environmental Chemistry*; Macalady, D. L., Ed.; Oxford: New York, 1998; pp 94-137.

[9] Collins, R.; Picardal, F. Enhanced anaerobic transformations of carbon tetrachloride by soil organic matter *Environ. Toxicol. Chem.* **1999**, *18*, 2703-2710.

[10] Lovley, D. R.; Fraga, J. L.; Blunt-Harris, E. L.; Hayes, L. A.; Phillips, E. J. P.; Coates, J. D. Humic substances as a mediator for microbially catalyzed metal reduction *Acta Hydrochim. Hydrobiol.* **1998**, *26*, 152-157.

[11] Scott, D. T.; McKnight, D. M.; Blunt-Harris, E. L.; Kolesar, S. E.; Lovley, D. R. Quinone moieties act as electron acceptors in the reduction of humic substances by humics-reducing microorganisms *Environ. Sci. Technol.* **1998**, *32*, 2984-2989.

[12] Tratnyek, P. G.; Macalady, D. L. Abiotic reduction of nitro aromatic pesticides in anaerobic laboratory systems *J. Agric. Food Chem.* **1989**, *37*, 248-254.

[13] Schwarzenbach, R. P.; Stierli, R.; Lanz, K.; Zeyer, J. Quinone and iron porphyrin mediated reduction of nitroaromatic compounds in homogeneous aqueous solution *Environ. Sci. Technol.* **1990**, *24*, 1566-1574.

[14] Curtis, G. P.; Reinhard, M. Reductive dehalogenation of hexachloroethane, carbon tetrachloride, and bromoform by anthrahydroquinone disulfonate and humic acid *Environ. Sci. Technol.* **1994**, *28*, 2393-2401.

[15] Perlinger, J. A.; Angst, W.; Schwarzenbach, R. P. Kinetics of the reduction of hexachloroethane by juglone in solutions containing hydrogen sulfide *Environ. Sci. Technol.* **1996**, *30*, 3408-3417.

[16] Royer, R. A.; Burgos, W. D.; Fisher, A. S.; Unz, R. F. In *220th ACS National Meeting*; Division of Environmental Chemistry, American Chemical Society: Washington, DC, 2000; Vol. 40, No. 2, pp 441-443.

[17] Helburn, R. S.; MacCarthy, P. Determination of some redox properties of humic acid by alkaline ferricyanide titration *Anal. Chim. Acta* **1994**, *295*, 263-272.

[18] Kolthoff, I. M.; Lingane, J. J. *Polarography*; 2nd ed.; Wiley: New York, 1952.

[19] Lucena-Conde, F.; Gonzalez-Crespo, A. In *7th International Congress of Soil Science*: Madison, WI, 1960; pp 59-65.

[20] Greter, F.-L.; Buffle, J.; Haerdi, W. Voltammetric study of humic and fulvic substances: Part I. Study of the factors influencing the measurement of their complexing properties with lead *J. Electroanal. Chem.* **1979**, *101*, 211-229.

[21] Plavsic, M.; Cosovic, B. Influence of surface-active substances on the redox processes of metal ions: a contribution to the speciation analysis of metals in aquatic systems *Anal. Chim. Acta* **1994**, *284*, 539-545.

[22] Xue, H. B.; Sigg, L. Comparison of the complexation of Cu and Cd by humic or fulvic acids and by ligands observed in lake waters *Aquatic Geochemistry* **1999**, *5*, 313-335.

[23] Nurmi, J. T.; Tratnyek, P. G. In *220th ACS National Meeting*; Division of Environmental Chemistry, American Chemical Society: Washington, DC, 2000; Vol. 40, No. 2, pp 418-421.

[24] Gu, B.; Schmitt, J.; Chen, Z.; Liang, L.; McCarthy, J. F. Adsorption and desorption of different organic matter fractions on iron oxide *Geochim. Cosmochim. Acta* **1995**, *59*, 219-229.

[25] Lowe, L. E. Fractionation of acid-soluble components of soil organic matter using polyvinyl pyrrolidone *Canad. J. Soil Sci.* **1975**, *55*, 119-126.

[26] Reznickova, J. G.; Hippler, H.; Striebel, F.; Tevzadze, L. A saturated LIF study on the high pressure limiting rate constant of the reaction CN + NO + M -> NCNO + M between 200 and 600 K *Zeitschrift fuer Physikalische Chemie (Muenchen)* **2000**, *214*, 1115-1136.

[27] Tollefsrud, E.; Schreier, C. G. In *Third International Conference on Remediation of Chlorinated and Recalcitrant Compounds*; Gavaskar, A. R., Chen, A. S. C., Eds.; Battelle Press: Monterey, CA, 2002; pp Paper 2C-16.

[28] Thorn, K. A.; Arterburn, J. B.; Mikita, M. A. ^{15}N and ^{13}C NMR investigation of hydroxylamine-derivatized humic substances *Environ. Sci. Technol.* **1992**, *26*, 107-116.

[29] Averett, R. C.; Leenheer, J. A.; McKnight, D. M.; Thorn, K. A. "Humic Substances in the Suwannee River, Georgia; Interactions, Properties, and Proposed Structures," U.S. Geological Survey, 1994.

[30] McKnight, D. M.; Andrews, E. D.; Spaulding, S. A.; Aiken, G. R. Aquatic fulvic acids in algal-rich antarctic ponds *Limnol. Oceanogr.* **1994**, *39*, 1972-1979.

[31] Leenheer, J. A.; Brown, G. K.; MacCarthy, P.; Cabaniss, S. E. Models of metal binding structures in fulvic acid from the Suwannee River, Georgia *Environ. Sci. Technol.* **1998**, *32*, 2410-2416.

[32] Cabaniss, S.; Zhou, Q.; Maurice, P. A.; Chin, Y.-P.; Aiken, G. R. A log-normal distribution model for the molecular weight of aquatic fulvic acids *Environ. Sci. Technol.* **2000**, *34*, 1103-1109.

[33] Mao, J.-D.; Hu, W.-G.; Schmidt-Rohr, K.; Davies, G.; Ghabbour, E. A.; Xing, B. Quantitative characterization of humic substances by solid-state carbon-13 nuclear magnetic resonance *Soil Sci. Soc. Am. J.* **2000**, *64*, 873-884.

[34] Motheo, A. J.; Pinhedo, L. Electrochemical degradation of humic acid *Sci. Total Environ.* **2000**, *256*, 67-76.

[35] Doña Rodríguez, J. M.; Alberto Herrera Melián, J.; Pérez Peña, J. Determination of the real surface area of Pt electrodes by hydrogen adsorption using cyclic voltammetry *J. Chem. Educ.* **2000**, *77*, 1195-1197.

[36] Sawyer, D. T.; Sobkowiak, A.; Roberts, J. L. J. *Electrochemistry for Chemists*; 2nd ed.; Wiley: New York, 1995.

[37] Zuman, P. In *Advances in Physical Organic Chemistry*; Gold, V., Ed.; Academic: London, 1967; Vol. 5, pp 1-52.

[38] Varga, B.; Kiss, G.; Galambos, I.; Gelencsér, A.; Hlavay, J.; Krivácsy, Z. Secondary structure of humic acids. Can micelle-like conformtion be proved by aqueous size exclusion chromatography *Environ. Sci. Technol.* **2000**, *34*, 3303-3306.

[39] Wershaw, R. L. Model for humus in soils and sediments *Environ. Sci. Technol.* **1993**, *27*, 814-816.

[40] Hubbard, A. T. Electrochemistry at well-characterized surfaces *Chem. Rev.* **1988**, *88*, 633-656.

[41] Malcolm, R. L.; MacCarthy, P. Limitations in the use of commercial humic acids in water and soil research *Environ. Sci. Technol.* **1986**, *20*, 904-911.

[42] Bard, A. J.; Faulkner, L. R. *Electrochemical Methods. Fundamentals and Applications*; Wiley: New York, 1980.

[43] Nikolic, J.; Expósito, E.; Iniesta, J.; González-García, J.; Montiel, V. Theoretical concepts and applications of a rotating disk electrode *J. Chem. Educ.* **2000**, *77*, 1191-1194.

[44] Newman, D. K.; Kolter, R. A role for excreted quinones in extracellular electron transfer *Nature* **2000**, *405*, 94-97.

[45] Gupta, N.; Linschitz, H. Hydrogen-bonding and protonation effects in electrochemistry of quinones in aprotic solvents *J. Am. Chem. Soc.* **1997**, *119*, 6384-6391.

[46] Kolthoff, I. M.; Reddy, T. B. Polarography and voltammetry in dimethylsulfoxide *J. Electrochem. Soc.* **1961**, *108*, 980-985.

[47] Chambers, J. Q. In *The Chemistry of the Quinonoid Compounds*; Patai, S., Ed.; Interscience: New York, 1974; Vol. 2, pp 737-791.

[48] Petrova, S. A.; Kolodyazhny, M. B.; Ksenzhek, O. S. Electrochemical properties of some naturally occurring quinones *J. Electroanal. Chem.* **1990**, *277*, 189-196.

[49] Zuman, P. Das polarographische verhalten des juglons und seine bestimmung in gegenwart von ascorbinsaure in den fruchten und grunene teilen des nussbaums (*Juglans regia*) *Collection Czechoslov. Chem. Commun.* **1954**, *19*, 1140-1149.

[50] Kadish, K. M.; van Caemelbecke, E.; Royal, G. In *The Porphyrin Handbook*; Kadish, K. M., Smith, K. M., Guilard, R., Eds.; Academic: San Diego, 2000; Vol. Vol. I, Synthesis and Organic Chemistry, pp 1-114.

[51] Bloom, P. R.; Leenheer, J. A. In *Humic Substances II. In Search of Structure*; Hayes, M. H. B., MacCarthy, P., Malcolm, R. L., Swift, R. S., Eds.; Wiley: Chichester, 1989; pp 409-446.

[52] Diau, E. W.; Yu, T.; Wagner, M. A. G.; Lin, M. C. Kinetics of the NH2 + NO Reaction: Effects of Temperature on the Total Rate Constant and the OH/H2O Branching Ratio *Journal of Physical Chemistry* **1994**, *98*, 4034-4042.

[53] Peuravuori, J.; Pihlaja, K. Molecular size distribution and spectroscopic properties of aquatic humic substances. *Anal. Chim. Acta* **1997**, *337*, 133-149.

[54] Korshin, G. V.; Li, C.-W.; Benjamin, M. M. Monitoring the properties of natural organic matter through UV spectroscopy: A consistent theory *Wat. Res.* **1997**, *31*, 1787-1795.

[55] McKnight, D. M.; Boyer, E. W.; Westerhoff, P. K.; Doran, P. T.; Kulbe, T.; Andersen, D. T. Spectrofluorometric characterization of dissolved organic matter for indication of precursor organic material and aromaticity *Limnol. Oceanogr.* **2001**, *46*, 38-48.

[56] Mobed, J. J.; Hemmingsen, S. L.; Autry, J. L.; McGown, L. B. Fluorescence characterization of IHSS humic substances: Total luminescence spectra with absorbance correction *Environ. Sci. Technol.* **1996**, *30*, 3061-3065.

[57] Pullin, M. J.; Cabaniss, S. E. Rank analysis of the pH-Dependent synchronous fluorescence spectra of sir standard humic substances *Environ. Sci. Technol.* **1995**, *29*, 1460-1467.

[58] Green, S. A.; Blough, N. V. Optical absorption and fluorescence properties of chromophoric dissolved organic matter in natural waters *Limnol. Oceanogr.* **1994**, *39*, 1903-1916.

[59] Szilágyi, M. The redox properties and the determination of the normal potential of the peat-water system *Soil Sci.* **1973**, *115*, 434-437.

[60] Wilson, S. A.; Weber, J. H. An EPR study of the reduction of vanadium(V) to vanadium(IV) by fulvic acid *Chem. Geol.* **1979**, *26*, 345-354.

[61] Skogerboe, R. K. Reduction of ionic species by fulvic acid *Anal. Chem.* **1981**, *53*, 228-232.

[62] Dassbjerg, K.; Pedersen, S. U.; Lund, H. In *General Aspects of the Chemistry of Radicals*; Alfassi, Z. B., Ed.; Wiley: Chichester, 1999; pp 385-427.

Table 2.1. Summary of electrochemical data.

Sample	Peak 1						Peak 2					
	E_p^{1C}	$E_{p/2}^{1C}$	E_p^{1A}	$E_{p/2}^{1A}$	ΔE_p	i_p^A/i_p^C	E_p^{2C}	$E_{p/2}^{2C}$	E_p^{2A}	$E_{p/2}^{2A}$	ΔE_p	i_p^A/i_p^C
NOM-PP	-0.93	-0.83	-0.77	-0.87	0.16	0.9	-1.50	-1.40	-1.34	-1.46	0.16	0.9
P-FA	-1.17	-1.09	-0.99	-1.07	0.18		-1.48	-1.37				
PB-NOM	-1.12	-1.07					-1.57	-1.47				
P-HA	-1.32	-1.24	-0.93	-1.00	0.39							
LF-HA	-1.37	-1.23	-1.00	-1.27	0.37							
FA(II)	-1.67	-1.47										
SR-FA	-1.5	-1.37										
MQ-4	-1.27	-1.04	-0.68	-0.89	0.59	0.9	-1.99	-1.84	-1.58	-1.72	0.41	1.2
UQ-5	-0.98	-0.87	-0.72	-0.82	0.26	1.0	-1.69	-1.51	-1.48	-1.56	0.21	
Menadione	-1.19	-0.99	-0.70	-0.88	0.49	1.1	-1.88	-1.75	-1.54	-1.68	0.34	
Juglone	-0.78	-0.70	-0.65	-0.74	0.13	0.9	-1.43	-1.28	-1.21	-1.37	0.22	0.9
Lawsone	-0.89	-0.82					-1.64	-1.52	-1.42	-1.57	0.22	0.8
AQDS	-1.12	-1.05	-0.99	-1.06	0.13	0.8	-1.75	-1.68	-1.62	-1.69	0.13	
Ferrocene	0.13	0.21	0.30	0.22	0.17	1.0						

Table 2.2. Summary of NOM properties.

	A_{280}	E_2/E_3	E_4/E_6	SUVA (L mg-1 C)	Fe,Ni,Zn,Cu (μg g-1 NOM)
NOM-PP	0.32	3.9	11	0.042	542,35.6,12.6,4.4
P-FA	0.35	5.1	23	0.050	4325,43.5,1155,306
PB-NOM					30365,4.4,50.8,108.5
P-HA	0.54	2.7	6.1	0.064	520,8.4,28.8,6.4
LF-FA	0.11	7.9	ND	0.016	83,4.05,15.6,45.5
FA(II)	0.36	4.2	17	0.046	412,12,29,46.8
SR-FA	0.22	4.7	49	0.030	26,1.65,19.6,2.1
NOM-GT	0.28	4.1	6.9	0.037	5268,21.8,39,10.6
NOM-CH	0.07	4.8	38	0.009	268,15.2,15.2,4.6
S-HA	0.61	2.2	4.2	0.070	456,7.2,41.2,179
MN-NOM					127.5,9,139,10
AL-HA	0.33	2.4	3.4	0.039	7716,14.8,25.6,22.8

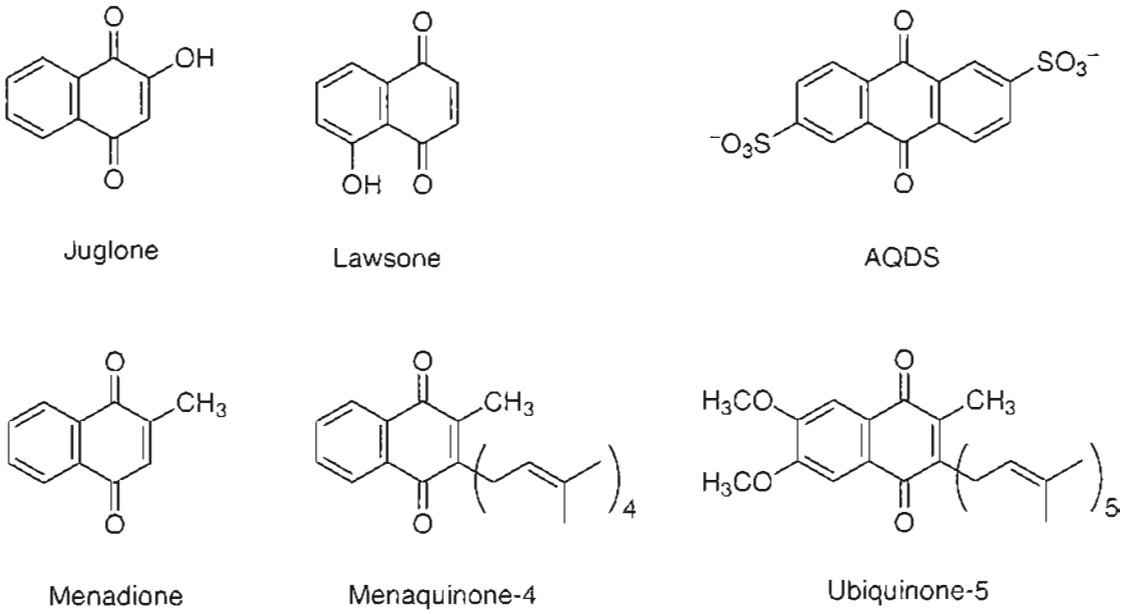

Figure 2.1. Chemical structures of NOM model quinones

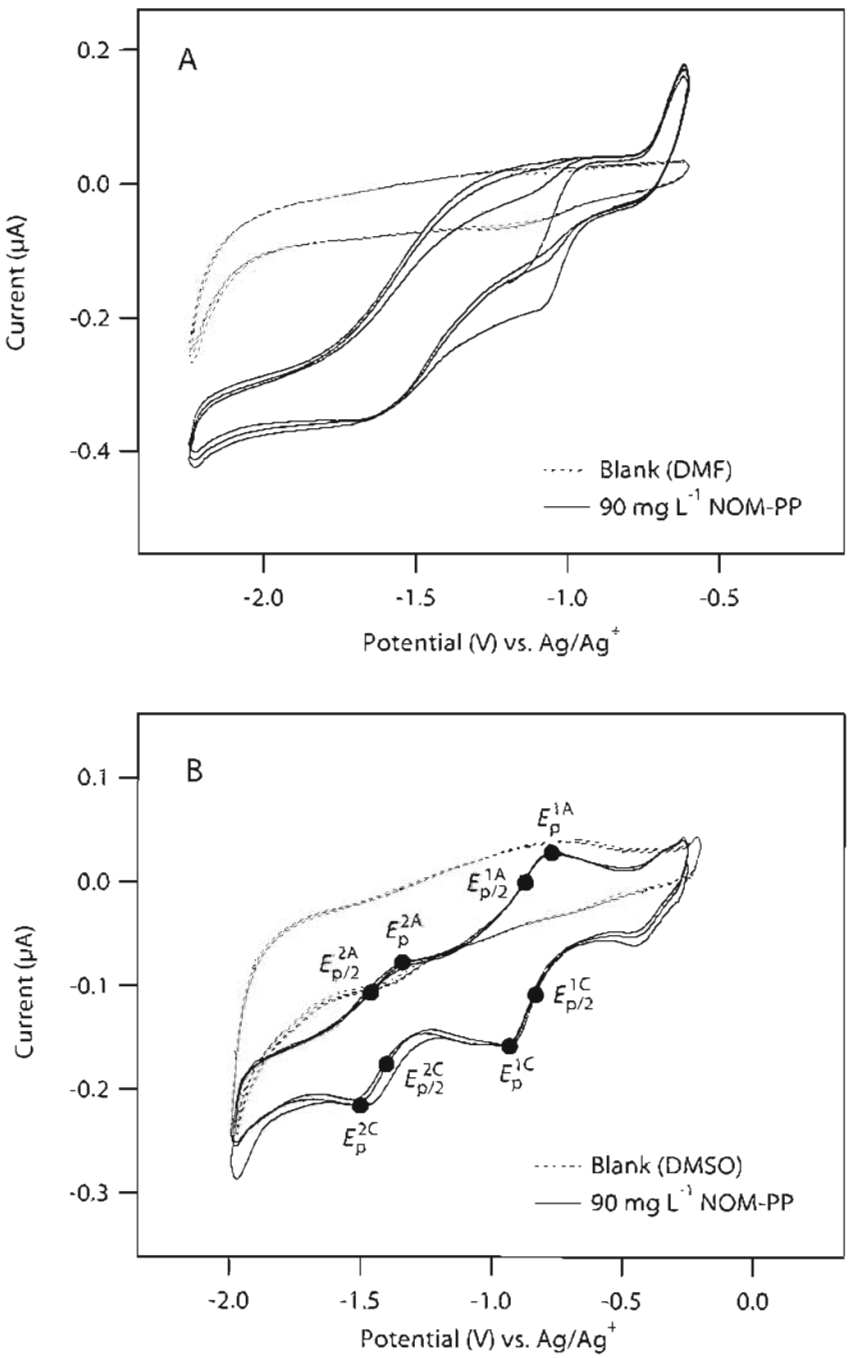

Figure 2.2. CVs of NOM-PP under nonaqueous conditions in (A) DMF and (B) DMSO. Working electrode: Pt disk (1.6-mm diameter). Electrolyte: 1.0 mM $NaClO_4$. Scan rate: 10 mV s^{-1}

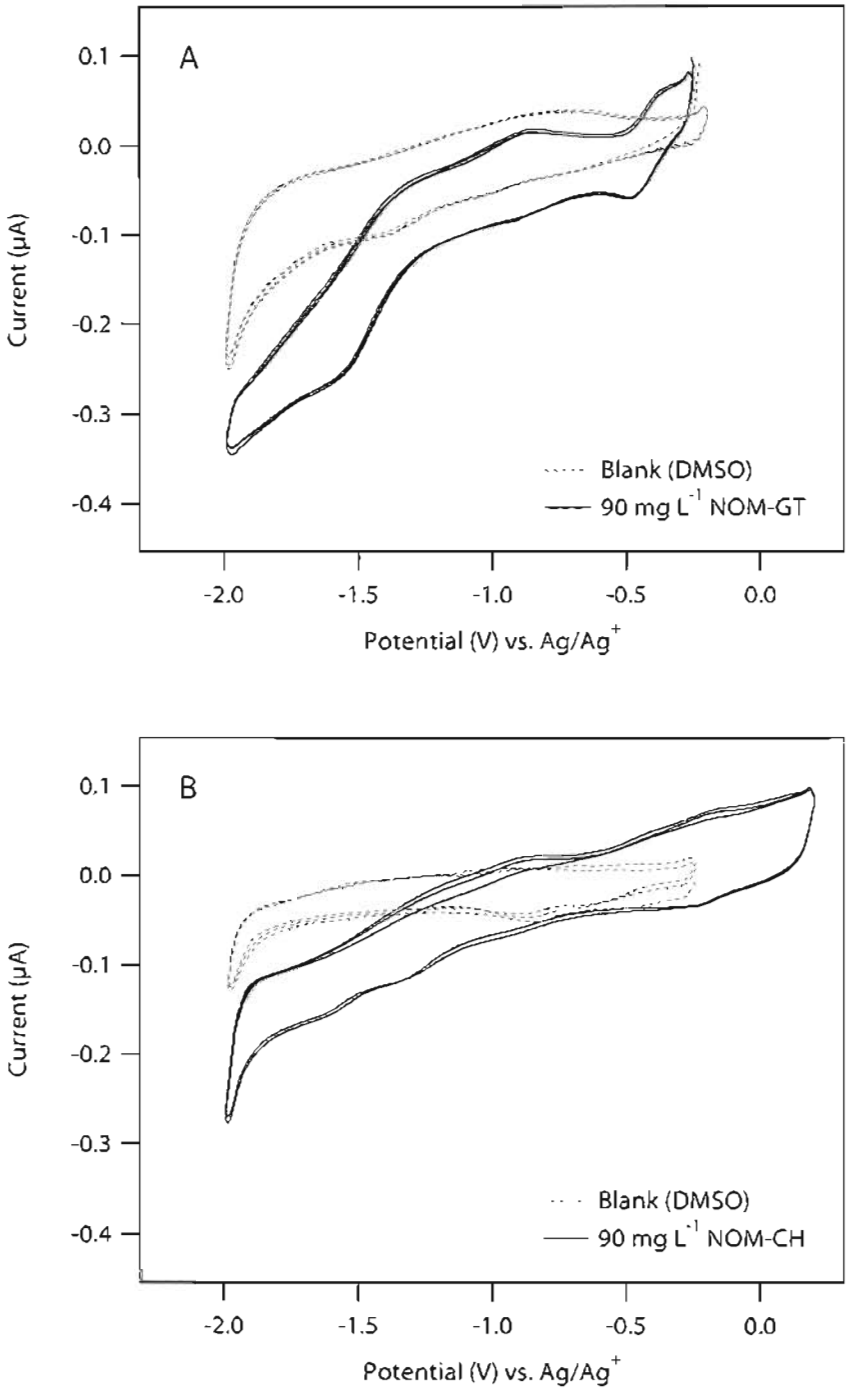

Figure 2.3. CVs of (A) NOM-GT and (B) NOM-CH. Working electrode: Pt disk (1.6-mm diameter). Electrolyte: 1.0 mM $NaClO_4$. Scan rate: 10 mV s^{-1}

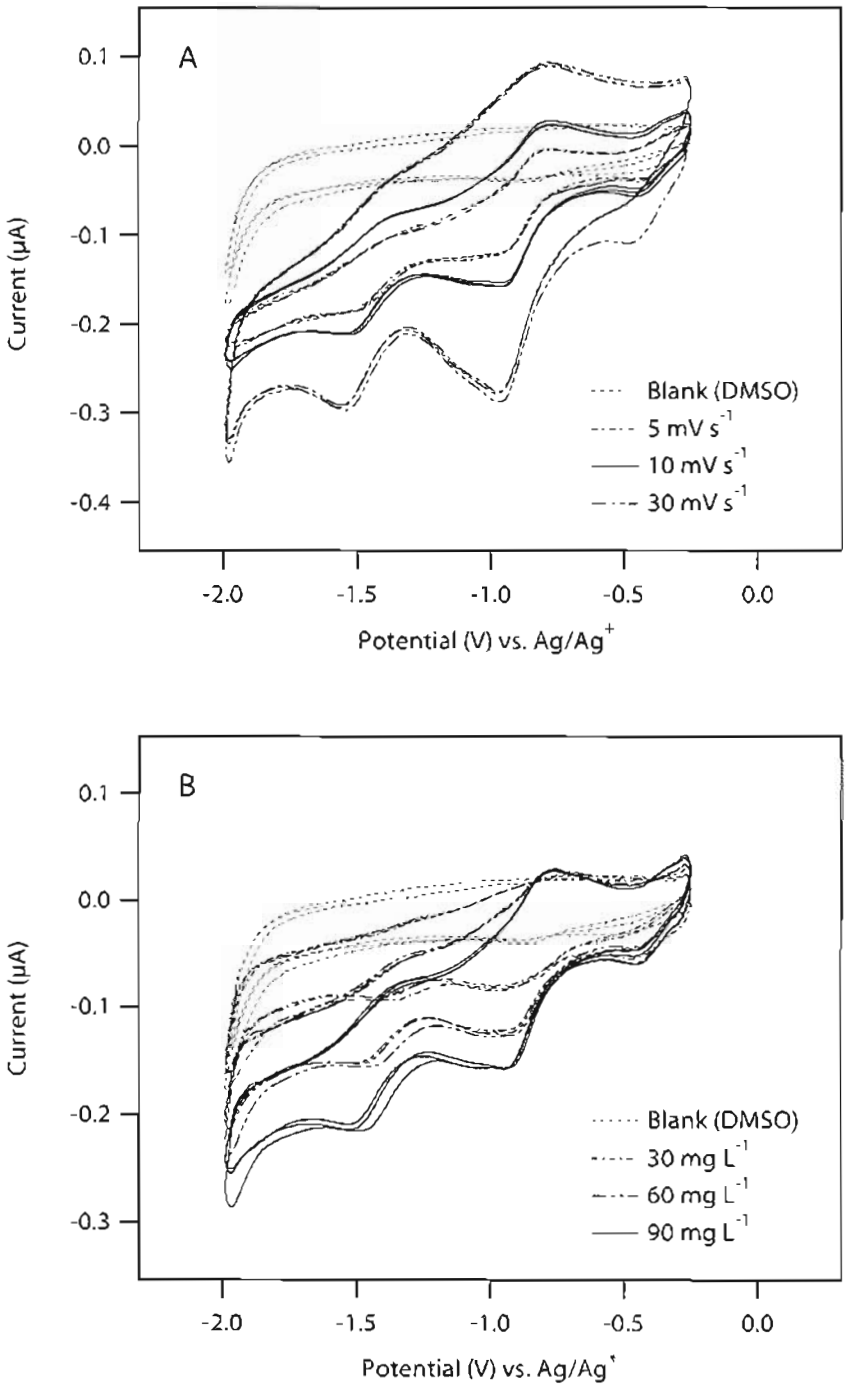

Figure 2.4. Effect of (A) scan rate and (B) concentration on CVs of NOM-PP. Working electrode: Pt disk (1.6-mm diameter). Electrolyte: 1.0 mM $NaClO_4$. Scan rate: 10 mV s^{-1}

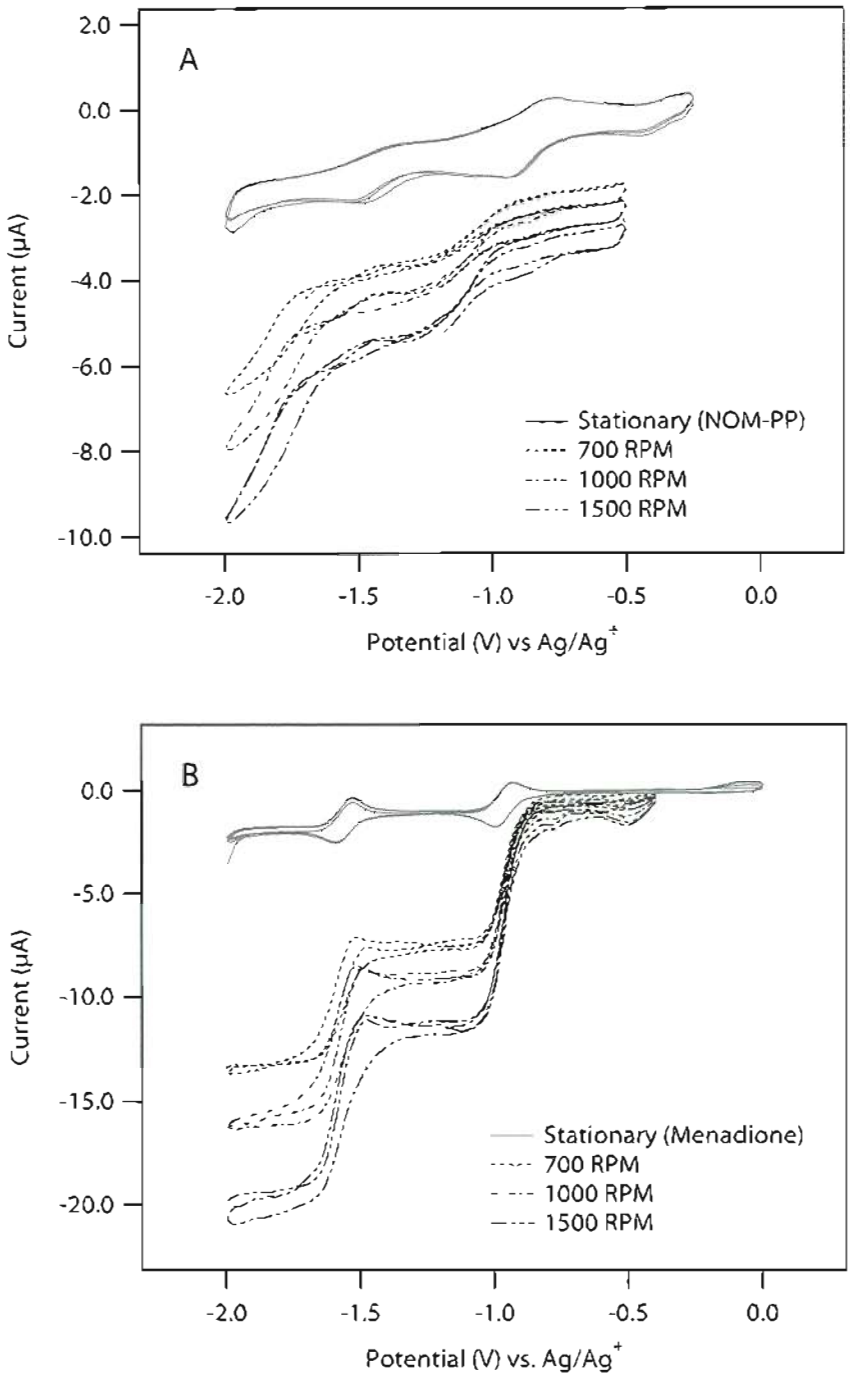

Figure 2.5. Rotating disk electrode experiment. Comparison of CVs obtained with Pt RDE: (A) NOM-PP and (B) menadione under the same conditions. Working electrode: Pt disk (1.6-mm diameter). Electrolyte: 1.0 mM $NaClO_4$. Scan rate: 10 mV s^{-1}

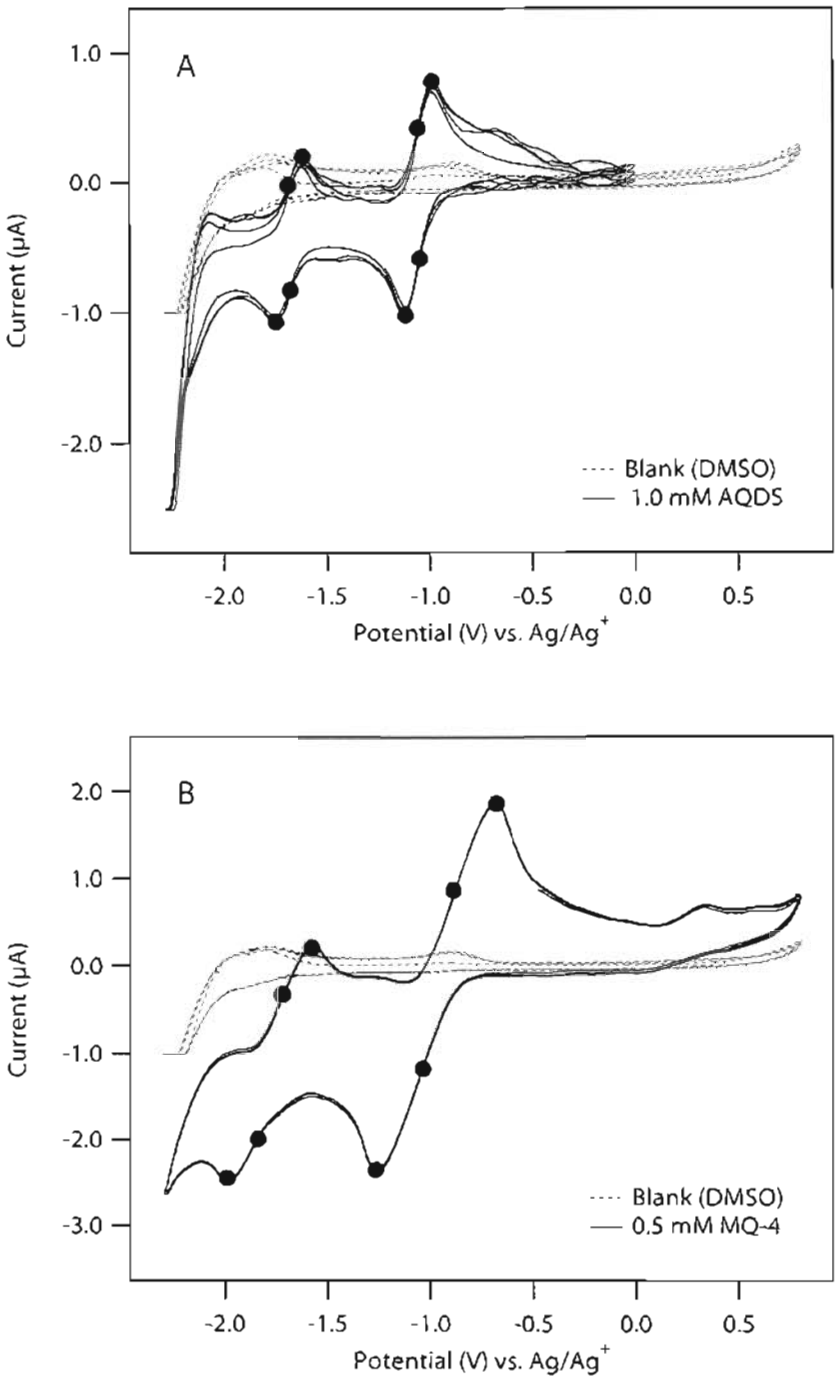

Figure 2.6. CVs of (A) AQDS and (B) menadione. Working electrode: Pt disk (1.6-mm diameter). Electrolyte: 1.0 mM $NaClO_4$. Scan rate: 10 mV s^{-1}

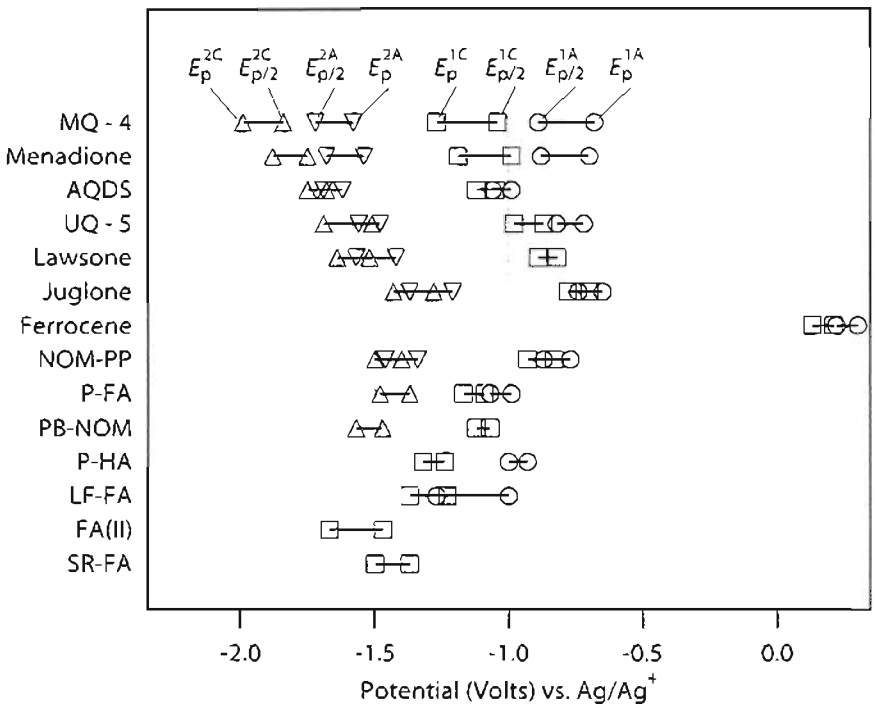

Figure 2.7. Redox ladder. Figure based on values in Table 2.1.

2.1.9. Supporting Information

Electrochemical Properties of Natural Organic Matter (NOM), Fractions of NOM, and Model Biogeochemical Electron Shuttles

James T. Nurmi and Paul G. Tratnyek

FigureS1.	Polyphenolic fraction of Georgetown NOM (NOM-PP) in H_2O with GC electrode	
Figure S2	Polyphenolic fraction of Georgetown NOM (NOM-PP) in H_2O with Pt electrode	
Figure S3	Polyphenolic fraction of Georgetown NOM (NOM-PP)	Group A
Figure S4	Peat fulvic acid (P-FA)	Group A
Figure S5	Pine Barrens NOM (PB-NOM)	Group A
Figure S6	Peat humic acid (P-HA)	Group B
Figure S7	Lake Fryxell fulvic acid (LF-FA)	Group B
Figure S8	Fulvic acid (II) (FA(II))	Group C
Figure S9	Suwannee River fulvic acid (SR-FA)	Group C
Figure S10	Georgetown NOM (NOM-GT)	Group D
Figure S11	Carbohydrate fraction of Georgetown NOM (NOM-CH)	Group D
Figure S12	Soil humic acid (S-HA)	Group D
Figure S13	San Diego humic acid (SD-HA)	Group D
Figure S14	Manuka NOM (MN-NOM)	Group D
Figure S15	Aldrich humic acid (AL-HA)	Group E
Figure S16	Anthraquinone disulfonate (AQDS)	Model Quinone
Figure S17	Juglone	Model Quinone
Figure S18	Lawsone	Model Quinone
Figure S19	Menaquinone-4 (MQ-4)	Model Quinone
Figure S20	Menadione	Model Quinone
Figure S21	Ubiquinone-5 (UQ-5)	Model Quinone
Figure S22	Ferrocene	Reference Compound
Figure S23	Correlation Plot Matrix	All NOMs

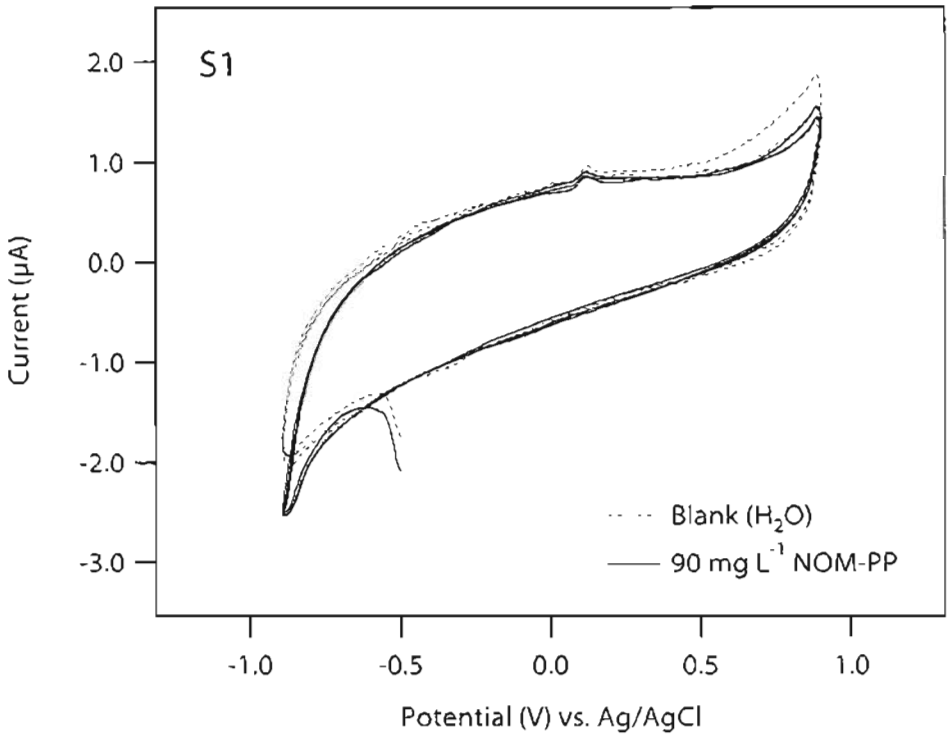
S1
2.0
1.0
0.0
-1.0
-2.0
-3.0
Current (µA)
Blank (H_2O)
90 mg L^{-1} NOM-PP
-1.0
-0.5
0.0
0.5
1.0
Potential (V) vs. Ag/AgCl

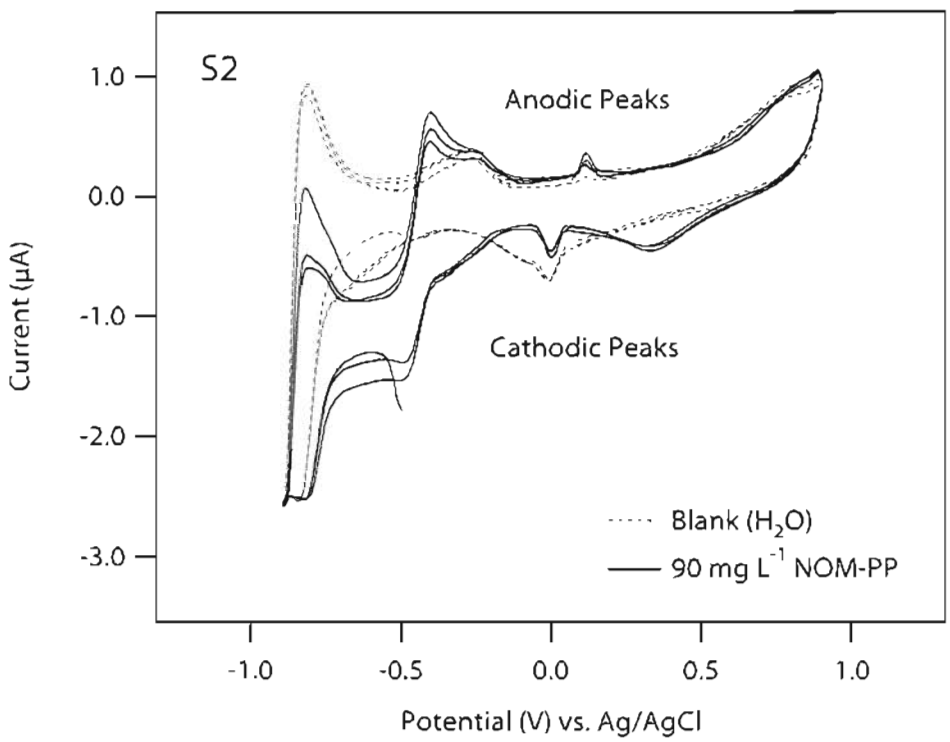
S2
Anodic Peaks
Cathodic Peaks
1.0
0.0
-1.0
-2.0
-3.0
Current (µA)
Blank (H_2O)
90 mg L^{-1} NOM-PP
-1.0
-0.5
0.0
0.5
1.0
Potential (V) vs. Ag/AgCl

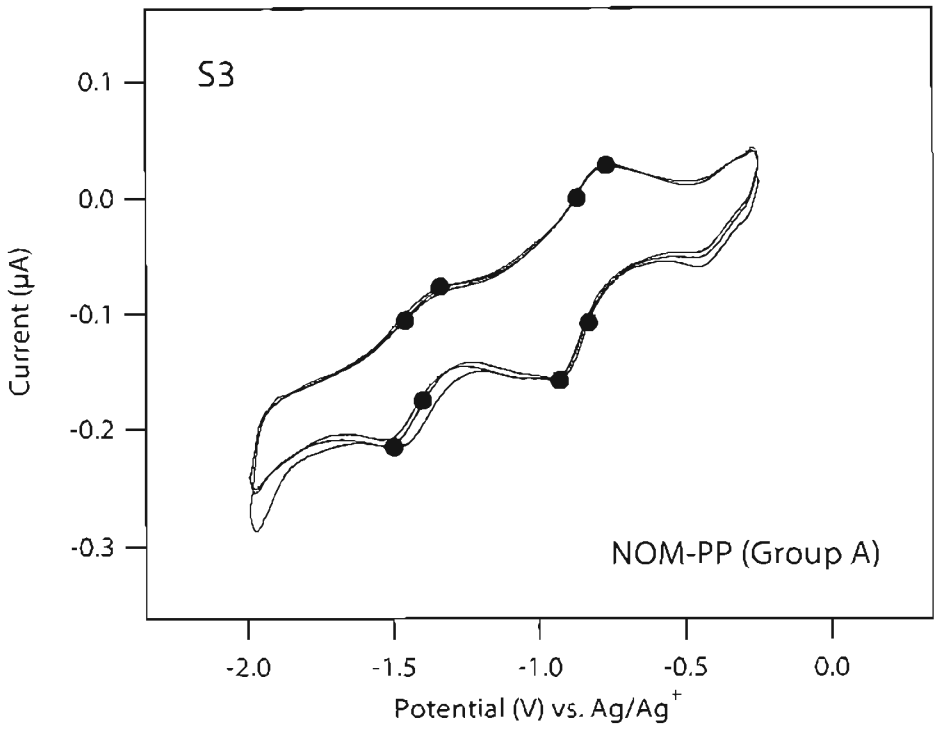
S3
0.1
0.0
-0.1
-0.2
-0.3
Current (µA)
NOM-PP (Group A)
-2.0
-1.5
-1.0
-0.5
0.0
Potential (V) vs. Ag/Ag+

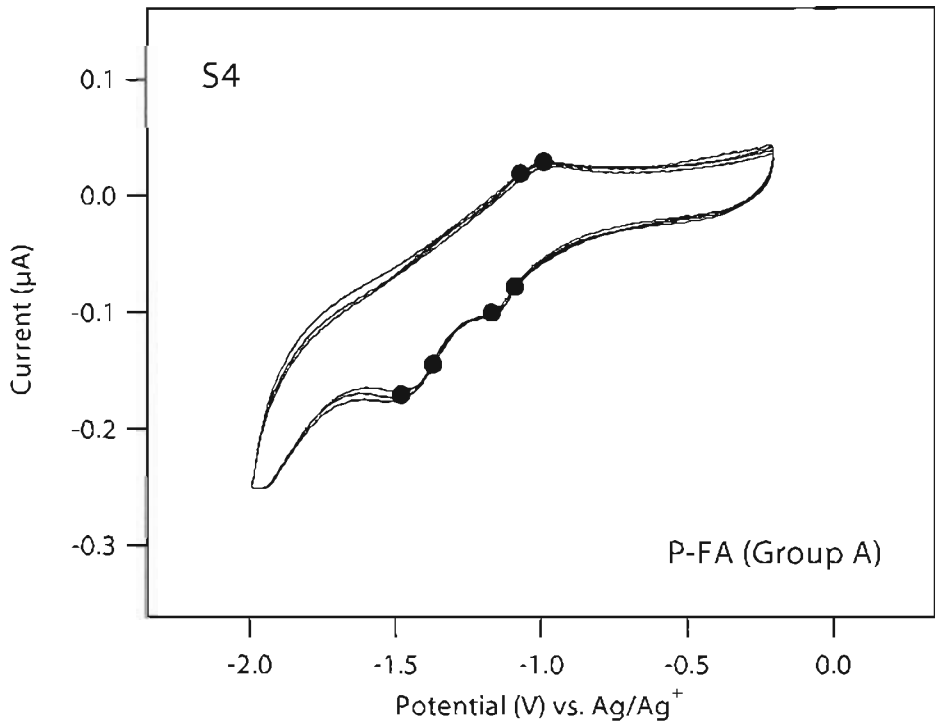
S4
0.1
0.0
-0.1
-0.2
-0.3
Current (µA)
P-FA (Group A)
-2.0
-1.5
-1.0
-0.5
0.0
Potential (V) vs. Ag/Ag+

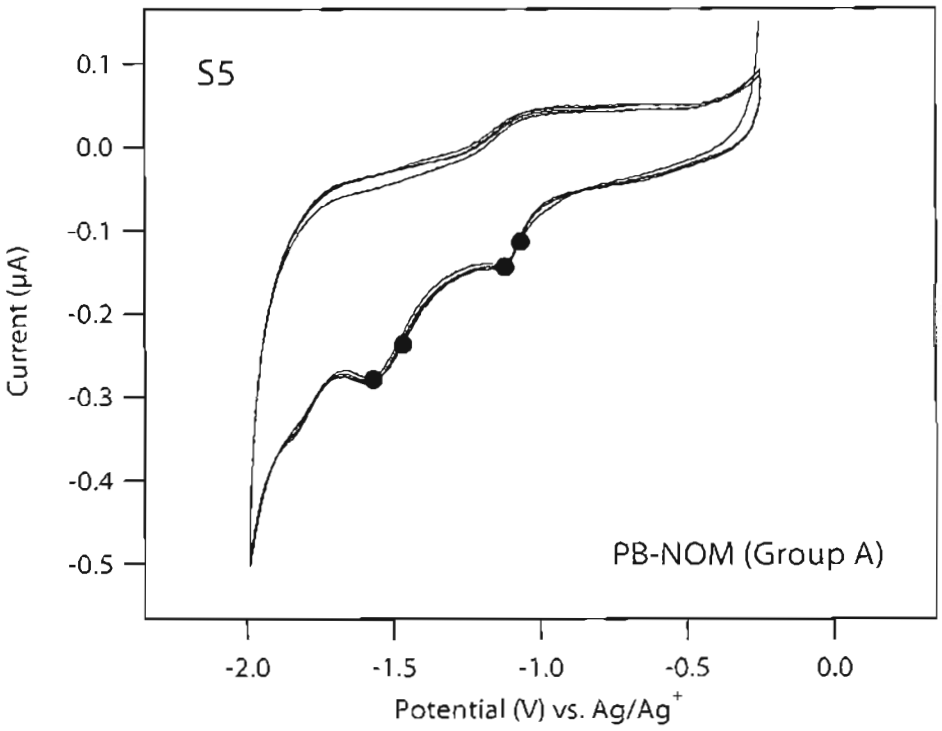
S5
PB-NOM (Group A)
Current (µA)
0.1
0.0
-0.1
-0.2
-0.3
-0.4
-0.5
-2.0
-1.5
-1.0
-0.5
0.0
Potential (V) vs. Ag/Ag+

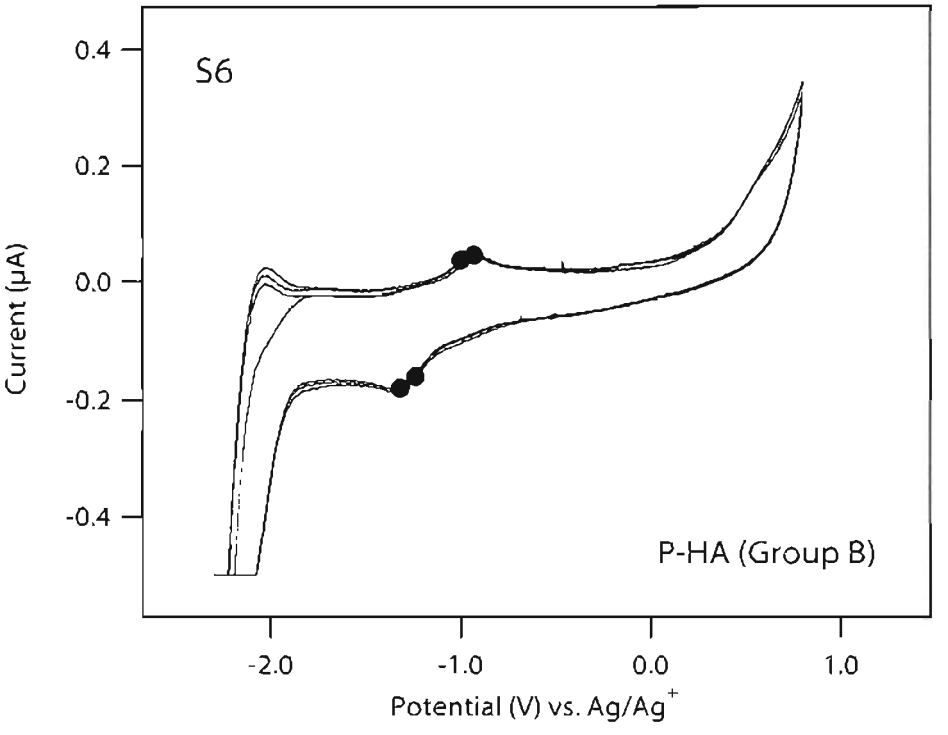
S6
P-HA (Group B)
Current (µA)
0.4
0.2
0.0
-0.2
-0.4
-2.0
-1.0
0.0
1.0
Potential (V) vs. Ag/Ag+

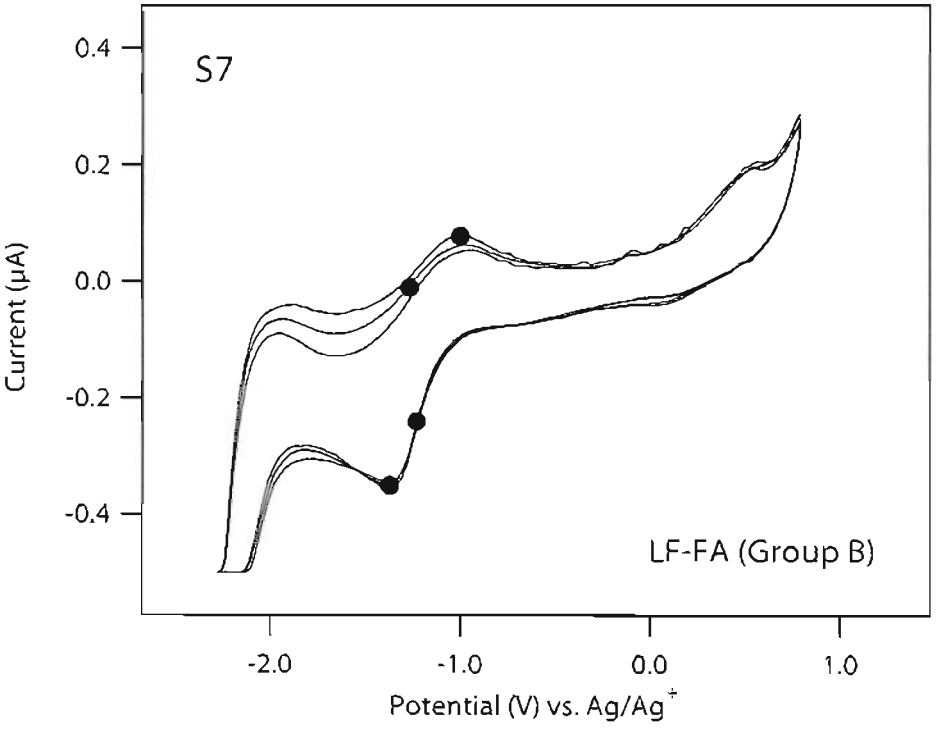
S7
LF-FA (Group B)
Current (µA)
0.4
0.2
0.0
-0.2
-0.4
-2.0
-1.0
0.0
1.0
Potential (V) vs. Ag/Ag+

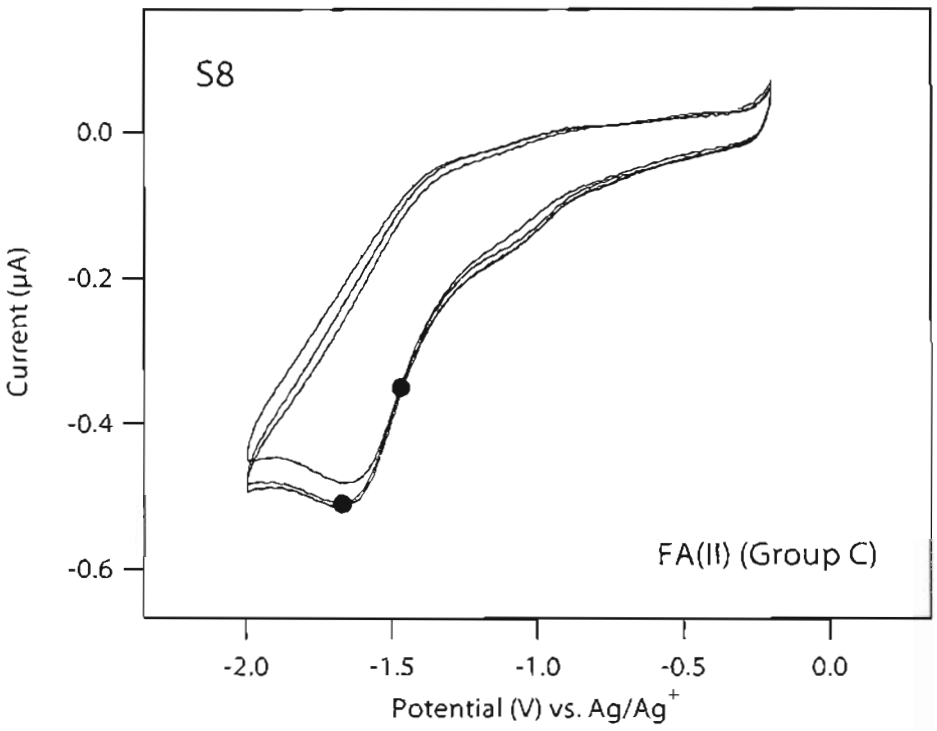
S8
0.0
-0.2
-0.4
-0.6
Current (µA)
FA(II) (Group C)
-2.0
-1.5
-1.0
-0.5
0.0
Potential (V) vs. Ag/Ag+

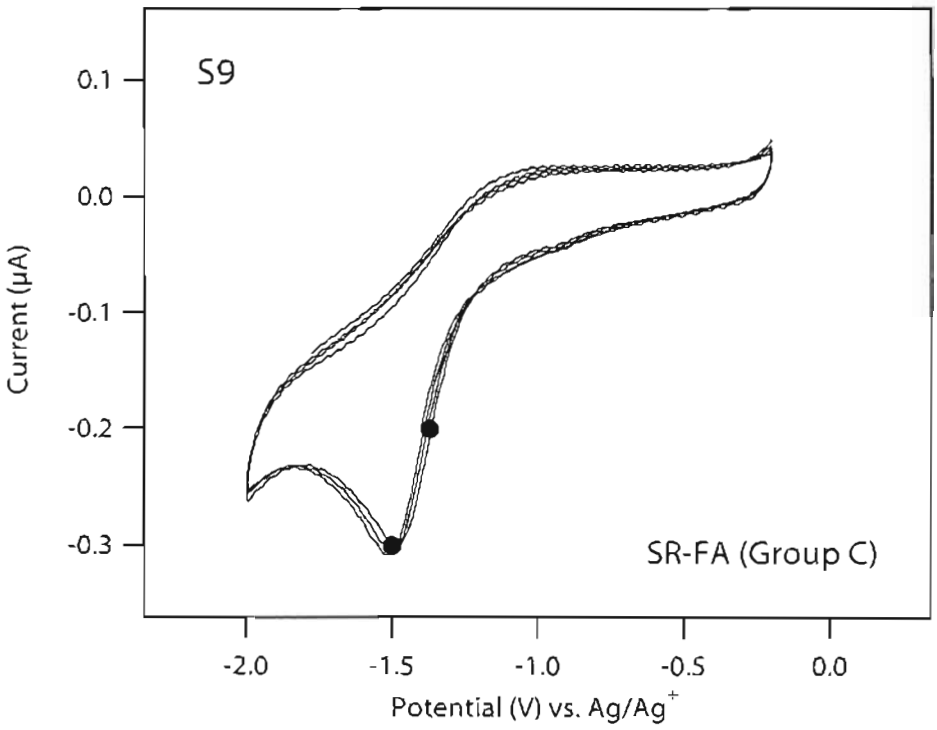
S9
0.1
0.0
-0.1
-0.2
-0.3
Current (µA)
SR-FA (Group C)
-2.0
-1.5
-1.0
-0.5
0.0
Potential (V) vs. Ag/Ag+

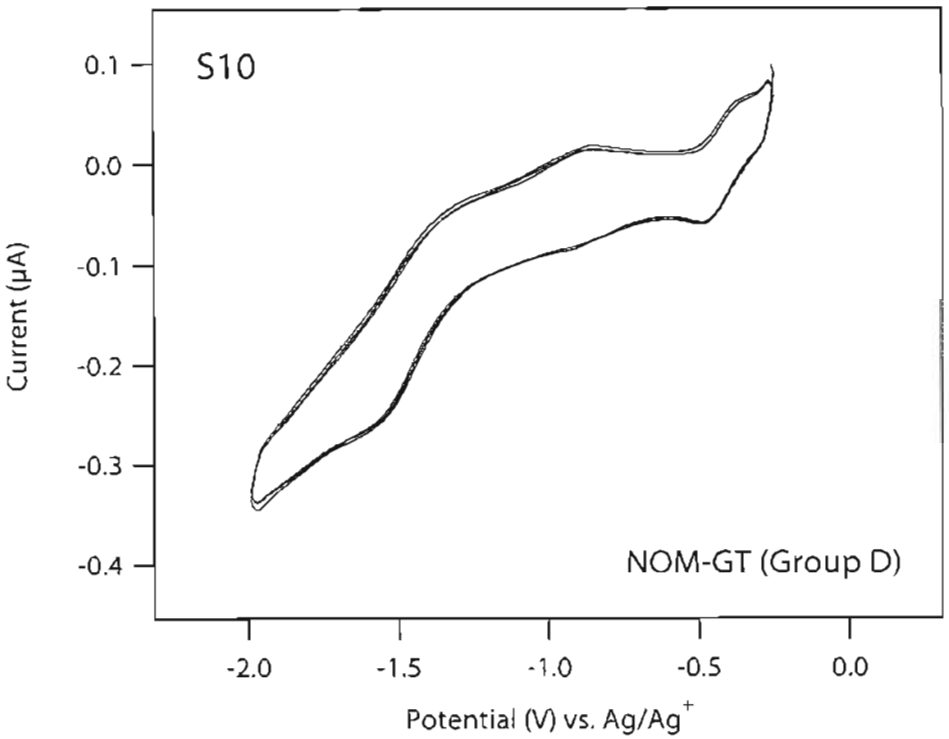
S10
NOM-GT (Group D)
Current (µA)
0.1
0.0
-0.1
-0.2
-0.3
-0.4
-2.0
-1.5
-1.0
-0.5
0.0
Potential (V) vs. Ag/Ag+

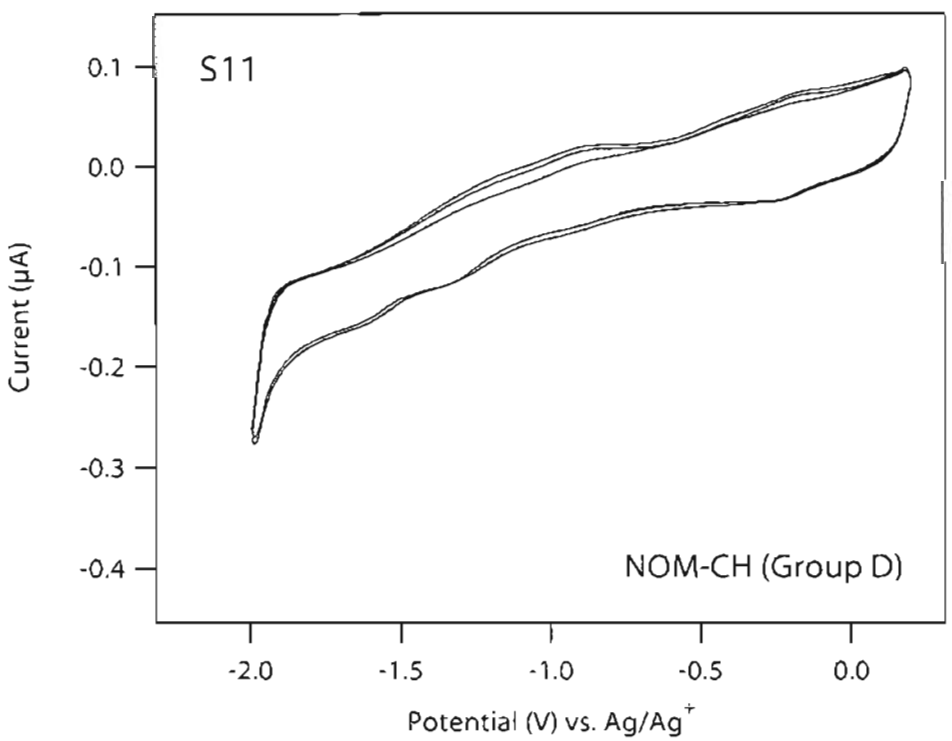
S11
NOM-CH (Group D)
Current (µA)
0.1
0.0
-0.1
-0.2
-0.3
-0.4
-2.0
-1.5
-1.0
-0.5
0.0
Potential (V) vs. Ag/Ag+

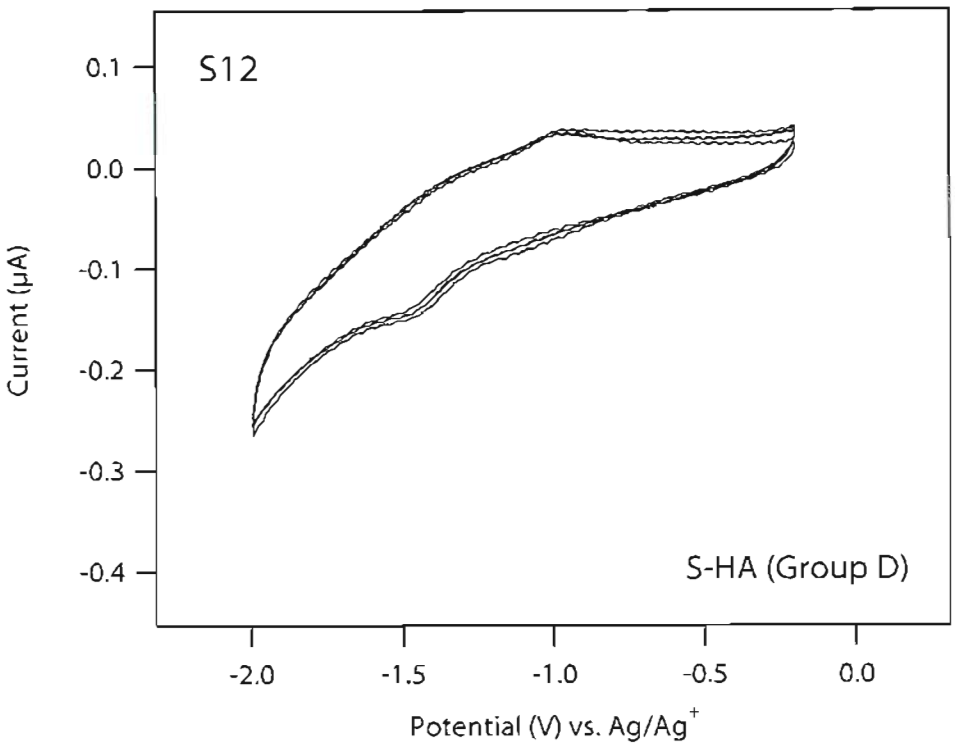
S12
S-HA (Group D)
Current (µA)
0.1
0.0
-0.1
-0.2
-0.3
-0.4
-2.0
-1.5
-1.0
-0.5
0.0
Potential (V) vs. Ag/Ag+

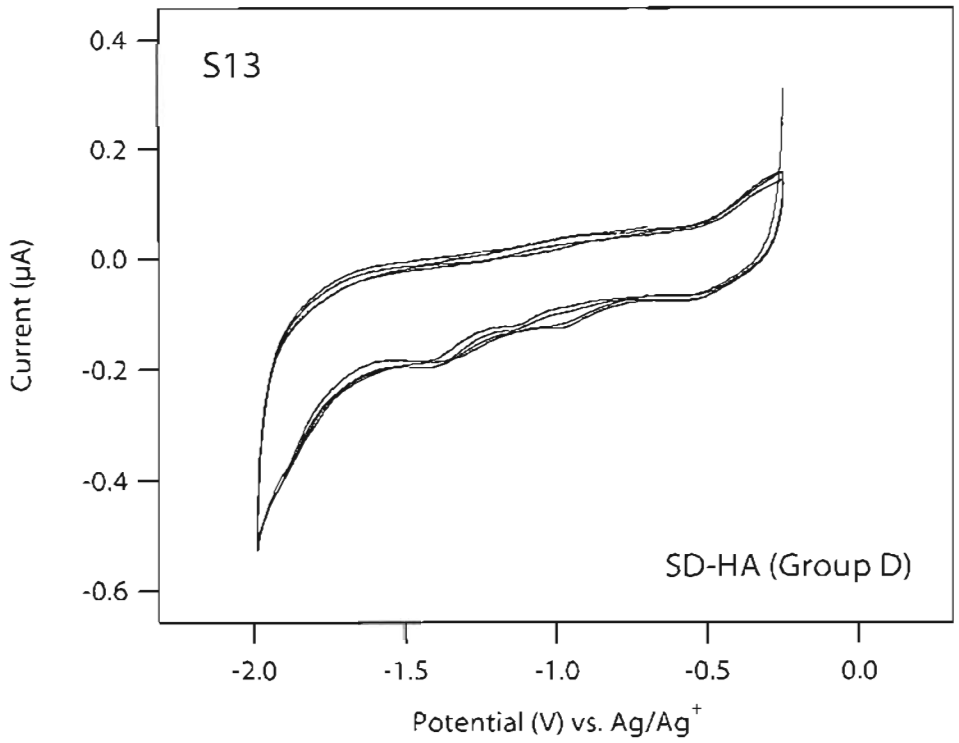
S13
SD-HA (Group D)
Current (µA)
0.4
0.2
0.0
-0.2
-0.4
-0.6
-2.0
-1.5
-1.0
-0.5
0.0
Potential (V) vs. Ag/Ag+

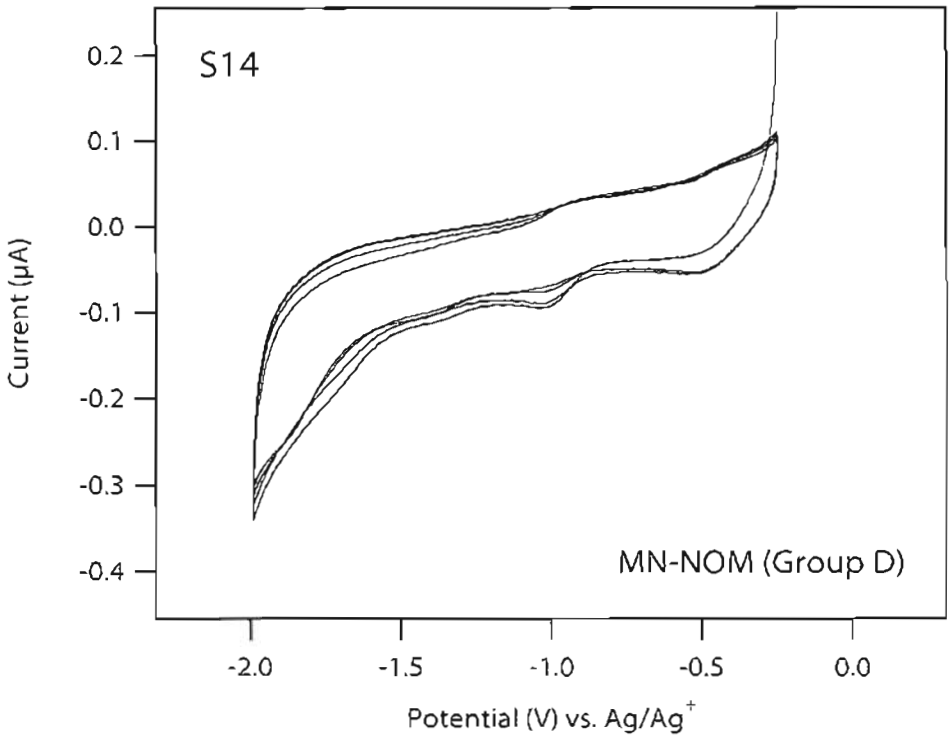
S14
MN-NOM (Group D)
Current (µA)
0.2
0.1
0.0
-0.1
-0.2
-0.3
-0.4
-2.0
-1.5
-1.0
-0.5
0.0
Potential (V) vs. Ag/Ag+

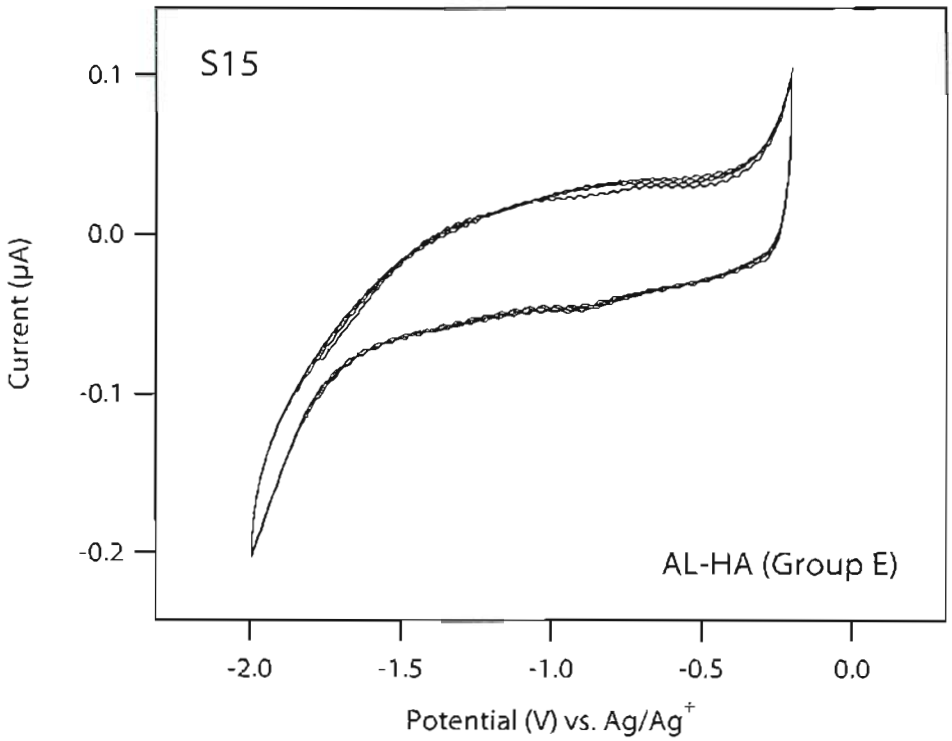
S15
AL-HA (Group E)
Current (µA)
0.1
0.0
-0.1
-0.2
-2.0
-1.5
-1.0
-0.5
0.0
Potential (V) vs. Ag/Ag+

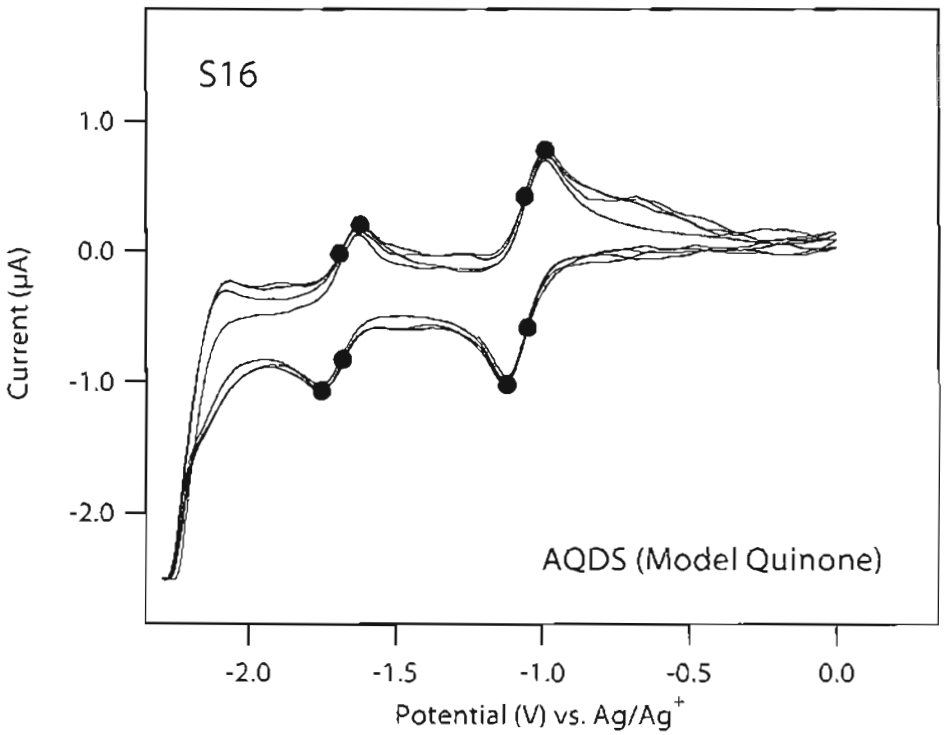
S16
1.0
0.0
-1.0
-2.0
Current (μA)
AQDS (Model Quinone)
-2.0
-1.5
-1.0
-0.5
0.0
Potential (V) vs. Ag/Ag+

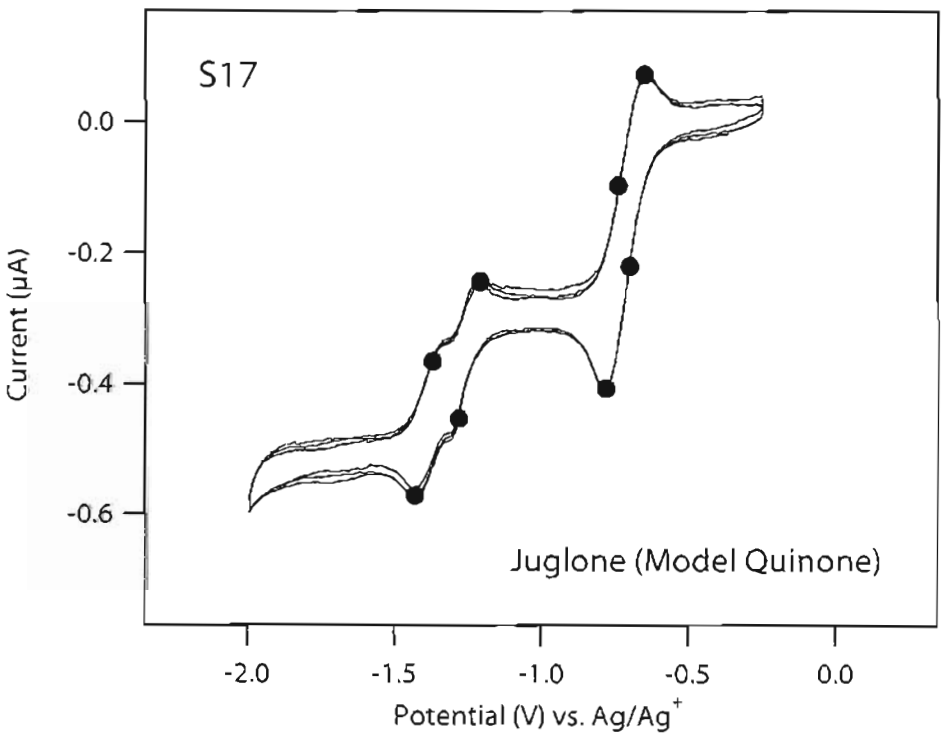
S17
0.0
-0.2
-0.4
-0.6
Current (μA)
Juglone (Model Quinone)
-2.0
-1.5
-1.0
-0.5
0.0
Potential (V) vs. Ag/Ag+

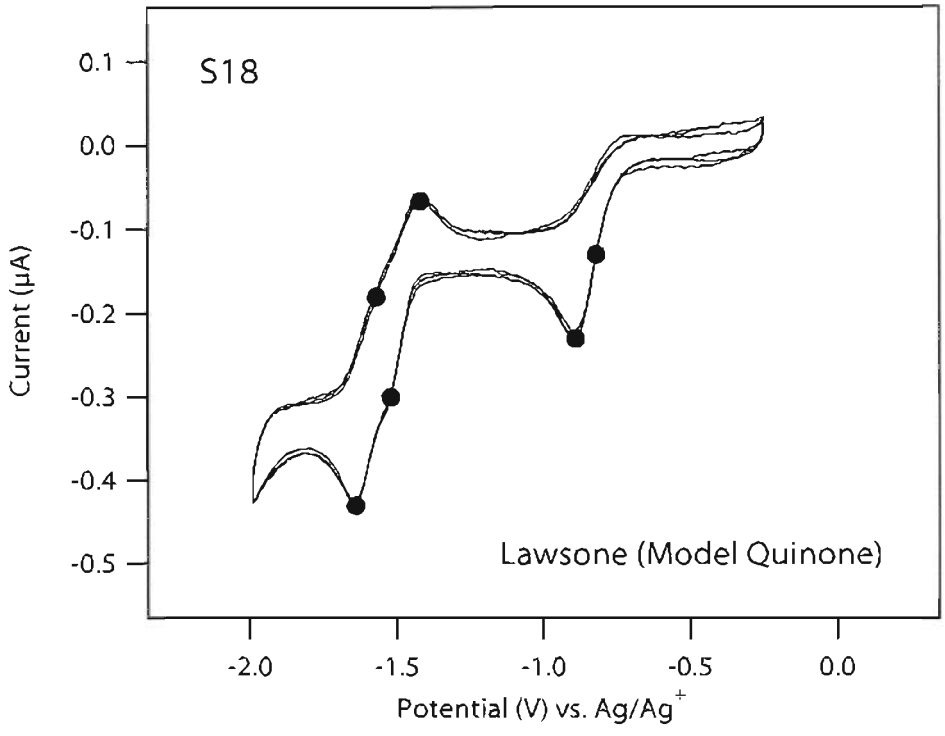
S18
0.1
0.0
-0.1
-0.2
-0.3
-0.4
-0.5
Current (µA)
Lawsone (Model Quinone)
-2.0
-1.5
-1.0
-0.5
0.0
Potential (V) vs. Ag/Ag+

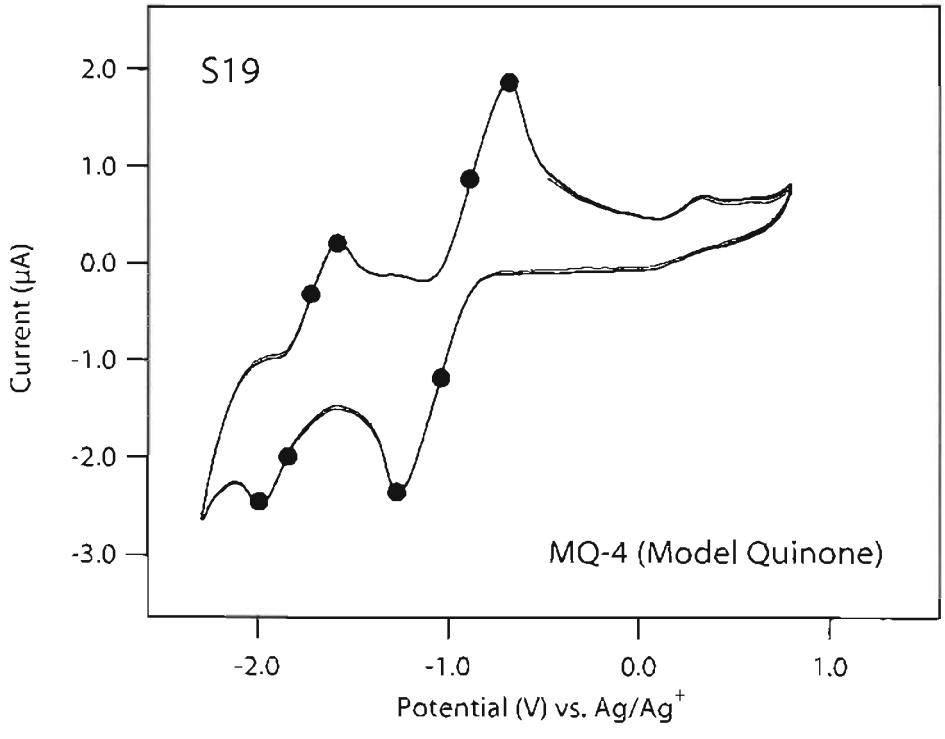
S19
2.0
1.0
0.0
-1.0
-2.0
-3.0
Current (µA)
MQ-4 (Model Quinone)
-2.0
-1.0
0.0
1.0
Potential (V) vs. Ag/Ag+

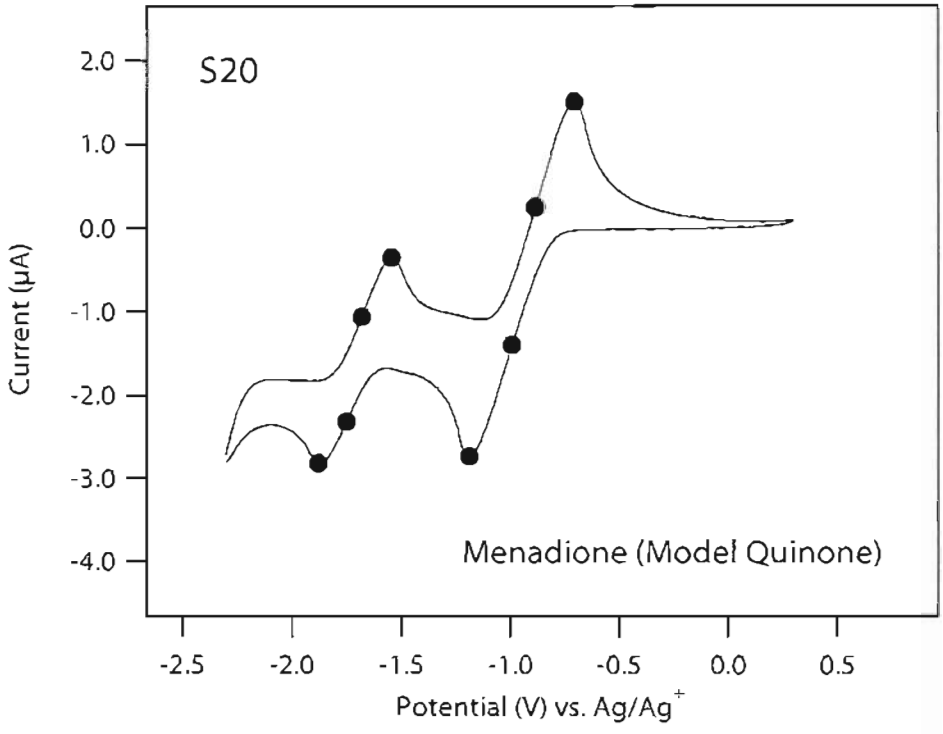
S20
Menadione (Model Quinone)
Current (µA)
2.0
1.0
0.0
-1.0
-2.0
-3.0
-4.0
-2.5
-2.0
-1.5
-1.0
-0.5
0.0
0.5
Potential (V) vs. Ag/Ag+

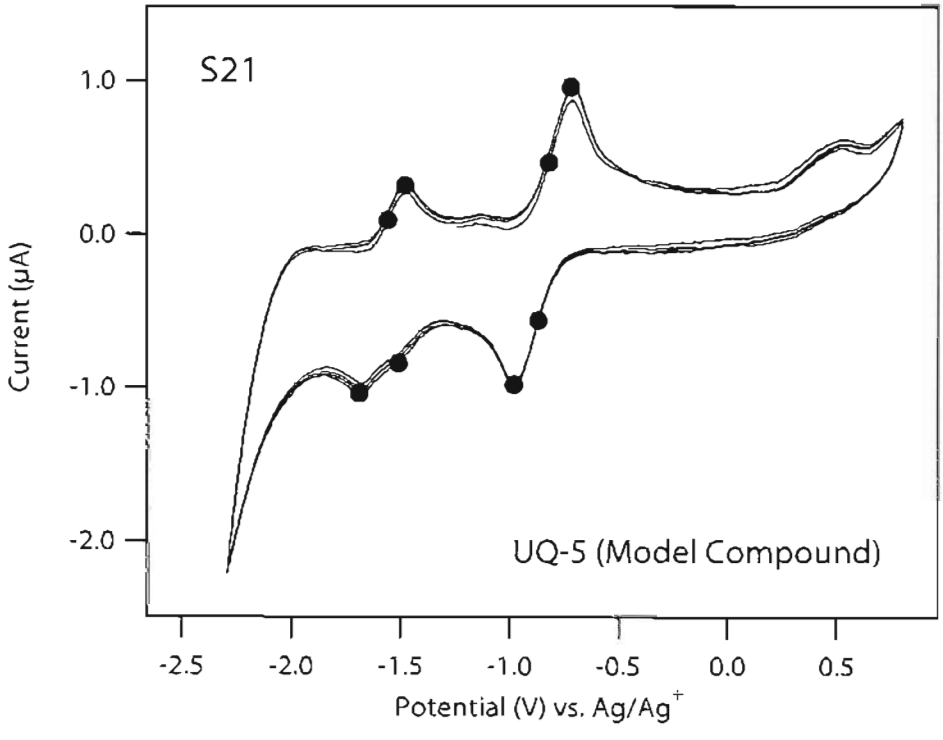
S21
UQ-5 (Model Compound)
Current (µA)
1.0
0.0
-1.0
-2.0
-2.5
-2.0
-1.5
-1.0
-0.5
0.0
0.5
Potential (V) vs. Ag/Ag+

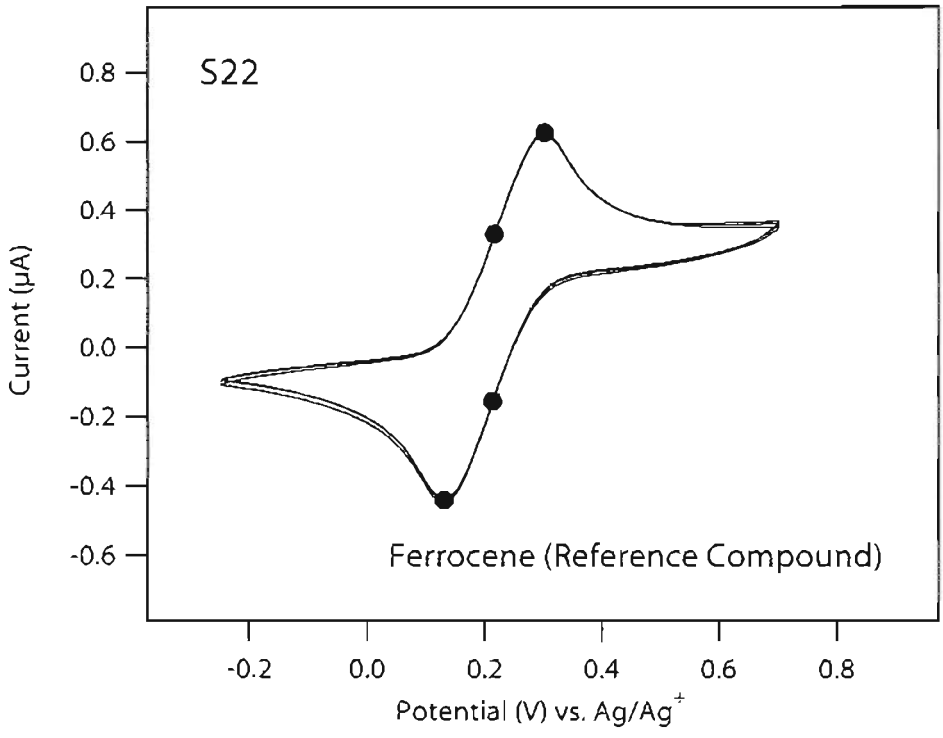
S22
0.8
0.6
0.4
0.2
0.0
-0.2
-0.4
-0.6
Current (µA)
Ferrocene (Reference Compound)
-0.2
0.0
0.2
0.4
0.6
0.8
Potential (V) vs. Ag/Ag+

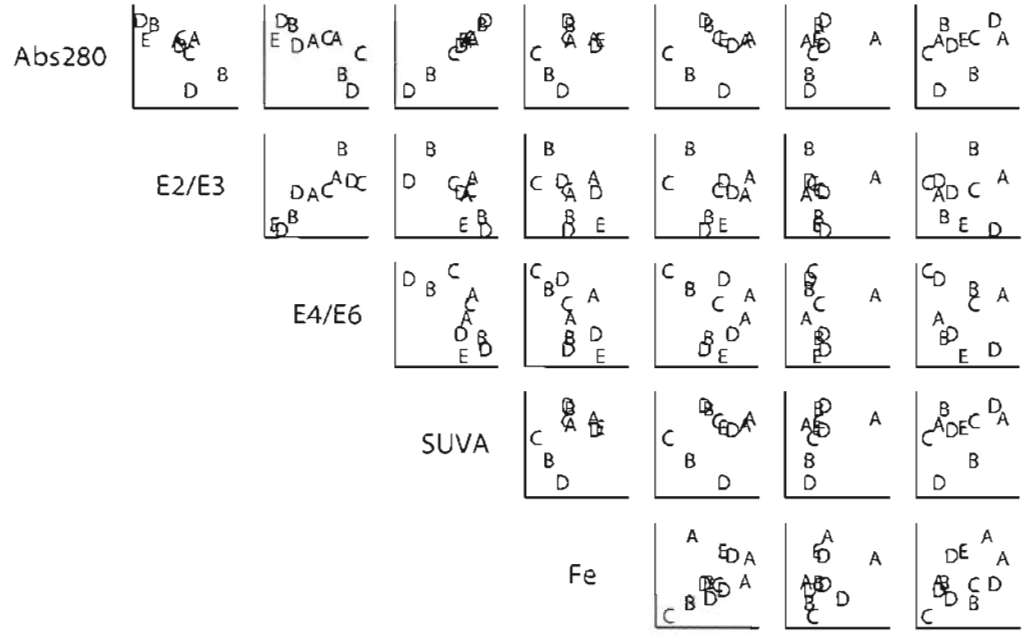

S23

Groups by CV Structure:

A	Most defined, CVs similar to quinones. (NOM-PP, P-FA, PB-NOM)
B	CVs show a single set of peaks. (P-HA, LF-FA)
C	CVs give a single cathodic peak. (FA(II), SR-FA)
D	Less defined CVs. (NOM-GT, NOM-CH, S-HA, SD-HA, MN-NOM)
E	No definition. (Aldrich HA)

2.2 Square Wave and Cyclic Voltammetry of NOM with Microelectrodes [1]

2.2.1. Abstract

In this study, we report on the further refinement of our electrochemical techniques in order to elucidate the redox properties of natural organic matter (NOM), fractions of NOM, and model biogeochemical electron shuttles. By using microelectrodes in conjunction with square wave voltammetry (SWV), we show that an un-fractionated NOM (NOM-GT) contains several redox active moieties or species. This technique also provides better resolution of peaks than previous methods. In order to relate redox potentials obtained under our experimental conditions to standard the redox potentials, a solvent independent redox active compound was used to standardize the redox potentials obtained with our method. Combining the better resolution of the SWV and the ability to relate potentials to a standard system, we show how various redox potentials obtained for NOM and NOM fractions compare to redox potentials of known electron donors and acceptors.

2.2.2. Introduction

It is well known that NOM can act as a reducing agent (reductant), and this is central to the role that NOM plays in the biogeochemical cycling of carbon [1-15]. More

[1] Adapted from Nurmi, J. T.; Tratnyek, P. G. In Extended Abstract in *Proceedings of the 20th Anniversary Conference of the International Humic Substances Society (IHSS), 21-26 July 2002, Northeastern University, Boston, MA*, 2002; pp 58-60.

recently, there has been growing interest in the role that NOM plays as an electron shuttle (mediator) in biogeochemical cycles. For example, several recent studies have shown that the addition of NOM to cultures of iron reducing bacteria can increase the rate of dissimilatory iron reduction [16]. These effects have been attributed to polyphenolic (especially hydroquinonoid) moieties that comprise a portion of NOM [17]. There are, however, other moieties that may contribute to the overall redox activity of NOM (e.g., complexed metals [14]), and this complexity has been one of the main impediments to the development of chemically exact descriptions of redox processes involving NOM.

Natural organic matter (NOM) has been studied for several decades, yet the physico-chemical properties are still being elucidated. Many studies have given conflicting results on the reducing power of NOM or NOM fractions and have attempted to assign formal redox potentials to NOM and NOM fractions [14, 15, 18]. One of the difficulties with attributing useful formal redox potentials to NOM is the limitations of the methods used. The majority of redox studies involving NOM or NOM fractions use indirect techniques such as adding NOM to a suite of redox labile probe compounds and measuring whether or not the probe compound is reduced by the NOM sample. This indirect technique allows for the determination of approximate formal redox potentials but does not address several important issues. Many studies also have used titrimetric analyses with moderate success [15, 18-22]

Recently, we successfully demonstrated that the use of linear sweep voltammetry in conjunction with the use of DMSO as a solvent and a slow scan rate provided moderately well defined peaks which correlate to redox potentials for several NOM fractions [23]. Although resolving these peaks was a breakthrough, we were still left with the issue of how to relate redox potentials determined in DMSO to standard redox potentials in water at environmentally relevant pH's. In this study, we report on the refinement of electrochemical techniques by using square wave voltammetry coupled with a microelectrode. This refinement allows for even better resolution of peaks for various NOM fractions. We also show that with the use of a solvent independent redox

active species, we can normalize redox potentials between solvents. We found that the unfractionated Georgetown NOM gave multiple peaks indicative of multiple redox active compounds or moieties. We propose that instead of a attributing a single formal redox potential to NOM and NOM fractions, there exists a redox continuum within NOM that is comprised of various redox active compounds and moieties.

2.2.3. Materials and Methods

Table 2.3 summarizes the materials and conditions used in this and previously published attempts to use voltammetric methods to characterize the redox properties of NOM. The main characteristics of our current method include Pt working and counter electrodes, dimethyl sulfoxide (DMSO) as the solvent, 1.0 mM NaClO4 as the electrolyte, and a Ag/Ag^+ reference electrode. In this study, we compare the response obtained with a platinum disc working electrode (1.6 mm dia.) and a platinum microelectrode (125 μm dia.) prepared by a procedure adapted from [24].

The NOM, and fractions of NOM, we have used in this work were obtained from B. Gu (Oak Ridge National Laboratory). He obtained the raw concentrate (NOM-GT) by reverse osmosis using brown water from a wetland pond in Georgetown, SC. A fraction of NOM-GT that is enriched in polyphenolic material (NOM-PP) was obtained by elution on a column of cross-linked polyvinyl pyrrolidone polymer. NOM-PP and other fractions of NOM-GT have been characterized by UV/Vis, IR, NMR, and EPR spectroscopy [25]. For our work, stock solutions of NOM were prepared by dissolving the freeze-dried materials directly into DMSO.

Cyclic voltammetry (CV) was performed with the Pt microelectrode by starting at −1.8 V vs. Ag/Ag^+ for most of the NOM and model compounds. Sqware wave voltammetry (SWV) was also initiated at this potential and ramped toward more positive potentials.

2.2.4. Results and Discussion

It appears that by using an aprotic solvent, DMSO, direct electrochemistry of NOM and NOM fractions have yielded results that allow for the determination of redox properties, such as redox potentials. In a previous study [23], we reported that several NOM fractions, especially a polyphenolic fraction (NOM-PP) gave well defined peaks. These peaks were then correlated with NOM model compounds and metal content. The NOM-PP fraction gave voltammograms similar to various quinones and gave peaks at potentials between those of juglone and lawsone. In Figure 2.8, three voltammograms are shown for the quinone, menadione. Figure 2.8A was obtained using the technique used in [23]. Figure 2.8B was obtained using CV with a Pt microelectrode. Figure 2.8C was obtained using a Pt microelectrode in conjunction with square wave voltammetry. Peak resolution increases when a microelectrode is used (Fig. 2.8B) and increases even more when SWV is employed (Fig. 2.8C). Figure 2.8B gives current plateaus instead of peaks due to the use of the microelectrode. As the working electrode surface area decreases, the limitations due to mass transfer to and from the electrode surface become minimized and thus the current response resembles that which is obtained by using rotating disk electrodes [26]. This allows for a more precise and accurate measurement of the potential at which each peak occurs. With CV, Figure 2.8A and C, half-wave potentials can be used to approximate standard redox potentials assuming that the system is electrochemically reversible. With SWV, the peak potential is used to approximate the formal redox potential.

Figure 2.9 shows the results of the three techniques used on an un-fractionated NOM sample from Georgetown NOM (NOM-GT). When the microelectrode was used (Fig. 2.9B), more peaks could be observed compared to Figure 2.9A. When SWV was used (Fig. 2.9C), the resolution of peaks was further improved. The cathodic and anodic peaks are indicated by solid circles. Notice that there are several well resolved peaks compared to Figure 2.9A and B. This indicates that there are several redox labile compounds or moieties in NOM-GT.

When the polyphenolic fraction (NOM-PP) of NOM-GT was studied, we obtained voltammograms as shown in Figure 2.10. As reported in [23] (Figure 2.10A), two sets of peaks were obtained. When the microelectrode was used (Figure 2.10B), the current response was similar to that observed with the quinone model compound. Current plateaus were observed where the peaks from Figure 2.10A occurred indicating that the response is due to two single electron transfers. When SWV was used, two sets of well resolved peaks were observed as indicated in Figure 2.10C with solid circles. This appears to be further evidence that the NOM-PP fraction contains an electrochemically reversible compound or moiety that can donate and accept two electrons (one electron for each set of peaks).

Figure 2.11 shows the data obtained for a range of NOM sources and NOM fractions. The groups (A-F) represent the groupings determined by shape of the voltammograms reported in [23]. The rows represent the three techniques used in this study. As you move from top to bottom, the resolution of the voltammograms increase in all cases except for the Aldrich humic acid, for which not peaks were observed. The open circles represent peak potentials and half-wave potentials obtained by using CV. The solid circles are used to mark peak potentials for the SWV. In Figure 2.12, all peak and half-wave potentials are summarized for all of the NOM samples and NOM model compounds studied. The open markers were obtained from CV and the solid markers are those obtained from SWV. Note that that there are no open markers for the NOM-GT samples but several solid markers indicating that SWV was better able to resolve various peaks indicative of several redox active compounds and/or moieties.

One of the major impediments in the use of these electrochemical techniques to determine redox potentials of NOM and NOM fractions is that all of the potentials are related to a Ag/Ag^{+} reference electrode in DMSO. In order to interpret the redox potentials obtained in this study to standard redox potentials under aqueous conditions at a pH = 7.0, we needed to correlate potentials obtained in DMSO to potentials in water. Since the activity coefficient of large polymers such as NOM are likely to differ between solvents and it is unclear what effect DMSO has on the secondary, tertiary and possible

even quaternary structure of NOM, a compound that is solvent independent was needed. We chose the ferricinium/ferricenium ion (Fc/Fc^+) for this purpose. By determining the redox potential of the Fc/Fc^+ couple in DMSO vs. Ag/Ag^+ and also in water vs. Ag/AgCl, we were able to normalize the potentials obtained in DMSO to potentials in water at environmental conditions (Fig. 2.13) [27]. By normalizing the potentials of several of the NOM samples and tabulating environmentally relevant redox potentials for electron donors and acceptors, we created a redox ladder that consists of three columns (Figure 2.14). The first column represents possible electron donors, the middle column is for electron transfer mediators, and the third column consists of redox potentials for various contaminants. Note that the redox potential for the NOM-PP fraction lies between juglone and menadione. The gray bar ranges from approximately -0.35 to +0.45 vs. SHE and represents the entire range of redox potentials found for the unfractionated NOM-GT sample.

2.2.5. Acknowledgements

This research was sponsored by the Natural and Accelerated Bioremediation Research (NABIR) Program, Office of Biological and Environmental Research, U.S. Department of Energy, under contract DE-AC05-00OR22725 with the Oak Ridge National Laboratory.

2.2.6. References

[1] Thurman, E. M. *Organic Geochemistry of Natural Waters*; Nijhoff/Junk: Dordrecht, 1986.

[2] Aiken, G. R.; McKnight, D. M.; Wershaw, R. L.; MacCarthy, P. In *Humic Substances in Soil, Sediment, and Water*; Wiley-Interscience, 1985.

[3] Buffle, J.; Deladoey, P.; Zumstein, J.; Haerdi, W. Analysis and characterization of natural organic matters in freshwaters. I. Study of analytical techniques *Schweiz. Z. Hydrol.* **1982**, *44*, 327-362.

[4] Choudhry, G. G. Humic substances: interactions with environmental chemicals (excluding sorptive interactions) *Toxic. Environ. Chem.* **1983**, *6*, 231-257.

[5] Frimmel, F. H. Characterization of natural organic matter as major constituents in aquatic systems *J. Contam. Hydrol.* **1998**, *35*, 201-216.

[6] Leenheer, J. A.; Mcknight, D. M.; Thurman, E. M.; MacCarthy, P. In *Humic Substances in the Suwannee River, Georgia; Interactions, Properties, and Proposed Structures, Water Supply Paper No. 2373*; Averett, R. C., Leenheer, J. A., McKnight, D. M., Thorn, K. A., Eds.; U.S. Geological Survey, 1994; pp 195-211.

[7] Lovley, D. R.; Blunt-Harris, E. L. Role of humic-bound iron as an electron transfer agent in dissimilatory Fe(III) reduction *Appl. Environ. Microbiol.* **1999**, *65*, 4252-4254.

[8] Lovley, D. R.; Coates, J. D.; BluntHarris, E. L.; Phillips, E. J. P.; Woodward, J. C. Humic substances as electron acceptors for microbial respiration *Nature* **1996**, *382*, 445-448.

[9] Macalady, D. L.; Ranville, J. F. In *Perspectives in Environmental Chemistry*; Macalady, D. L., Ed.; Oxford: New York, 1998; pp 94-137.

[10] Schindler, J. E.; Williams, D. J.; Zimmerman, A. P. In *Environmental Biogeochemistry.*; Nriagu, J. O., Ed.; Ann Arbor Science: Ann Arbor, 1976; Vol. 1. Carbon, Nitrogen, Phosphorus, Sulfur, and Selenium Cycles, pp 109-115.

[11] Schnitzer, M.; Riffaldi, R. The Determination of Quinone Groups in Humic Substances *Soil. Sci. Soc. Amer. Proc.* **1972**, *36*, 772-777.

[12] Steelink, C. Investigating humic acids in soils *Anal. Chem.* **2002**, *74*, 326A-333A.

[13] Stevenson, F. J. *Humus Chemistry: Genesis, Composition, Reactions*; Wiley Interscience: New York, 1982.

[14] Struyk, Z.; Sposito, G. Redox properties of standard humic acids *Geoderma* **2001**, *102*, 329-346.

[15] Szilágyi, M. The redox properties and the determination of the normal potential of the peat-water system *Soil Sci.* **1973**, *115*, 434-437.

[16] Lovley, D. R.; Fraga, J. L.; Blunt-Harris, E. L.; Hayes, L. A.; Phillips, E. J. P.; Coates, J. D. Humic substances as a mediator for microbially catalyzed metal reduction *Acta Hydrochim. Hydrobiol.* **1998**, *26*, 152-157.

[17] Scott, D. T.; McKnight, D. M.; Blunt-Harris, E. L.; Kolesar, S. E.; Lovley, D. R. Quinone moieties act as electron acceptors in the reduction of humic substances by humics-reducing microorganisms *Environ. Sci. Technol.* **1998**, *32*, 2984-2989.

[18] Szilágyi, M. Reduction of Fe^{3+} ion by humic acid preparations *Soil Sci.* **1971**, *111*, 233-235.

[19] Zimmerman, A. P. Electron intensity, the role of humic acids in extracellular electron transport and chemical determination of pE in natural waters *Hydrobiologia* **1981**, *78*, 259-265.

[20] Visser, S. A. Oxidation-reduction potentials and capillary activities of humic acids *Nature* **1964**, *4958*, 581.

[21] Helburn, R. S.; MacCarthy, P. Determination of some redox properties of humic acid by alkaline ferricyanide titration *Anal. Chim. Acta* **1994**, *295*, 263-272.

[22] Matthiessen, A. Kinetic aspects of the reduction of mercury ions by humic substances.1. Experimental design *Fres. J. Anal. Chem.* **1996**, *354*, 747- 749.

[23] Nurmi, J. T.; Tratnyek, P. G. Electrochemical properties of natural organic matter (NOM), fractions of NOM, and model biogeochemical electron shuttles *Environ. Sci. Technol.* **2002**, *36*, 617-624.

[24] Brendel, P. J.; Luther, G. W., III Development of a gold amalgam voltammetric microelectrode for the determination of dissolved Fe, Mn, O_2, and S(-II) in porewaters of marine and freshwater sediments *Environ. Sci. Technol.* **1995**, *29*, 751-761.

[25] Chen, J.; LeBoeuf, E. J.; Choi, S.; Gu, B. Spectroscopic characterization of structural and functional properties of natural organic matter fractions *Chemosphere* **2002**, *48*, 59-68.

[26] Sawyer, D. T.; Sobkowiak, A.; Roberts, J. L. J. *Electrochemistry for Chemists*; 2nd ed.; Wiley: New York, 1995.

[27] Treimer, S. E.; Evans, D. H. Electrochemical reduction of acids in dimethyl sulfoxide. CE mechanisms and beyond *J. Electroanal. Chem.* **1998**, *449*, 39.

Table 2.3. Electrochemical parameters used in voltammetric studies of NOM.

Properties	Helburn, 1994	Motheo, 2000	Nurmi, 2002	Nurmi (IHSS, 2002 and unpublished)
Working electrode	Au Wire	$Ti/Ir_nTi_nO_2$	Pt disk	Pt microelectrode
Counter electrode	Au Wire	Steel	Pt wire	Pt wire
Reference electrode	SCE	SCE	Ag/Ag^+	Ag/Ag^+
Potential Wave Form	LSV	LSV	LSV	LSV and SWV
Scan Rate	500 mV/s	50 mV/s	10 mV/s	1.0-100 mV/s
Solvent	H_2O	H_2O	DMSO	DMSO
Electrolyte	0.5 M KCl	0.1 M KCl	1.0 mM $NaClO_4$	1.0 mM $NaClO_4$
NOM conc.	3 g/L	30 mg/L	90 mg/L	90 mg/L
NOM type	Glenamoy, Ireland HA	Mogi Guacu River peat HA	Various NOM	Various NOM

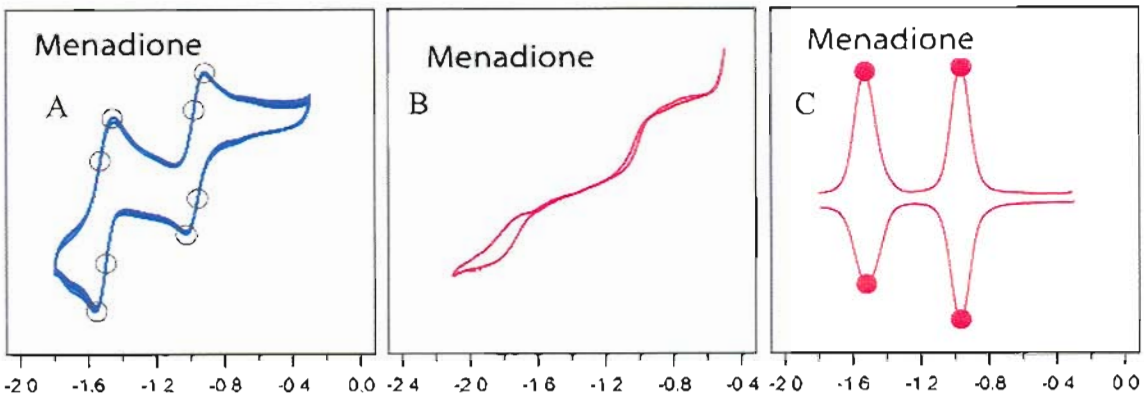

Figure 2.8. Voltammetry of the model compound, menadione. LSV with a (A) macroelectrode, (B) microelectrode. (C) SWV with a microelectrode.

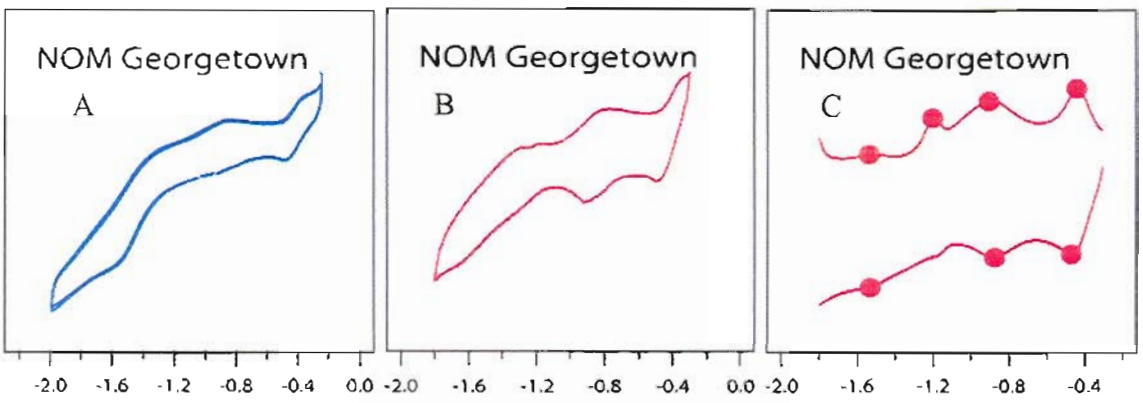

Figure 2.9. Voltammetry of NOM-GT. LSV with a (A) macroelectrode, (B) microelectrode. (C) SWV with a microelectrode.

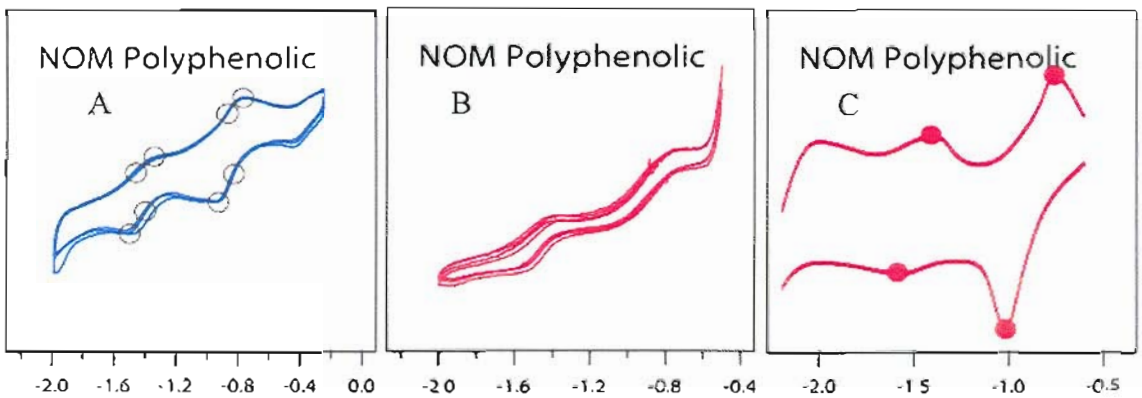

Figure 2.10. Voltammetry of NOM-PP. LSV with a (A) macroelectrode, (B) microelectrode. (C) SWV with a microelectrode.

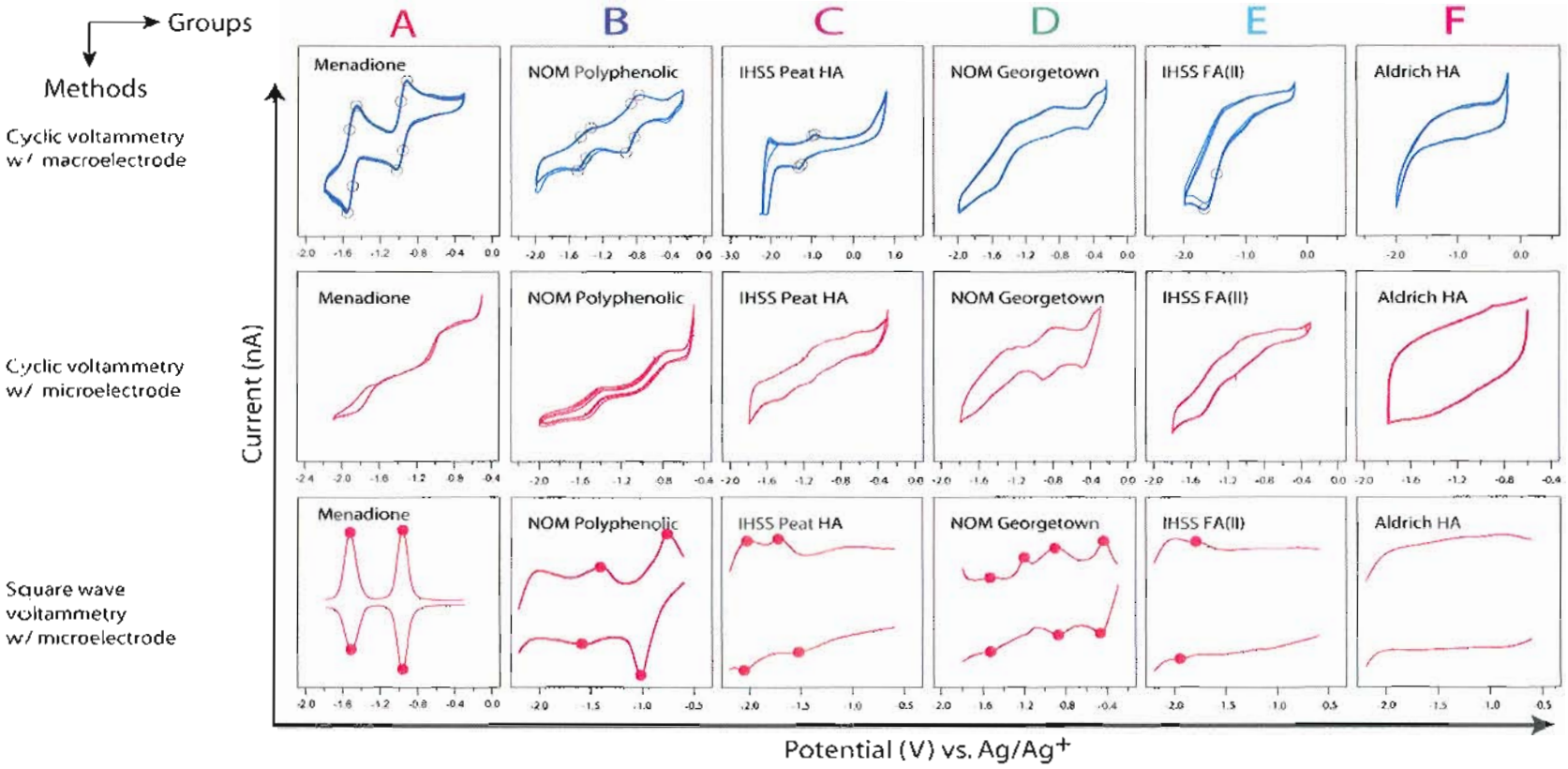

Figure 2.11. All NOM and NOM fractions with all electrochemical techniques.

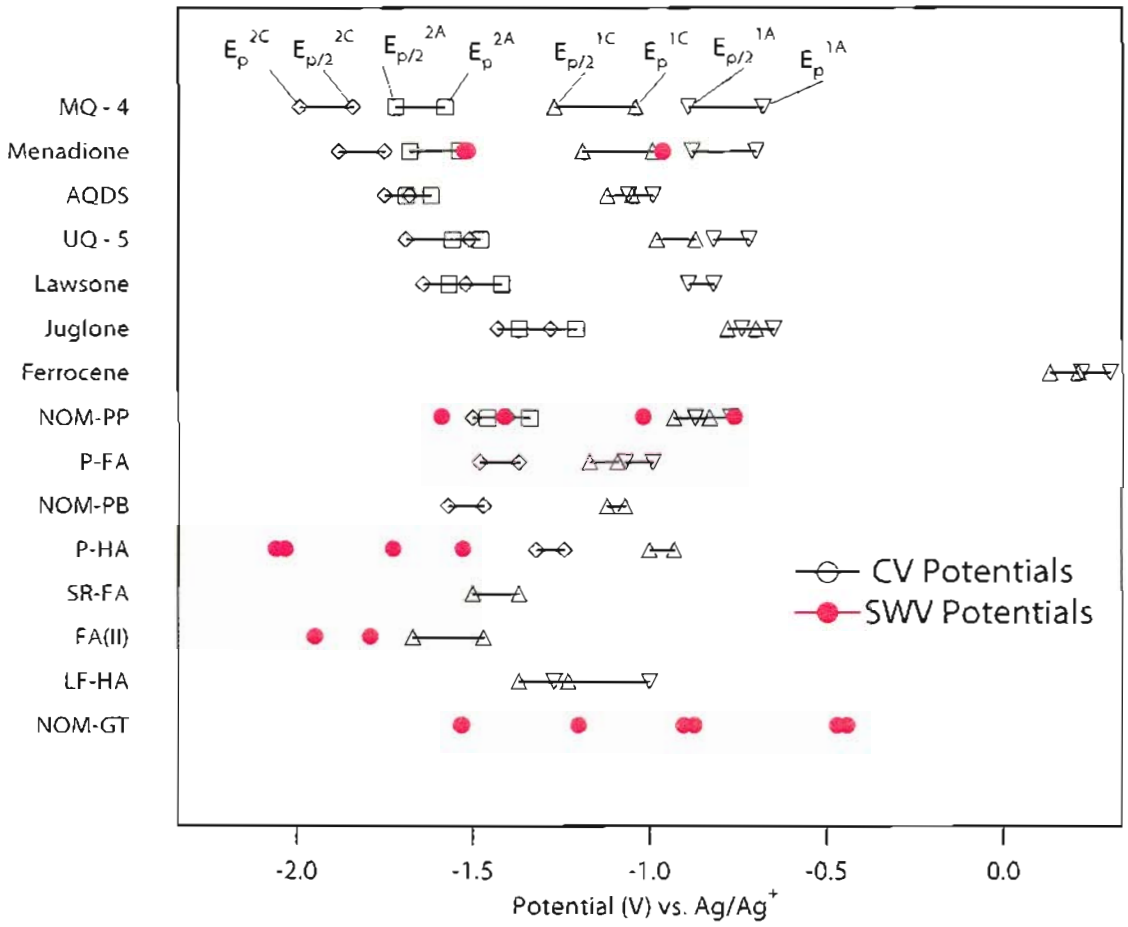

Figure 2.12. Peak potentials for all NOM and NOM model compounds for all Echem techniques.

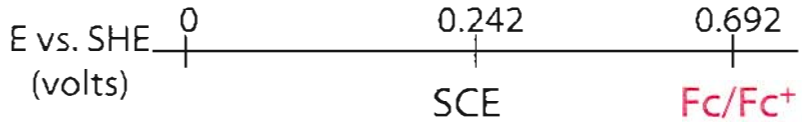

Figure 2.13. Reference electrode potentials showing how the Fc.Fc+ relates to standard reference electrode potentials (SHE).

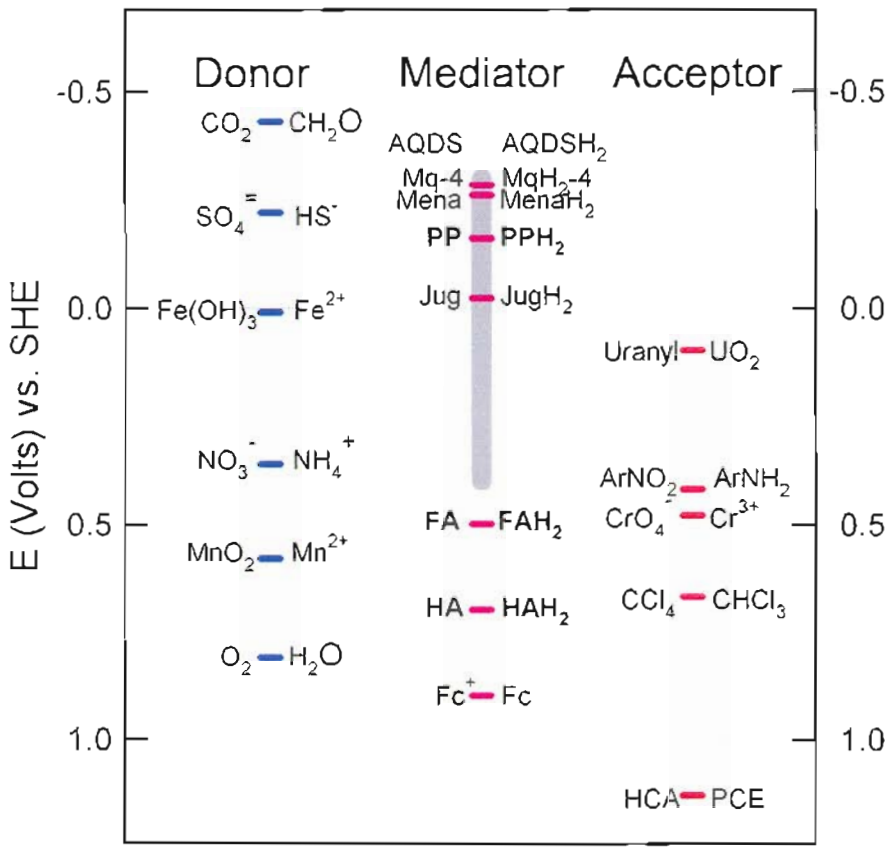

Figure 2.14. Redox ladder showing possible electrons donors, mediator and acceptors. PP stands for the NOM-PP fraction and the gray bar represents the range of peaks observed for the unfractionated NOM-GT sample.

Section 3.0. Electrochemical Properties of Micron to Nano Sized Iron Particulate

3.1. Packed Powder Electrodes for Characterizing the Reactivity of Iron Powders in Aqueous Solutions[1]

3.1.1.Abstract

Electrochemical aspects of the corrosion of iron metal have been studied using polished disk, wire, and iron coupon electrodes, but these model systems do not represent many characteristics of the granular iron used in environmental remediation applications. To address this issue, we have modified a rotating disk electrode with a cavity that accommodates a wide range of iron powders. By comparison with conventional Fe0 and Pt0 disk electrodes, we found that our powder disk electrodes (PDEs) packed with unpretreated, < 147 μm granular iron give anodic polarization curves that are unaffected by the underlying disk material and are consistent with a large electro-active surface area of iron that is initially coated with an air-formed passive film. Thus, we believe this electrode design will allow us to begin electrochemical studies of the reduction of aqueous environmental contaminants by relevant iron powders. In preparation for this, we report here on some of the experimental factors that effect response of an iron PDE in pH 8.4 borate buffer. Cavity size and rotation rate have synergistic effects that suggest

[1] Reproduced with permission from Nurmi, J. T.; Bandstra, J. Z.; Tratnyek, P. G. Packed powder electrodes for characterizing the reactivity of granular iron in borate solutions *J. Electrochem. Soc.* **2004**, *151*, B347-B353. Copyright 2005 The Electrochemical Society.

that most of the iron powder is electro-active, hydrogen evolution in the active region iskinetically limited, and iron dissolution in the active region is affected by mass transport of solutes in the cavity pore space and the formation of a passivating film.

3.1.2. Introduction

Batch, column, and electrochemical model systems have been used in many studies of the pathways, kinetics, and mechanisms by which granular iron metal reduces environmental contaminants such as trichloroethylene, 2,4,6-trinitrotoluene, and chromate [1]. In most batch and column studies, the observed changes involve solution chemistry (e.g., concentrations of the contaminant and its reduction products) andsometimes surface chemistry (e.g., growth or breakdown of the passive film). Such data have revealed a great deal about the chemistry of contaminant reduction [2-4] and the role of the passive film [5-7] in this system. However, batch and column studies provide only indirect evidence regarding the interfacial redox processes that link iron corrosion with contaminant degradation.

Electrochemical model systems allow direct monitoring and control of redox reactions at the iron-solution interface, and a number of studies have taken this approach to study contaminant reduction by iron metal. Scherer et al. [8-10] used a polished, high purity, iron rotating disk electrode to determine the contribution of mass transfer to contaminant reduction kinetics and to derive mixed-potential diagrams for the interfacial electron transfer resulting from simultaneous aqueous corrosion of iron and reduction of contaminants. Farrell et al. [11-13] used iron disk and wire electrodes to show that contaminant reduction by iron may be due to hydrogen atom transfer as well as electron transfer, and that the relative importance of these reactions varies with contaminant structure. Odziemkowski et al. [14-17] applied Raman spectroscopy to characterize the films that form on iron electrodes; demonstrating, among other things, that autoreduction of the air-formed passive film on iron contributes to the rapid reduction kinetics that are observed for many dissolved contaminants. Others have used electrochemical methods to investigate effects of buffers [18], mass transport [19], and reactive metals or metal oxides other than iron [20-23].

In all of the electrochemical studies summarized above, the working electrode was constructed of an iron disk or wire that differs in many ways from the granular iron that is used to degrade contaminants in environmental remediation contexts. This material ranges from high-purity, reagent-grade powders in the 10-100 μm size range (for laboratory studies) to partially-oxidized scrap metal that is ground to mm-sized grains (for construction and environmental engineering applications). To study relevant materials directly, it is necessary to make working electrodes from the same iron that is used in environmental applications. This could be done in three ways: (i) making an electrical connection to a single grain of iron, (ii) packing grains of iron into a cavity in a disk electrode, or (iii) filling a column that is equipped to serve as a flow-through, packed-bed electrode. The latter was used in one study of contaminant reduction by iron [7], but this electrode design accommodates only a narrow range of electrochemical techniques. A cavity electrode design was used in one study of contaminant reduction by nano-sized granular iron [24], but this particular design proved to be problematic because a conductive binder (beeswax and carbon black) was used, which resulted in a large background current. In this study, we chose to revisit the cavity electrode design because it seemed to offer the most promise for rigorous electrochemical characterization of the granular metals (and metal oxides) that are of practical environmental interest.

Part of our rationale for focusing on cavity electrodes stems from a series of recent papers that describe the use of cavity microelectrodes (CMEs, or powder microelectrodes, PMEs) [25-31] for electrochemical studies of various powders. The small size of the CME cavity (1-5 x 10-14 m3) alleviates several of the fundamental difficulties with larger cavity electrodes: there is less pore space between the grains thereby reducing diffusion distances within the electrode, and there is less internal surface area thereby reducing capacitive current and ohmic drop. These characteristics enable the CME to be modeled as equivalent to a thin-film electrode [32]. Theoretical and experimental validation of CME response has been reported using powders of PtO2 [32], Bi2O3 [25, 27, 29], and polyaniline [25, 27, 28].

There are, of course, many alternative ways to make electrodes from powders [33, 34]. From several extensive reviews of these methods [35-37], it is clear that the advantages and disadvantages of any particular method are highly dependent on their intended applications. For example, the method known as abrasive stripping voltammetry (AbrSV) has proven to be very effective for studying reactivity of iron powders [38, 39]—as we will do in this study—but AbrSV is only well suited for very fine powders (□m or less) that are significantly dissolved during analysis.

For the purposes of this study, a large cavity (0.78 cm3) electrode design was used in order to accommodate the range of iron grain sizes that are of interest for reduction of environmental contaminants (0.002 to 2 mm). With these materials, we anticipated that the difficulties noted above (long diffusion distances, high capacitive currents, and large ohmic drops) would be partly alleviated by the small size and low resistivity of the particles. To begin exploring the response of our cavity electrodes, we chose to use a reagent-grade, fine-grained iron powder (Fisher electrolytic, Felc) that is among the most frequently used in laboratory studies of contaminant reduction reactions in solution. The results provide evidence that the electrode response in this system is consistent with expectations based on previous studies done using polished iron disk electrodes, and therefore that this electrode design may be useful in future studies of contaminant reduction by environmentally-relevant iron powders.

3.1.3. Experimental

Chemicals and Reagents. All chemicals were obtained in high purity and were used as received, including boric acid (Certified A.C.S, Fisher), sodium borate (Certified A.C.S, Fisher, and argon (UHP, Airgas). All stock solutions were prepared with deoxygenated de-ionized water and stored in an anaerobic glove box. Borate buffer (pH = 8.4, 0.19 M) was made from 0.15 M H_3BO_3 and 0.0375 M $Na_2B_4O_7$.

The iron metal used was Fisher electrolytic powder (Felc) (Catalog No. I60-3) from the same lot that was used in some of our previous work [5]. The specific surface area of this particular material is 1.8 x 103 cm2 g-1 (determined by BET gas adsorption)

[40]. The Felc iron was not sieved, chemically-pretreated, or polished before it was used to make PDEs.

Fabrication of electrodes. Working electrodes were based on the rotating disk electrode (RDE) design from Pine Instruments Company (Grove City, PA). The diameter of the Pt and Fe disk electrodes were 3.0 mm. The RDFeE was custom fabricated by Pine Instruments from 99.5% purity iron rod (Metal Sample, Munford, AL). Before each use, the RDEs were polished with 1 μm diamond paste and then sonicated in methanol for 5 minutes.

The cavity for our stationary or rotating powder disk electrodes (SPDEs or RPDEs, respectively) was created by attaching a custom fabricated cap (from Pine Instruments) to the conventional $RD_{Fe}E$ or $RD_{Pt}E$. The custom caps (Kel-F or Teflon) covered the RDE tip except for a 1.4 mm diameter hole that was centered on the axis of rotation. This hole created a cavity (usually 5.1 mm deep) that was then filled with iron to form the iron powder disk electrode. The details of this design are shown in Figure 3.1.

When preparing a powder disk electrode, a thin layer of beeswax (Aldrich) was applied to the surface of the RDE before the cap was applied. The cavity was then filled by pressing the electrode tip against a glass slide that was covered with an excess of iron powder (this compression was sufficient to hold most Fe powders in the cavity). When the cavity was full, the electrode tip was warmed briefly with a heat gun to melt the wax layer, thereby ensuring that the disk material was completely protected from contact with electrolyte (which may fill the pore space after immersion). When good electrical contact was not made between the iron powder and the underlying disk, this gave open circuit potentials that were obviously spurious. In such cases, a new electrode was prepared, starting with polishing of the RDE.

Electrochemical Experiments. Experiments were carried out in a three-electrode cell (BAS, West Lafayette, IN). Along with the working electrodes described above, a Pt wire was used as the counter electrode and a Ag/AgCl electrode was used as the reference. All potentials are reported relative to the Ag/AgCl reference, and currents are reported in accord with IUPAC convention (anodic currents are positive and cathodic currents are

negative). Prior to each scan, the potential was held at -0.8 V vs. Ag/AgCl for 1 minute to establish a reproducible surface condition. All polarization experiments were done at a scan rate of 0.1 mV/s, which should ensure approximately steady-state conditions at the working electrode during polarization [41].

Electrode potentials and currents were recorded with a potentiostat (Autolab PGSTAT30, EcoChemie, Utrecht, The Netherlands) without use of the built-in resistance (iR) compensation. Instead, we measured the total uncompensated resistance (iR) at several appropriate electrode potentials because our working electrode material (iron) undergoes significant changes in composition during each scan. The iR drop (measured using the current interrupt technique [42]) was 3-42 mV for the S(R)PDE and 1-4 mV for the S(R)DE. From these results, we calculate Ru (Ru = i/V) to be between 2000 and 4000 ohms for both electrodes. Since the corresponding iR values are of the same order of magnitude for the two types of electrodes, and very small relative to all comparisons among measured potentials that are made in this paper, we concluded that Ru was insignificant for the purposes of this work. A more detailed analysis of the effects of Ru is planned for a future study of the kinetics of contaminant reactions at PDEs.

Electrochemical experiments were performed using the methods, solutions, and electrodes described above, in various permutations. To represent the various electrode designs in the discussion of results that follows, we have adopted the following nomenclature. Conventional disk electrodes employed without rotation (stationary) are designated SDE with subscripts to indicate the disk metal (e.g., $SD_{Fe}E$ and $SD_{Pt}E$). For the stationary powder disk electrodes (SPDEs), we used a second subscript to indicate what powder was packed in the cavity (i.e., $SP_{Felc}D_{Fe}E$ and $RP_{Felc}D_{Pt}E$ where the powder was Fisher electrolytic iron, Felc). If the PDE was operated with rotation, rather than stationary, the prefix R is used instead of S.

3.1.4. Results and Discussion

3.1.4.1. Preliminary Characterization.

The first step in validation of our electrode design was to show that the response of our PDE is due to the powder packed in the cavity and not the underlying disk contacting electrolyte in the interior of the cavity. To do this, the current vs. potential behavior of Pt and Fe in aqueous borate buffer (pH = 8.4) were compared for S(P)DEs (Figure 3.2) and R(P)DEs (Figure 3.3). The results are shown in two formats: linear current vs. potential (Figures 3.2A and 3.3A), and log absolute current vs. potential (Figures 3.2B and 3.3B). As expected, the conventional platinum disk electrodes ($SD_{Pt}E$ and $RD_{Pt}E$) gave polarization curves with large cathodic currents, as is typical for Pt-catalyzed H2 evolution in aqueous borate [43], and the conventional iron disk electrodes ($SD_{Fe}E$ and $RD_{Fe}E$) gave anodic polarization curves that reflect the transition from active to passive state of iron as the potential becomes more anodic, as is typical for iron in borate buffer [44-47].

In contrast to the results obtained with the conventional disk electrodes, the polarization curves obtained with PDEs (Figures 3.2 and 3.3) exhibit larger currents and no significant affect of the underlying disk material (Pt or Fe). The shapes of the PDE polarization curves, however, are similar to those of the corresponding iron disk electrodes ($SD_{Fe}E$ or $RD_{Fe}E$). Together, these qualitative results suggest that the response of our PDEs reflects electrochemical reactions of the iron powder only, and therefore, that this electrode design may allow direct electrochemical characterization of corrosion by iron powders and/or solute reactions with iron powders.

A prominent feature of the log current vs. potentials plots (Figures 3.2B and 3.3B) for the electrodes that contain iron are the singularities where net current is zero, i.e., the corrosion potentials (Ecorr). The Ecorr's for the conventional iron disk electrodes are at –0.72 V, which is typical for polished high-purity iron in pH 8.4 borate [8]. In contrast, the Ecorr's for all the PDEs are shifted to about –0.70 V. This shift in Ecorr appears to be significant, because—with practice—we were able to prepare PDEs that gave highly

reproducible Ecorr's (typically within 10 mV). The anodic shift in Ecorr of the PDEs probably reflects physical properties of the granular iron used in this study, such as microstructure, dislocation and defect densities, and/or surfacial oxide composition.

Since the majority of the electrochemical response of the PDEs seems to be attributable to the iron powder and not the underlying disk material, we concluded that the choice of disk material was unlikely to affect the results of further experiments. However, for the rest of the experiments described in this paper, the $P_{Fe|c}D_{Fe}E$ was chosen over the $P_{Fe|c}D_{Pt}E$ to eliminate the possibility of galvanic corrosion between the more noble platinum and the less noble iron. This allows us to drop the subscript Fe below the D for simplicity of notation in the rest of this paper.

3.1.4.2. Effect of Rotation Rate.

The differences between the polarization curves of the SPDEs (Figure 3.2) and the RPDEs (Figure 3.3) suggest mass transport affects that must be characterized before these electrodes can be used for any sort of quantitative analysis. For this purpose, we systematically varied rotation rate using the $RP_{Fe|c}DE$, and the results are shown in Figure 3.4. The cathodic region of Figure 3.4 shows no effect of rotation rate, indicating that the hydrogen evolution reaction ($2H_2O + 2e^- \rightarrow H_2(g) + 2OH^-$), which is the predominant cathodic half-reaction under these conditions, is kinetically limited. In contrast, the anodic region of Figure 3.4 shows an increase in current that is linear with the square root of rotation rate (see inset). This result applies to the active and passive regions of the anodic portion of the polarization curves, indicating that both the dissolution of iron and the precipitation of passivating iron oxides occur by mechanisms that are similarly influenced by mass transport. One process that might account for these results is transport of Fe^{2+} out of the electrode cavity.

Mass transport control of the dissolution from an iron disk has been previously noted and attributed to the reversible nature of the dissolution reaction in the active region [48, 49] and the formation of a porous film of precipitates such as $FeSO_4$ or $Fe(OH)_2$ in the pre-passivation stage [50-52]. In our system, this effect presumably arises because Fe2+ from anodic dissolution of Fe^0 builds up in the confined pore space of the

PDE. Increasing rotation rate improves mass transport out of the electrode cavity, thereby lowering interfacial concentrations of Fe^{2+} and allowing higher sustained corrosion rates. The same effect explains the anodic shift in passivation potential (at the peak in the polarization curves) with increased rotation rate: more rapid removal of Fe^{2+} from the cavity pore space makes a more positive potential necessary to achieve passivation.

3.1.4.3. Varying Cavity Volume.

While the data in Figures 3.2-3.4 suggest that a significant and consistent fraction of the surface area of iron in the cavity of our PDE is electro-active, they can not be used to quantify the electro-active fraction, or to determine if the iron surface area within the cavity contributes uniformly to the electrode response. To begin addressing these issues, we obtained anodic polarization curves using PDEs with cavities of varying volumes. The cap volume was varied by shortening the cap length, resulting in a less deep cavity of constant diameter. The results are shown for stationary conditions (Figure 3.5) and hydrodynamic conditions (Figure 3.6), along with data for the corresponding conventional disk electrodes ($SD_{Fe}E$ and $RD_{Fe}E$) as controls. Current was found to increase with cavity volume for all rotation rates (Figure 3.5 and 3.6) in all potential regions (except for the portion of the 3000 rpm case, shown in Figure 3.6, where the anodic current is concave down due to the formation of a passivating film in the pre-passivation region). The increase in cathodic current with cavity volume, and therefore total electrode surface area, is consistent with kinetically-limited H_2 evolution.

In our discussion of Figure 3.4, we suggest that the effect of mass transport on the dissolution of iron in a PDE could arise because the reaction rate is limited by the diffusive removal of Fe^{2+} from the electrode cavity. Under conditions where this is the case, cavity length should have little effect on the active anodic portion of the polarization curve, as was observed at 3000 rpm (Figure 3.6), but increased mass transport should eventually create a regime where the anodic current would increase with cavity volume (due to kinetically limited anodic dissolution). We did not investigate rotation rates >3000 rpm, but we did find that current in the active anodic region was dependent on cavity size at 0 rpm (Figure 3.5), which probably is due to effects of "pre-

passive" film formation [53]. The data in this region of the 0 rpm polarization curves are mostly concave down, which is consistent with pre-passivation of the iron.

An additional feature of the data in Figures 3.5 and 3.6 is the anodic shift of Ecorr (most easily seen in Figure 3.5B and 3.6B) with increasing cavity volume. This shift exists in both the 0 rpm and the 3000 rpm cases but is significantly diminished for the latter. In general, such a shift indicates that the cap volume induced increase in cathodic current (H2 evolution) is greater than the concomitant increase in anodic current (Fe0 dissolution). In the 3000 rpm case, the anodic current is unchanged while the cathodic current increases with cavity volume yielding the observed anodic shift in Ecorr. Given the kinetic limitation of H_2 generation and the fact that anodic current does increase with cap volume in the 0 rpm case might lead one to suppose that the effect of cap volume on Ecorr would be smaller for the 0 rpm case than for the 3000 rpm case. That the opposite is observed implies that the slope of the anodic current with respect to potential (in the vicinity of Ecorr) is significantly smaller for the 0 rpm case than for the 3000 rpm case. This result provides further weight to the hypothesis that the 0 rpm case is heavily influenced by a pre-passivation stage throughout the anodic region while the 3000 rpm case contains distinct regions of mass transport limited iron dissolution and pre-passivation. This shift in chemical mechanism with mass transport rate could be caused by the increased build-up of Fe^{2+} in the pore water at 0 rpm. A greater concentration of Fe^{2+} in the pore water should also result in a more cathodic passivation potential (Epeak) at lower rotation rates as is the case with the data in Figures 3.5 and 3.6.

3.1.4.4. Estimating Current Density.

If all (or a consistent fraction) of the iron in the PDE were electro-active, then the observed current should be proportional to the surface area of the iron packed in the electrode cavity, and the current density should be independent of cavity size. We tested this hypothesis by estimating current densities for the data in Figures 3.5 and 3.6 using the specific surface area of Felc iron (1.8 x 103 cm^2 g-1 [40]). The results of this calculation are shown in Figure 3.7 for stationary and hydrodynamic conditions, along

with data for the conventional disk electrodes (assuming geometric surface area = 0.071 cm^2).

The most prominent feature of Figure 3.7 is the large difference between the current densities obtained with conventional disk electrodes and PDEs. Presumably, the conventional disk electrodes give larger current densities because they are polished iron, while the iron used in the PDEs was not pretreated to remove the air-formed oxide film. Among the PDE data, the effect of cavity size on current density appears to be negligible under all conditions except in the active region for the RPDEs. The lack of effect of cavity size on current density under most conditions confirms that the majority of iron in the PDE is electro-active. In the active region for the RPDEs, smaller cavity sizes gave larger current densities presumably for the same reason that Figure 3.4A shows an effect of rotation rate only in the anodic region: smaller cavities provide less confined pore space where Fe^{2+} (from anodic dissolution of Fe^0) can build up and inhibit further corrosion.

3.1.4.5. Implications

Having satisfied the preliminary goal of this work—to demonstrate that robust and reproducible electrodes can be made from granular iron of the type that is relevant to studies of environmental remediation—we began characterizing the response of these electrodes using linear sweep voltammetry in pH 8.4 borate buffer. In this simple system, PFelcDEs gave anodic polarization curves with features that are characteristic of the various stages of iron corrosion, suggesting that they may be useful for characterizing the reactivity of granular iron under a variety of conditions that are environmentally relevant.

One application of the $P_{Felc}DE$—on which we have already reported preliminary data [54]—is characterization of changes in the passive film on granular iron due to inorganic anions such as carbonate (which is ubiquitous in environmental waters), sulfate (which is reduced to sulfide and precipitates as pyrite), and chloride (which is a product of the degradation of some key environmental contaminants). Another promising application is the comparison of different iron powders by their electrochemical response as PDEs. Our preliminary results in this area (unpublished) suggest that PDEs made from

nano-sized iron powders give anodic polarization curves that are similar to those reported in this study but with several distinctive characteristics that may be indicative of the higher reactivity of nano-sized particles that have been reported with some environmental contaminants [55-58]. Ultimately, we hope to model the polarization curves obtained using PDEs in the presence and absence of dissolved contaminants, and thereby, extract kinetic data for contaminant reduction on iron powders, as we have done with RDFeEs previously [8, 9]

To varying degrees, applications of the $P_{FeIc}DE$, such as the three described above, will be complicated by the results of this study showing that electrode response is affected by resistance to mass transport of Fe^{2+} in the restricted pore space of the PDE cavity. This complication may have unanticipated benefits, however, because restricted pore space is also characteristic of the porous media that comprise full-scale permeable reactive barriers that are used to remediate contaminated groundwater and the packed-bed column reactors that are used by many to model permeable reactive barriers. In fact, recent studies have noted evidence for more strongly reducing conditions in packed-bed reactors than is observed in mixed batch reactors and suggested that this could limit the relevance of results obtained in well mixed systems [59]. For this reason, results obtained with $P_{FeIc}DEs$ may eventually prove to be more relevant to understanding the chemistry of permeable reactive barriers than what has been achieved with $RD_{Fe}Es$.

3.1.4.6. Acknowledgments

This research was sponsored by the Nanoscale Science, Engineering, and Technology program of the U.S. Department of Energy, Office of Science, (DE-AC06-76RLO 1830). This paper has not been subject to review by DOE and therefore does not necessarily reflect the views of DOE, and no official endorsement should be inferred.

3.1.4.7. References

[1] Tratnyek, P. G.; Scherer, M. M.; Johnson, T. J.; Matheson, L. J. In *Chemical Degradation Methods for Wastes and Pollutants: Environmental and Industrial Applications*; Tarr, M. A., Ed.; Marcel Dekker: New York, 2003; pp 371-421.

[2] Matheson, L. J.; Tratnyek, P. G. Reductive dehalogenation of chlorinated methanes by iron metal *Environ. Sci. Technol.* **1994**, *28*, 2045-2053.

[3] Fennelly, J. P.; Roberts, A. L. Reaction of 1,1,1-trichloroethane with zero-valent metals and bimetallic reductants *Environ. Sci. Technol.* **1998**, *32*, 1980-1988.

[4] Arnold, W. A.; Roberts, A. L. Pathways and kinetics of chlorinated ethylene and chlorinated acetylene reaction with Fe(0) particles *Environ. Sci. Technol.* **2000**, *34*, 1794-1805.

[5] Agrawal, A.; Ferguson, W. J.; Gardner, B. O.; Christ, J. A.; Bandstra, J. Z.; Tratnyek, P. G. Effects of carbonate species on the kinetics of 1,1,1-trichloroethane by zero-valent iron *Environ. Sci. Technol.* **2002**, *36*, 4326-4333.

[6] Gaspar, D. J.; Lea, A. S.; Engelhard, M. H.; Baer, D. R.; Miehr, R.; Tratnyek, P. G. Evidence for localization of reaction upon reduction of CCl_4 by granular iron *Langmuir* **2002**, *18*, 7688-7693.

[7] Ritter, K.; Odziemkowski, M. S.; Gillham, R. W. An in situ study of the role of surface films on granular iron in the permeable iron wall technology *J. Contam. Hydrol.* **2002**, *55*, 87-111.

[8] Scherer, M. M.; Westall, J. C.; Ziomek-Moroz, M.; Tratnyek, P. G. Kinetics of carbon tetrachloride reduction at an oxide-free iron electrode *Environ. Sci. Technol.* **1997**, *31*, 2385-2391.

[9] Scherer, M. M.; Johnson, K.; Westall, J. C.; Tratnyek, P. G. Mass transport effects on the kinetics of nitrobenzene reduction by iron metal *Environ. Sci. Technol.* **2001**, *35*, 2804-2811.

[10] Scherer, M. M.; Westall, J. C.; Tratnyek, P. G. Discussion on "Electrochemical and Raman spectroscopic studies of the influence of chlorinated solvents on the corrosion behaviour of iron in borate buffer and in simulated groundwater" [*Corrosion Science* 42 (2000) 1921-1939] *Corr. Sci.* **2001**, *44*, 1151-1157.

[11] Farrell, J.; Melitas, N.; Li, T. Electrochemical and column investigation of iron-mediated reductive dechlorination of trichloroethylene and perchloroethylene *Environ. Sci. Technol.* **2000**, *34*, 2549-2556.

[12] Li, T.; Farrell, J. Electrochemical investigation of the rate-limiting mechanisms for trichloroethylene and carbon tetrachloride reduction at iron surfaces *Environ. Sci. Technol.* **2001**, *35*, 3560-3565.

[13] Wang, J.; Farrell, J. Investigating the role of atomic hydrogen on chloroethene reactions with iron using Tafel analysis and electrochemical impedance spectroscopy *Environ. Sci. Technol.* **2003**, *37*, 3891-3896.

[14] Bonin, P. M. L.; Odziemkowski, M. S.; Gillham, R. W. Influence of chlorinated solvents on polarization and corrosion behaviour of iron in borate buffer *Corr. Sci.* **1998**, *40*, 1391-1409.

[15] Odziemkowski, M. S.; Schuhmacher, T. T.; Gillham, R. W.; Reardon, E. J. Mechanism of oxide film formation on iron in simulating groundwater solutions: Raman spectroscopic studies *Corr. Sci.* **1998**, *40*, 371-389.

[16] Bonin, P. M. L.; Odziemkowski, M. S.; Reardon, E. J.; Gillham, R. W. In situ identification of carbonate-containing green rust on iron electrodes in solutions simulating groundwater *J. Solut. Chem.* **2000**, *29*, 1061-1074.

[17] Bonin, P. M. L.; Jedral, W.; Odziemkowski, M. S.; Gillham, R. W. Electrochemical and Raman spectroscopic studies of the influence of chlorinated solvents on the corrosion behaviour of iron in borate buffer and in simulated groundwater *Corr. Sci.* **2000**, *42*, 1921-1939.

[18] Lavine, B. K.; Auslander, G.; Ritter, J. Polarographic studies of zero valent iron as a reductant for remediation of nitroaromatics in the environment *Microchem J.* **2001**, *70*, 69-83.

[19] Bigg, T.; Judd, S. J. Electrochemical monitoring of water remediation by metallic iron *J. Appl. Electrochem.* **2001**, *31*, 1339-1344.

[20] Warren, K. D.; Arnold, R. G.; Bishop, T. L.; Lindholm, L. C.; Betterton, E. A. Kinetics and mechanism of reductive dehalogenation of carbon tetrachloride using zero-valence metals *J. Haz. Mat.* **1995**, *41*, 217-227.

[21] Liu, Z.; Arnold, R. G.; Betterton, E. A.; Festa, K. D. Electrolytic reduction of CCl_4—Effects of cathode material and potential on kinetics, selectivity, and product stoichiometry *Environ. Eng. Sci.* **1999**, *16*, 1-13.

[22] Liu, Z.; Betterton, E. A.; Arnold, R. G. Electrolytic reduction of low molecular weight chlorinated aliphatic compounds: structural and thermodynamic effects on process kinetics *Environ. Sci. Technol.* **2000**, *34*, 804-811.

[23] Logue, B. A.; Westall, J. C. Kinetics of reduction of nitrobenzene and carbon tetrachloride at an iron-oxide coated gold electrode *Environ. Sci. Technol.* **2003**, *37*, 2356-2362.

[24] Ponder, S. M.; Darab, J. G.; Bucher, J.; Caulder, D.; Craig, I.; Davis, L.; Edelstein, N.; Lukens, W.; Nitsche, H.; Rao, L.; Shuh, D. K.; Mallouk, T. E. Surface chemistry and electrochemistry of supported zerovalent iron nanoparticles in the remediation of aqueous metal contaminants *Chem. Mat.* **2001**, *13*, 479-486.

[25] Vivier, V.; Cachet-Vivier, C.; Wu, B. L.; Cha, C.-S.; Nedelec, J. Y.; Yu, L. T. Cavity microelectrode for studying powder materials at a high potential scan rate *Electrochem. Solid State Lett.* **1999**, *2*, 385-387.

[26] Vivier, V.; Cachet-Vivier, C.; Mezaille, S.; Wu, B. L.; Cha, C.-S.; Nedelec, J. Y.; Fedoroff, M.; Michel, D.; Yu, L. T. Electrochemical study of Bi_2O_3 and $Bi_2O_2CO_3$ by means of a cavity microelectrode. I. Observed phenomena and direct analysis of results *J. Electrochem. Soc.* **2000**, *147*, 4252-4262.

[27] Cachet-Vivier, C.; Vivier, V.; Cha, C. S.; Nedelec, J. Y.; Yu, L. T. Electrochemistry of powder material studied by means of the cavity microelectrode (CME) *Electrochim. Acta* **2001**, *47*, 181-189.

[28] Vivier, V.; Cachet-Vivier, C.; Cha, C. S.; Nedelec, J. Y.; Yu, L. T. Cavity microelectrode for studying battery materials: application to polyaniline powder *Electrochem. Commun. 2* **2000**, *2*, 180-185.

[29] Vivier, V.; Régis, A.; Sagon, G.; Nedelec, J. Y.; Yu, L. T.; Cachet-Vivier, C. Cyclic voltammetry study of bismuth oxide Bi_2O_3 powder by means of a cavity microelectrode coupled with Raman microspectrometry *Electrochim. Acta* **2001**, *46*, 907-914.

[30] Vivier, V.; Cachet-Vivier, C.; Michel, D.; Nedelec, J. Y.; Yu, L. T. Voltamperommetric study of chemically made polyaniline powder with cavity microelectrode technique *Synth. Met.* **2002**, *126*, 253-262.

[31] Cha, C.-S.; Li, C. M.; Yang, H. X.; Liu, P. F. Powder microelectrodes *J. Electroanal. Chem.* **1994**, *368*, 47-54.

[32] Cachet-Vivier, C.; Vivier, V.; Cha, C. S.; Nédélec, J.-Y.; Yu, L. T. Electrocatalytic hydrogenation of C_2H_4 on PtO_2 powder. A study of surface processes occurring at powder materials by cavity microelectrode *J. Electrochem. Soc.* **2001**, *148*, E177-E182.

[33] Longhi, M.; Formaro, L. Oxide electrodes. A new technique to bind oxide powders onto Au substrates *Electrochem. Commun.* **2002**, *4*, 123-127.

[34] Totir, D. A.; Cahan, B. D.; Scherson, D. A. Electrochemical characterization of lithiated transition metal oxide cathode particles in the absence of carbon, binders and other additives *Electrochim. Acta* **1999**, *45*, 161-166.

[35] Grygar, T.; Bezdicka, P.; Hradil, D.; Pikna, L. In *Solid State Chemistry V*, 2003; Vol. 90-91, pp 45-49.

[36] Grygar, T.; Marken, F.; Schroder, U.; Scholz, F. Electrochemical analysis of solids. A review *Coll. Czech. Chem. Commun.* **2002**, *67*, 163-208.

[37] Scholz, F.; Meyer, B. Electrochemical solid-state analysis: state of the art *Chem. Soc. Rev.* **1994**, *23*, 341-347.

[38] Galova, M.; Grygar, T.; Pikna, L.; Lux, L. Electrochemical study on the reactivity of Fe powders *Chemia Analityczna* **2003**, *48*, 293-303.

[39] Lux, L.; Galova, M.; Hezcaronelova, M.; Markusova, K. Investigation of the reactivity of powder surfaces by abrasive voltammetry *J. Solid State Electrochem.* **1999**, *3*, 288-292.

[40] Alowitz, M. J.; Scherer, M. M. Kinetics of nitrate, nitrite, and Cr(VI) reduction by iron metal *Environ. Sci. Technol.* **2002**, *36*, 299-306.

[41] Drazic, D. M.; Zecevic, S. K. Transient phenomena during the anodic polarization of iron *Corr. Sci.* **1985**, *25*, 209-216.

[42] EG&G Princeton Applied Research "Technical Bulletin: Potential error correction (IR compensation)," 1986.

[43] Bard, A. J.; Faulkner, L. R. *Electrochemical Methods. Fundamentals and Applications*; 2nd ed.; Wiley: New York, 2001.

[44] Sato, N. In *Passivity of Metals*; Frankenthal, R. P., Kruger, J., Eds.; Electrochemical Society: Princeton, NJ, 1978; pp 29-58.

[45] Cohen, M. In *Passivity of Metals*; Frankenthal, R. P., Kruger, J., Eds.; Electrochemical Society: Princeton, NJ, 1978; pp 521-545.

[46] Jovancicevic, V.; Kainthla, R. C.; Tang, Z.; Yang, B.; Bockris, J. O. M. The passive film on iron: an ellipsometric-spectroscopic study *Langmuir* **1987**, *3*, 388-395.

[47] Oblonsky, L. J.; Devine, T. M. A surface enhanced Raman spectroscopic study of the passive films formed in borate buffer on iron, nickel, chromium and stainless steel *Corr. Sci.* **1995**, *37*, 17-41.

[48] Despic, A. R. In *Comprehensive Treatise of Electrochemistry. Vol. 7. Kinetics and Mechanisms of Electrode Processes*; Conway, B. E., Bockris, J. O. M., Yeager, E., Khan, S. U. M., White, R. E., Eds.; Plenum: New York, 1983; pp 451-528.

[49] Kimball, G. E. The absolute rates of heterogeneous reactions. II. Electrode reactions *J. Chem. Phys.* **1940**, *8*, 199-204.

[50] Mattos, O. R. Anodic dissolution of metals: Process control by mass transport *J. Chim. Phys.-Chim. Biol.* **1996**, *93*, 777-792.

[51] Barcia, O. E.; Mattos, O. R.; Tribollet, B. Anodic dissolution of iron in acid sulfate under mass transport control *J. Electrochem. Soc.* **1992**, *139*, 446-453.

[52] Barcia, O. E.; Mattos, O. R.; Pebere, N.; Tribollet, B. Anodic dissolution of metals under mass transport control *Electrochim. Acta* **1996**, *41*, 1385-1391.

[53] El Miligy, A. A.; Geana, D.; Lorenz, W. J. A theoretical treatment of the kinetics of iron dissolution and passivation *Electrochim. Acta* **1975**, *20*, 273-281.

[54] Nurmi, J. T.; Tratnyek, P. G. In *226th National Meeting, 7-11 September 2003*; American Chemical Society: New York, NY, 2003; Vol. 43, No. 2, pp 691-695.

[55] Lien, H.-L.; Zhang, W.-X. Transformation of chlorinated methanes by nanoscale iron particles *J. Environ. Eng.* **1999**, *125*, 1042-1047.

[56] Choe, S.; Chang, Y. Y.; Hwang, K. Y.; Khim, J. Kinetics of reductive denitrification by nanoscale zero-valent iron *Chemosphere* **2000**, *41*, 1307-1311.

[57] Lien, H.-L.; Zhang, W.-X. Nanoscale iron particles for complete reduction of chlorinated ethenes *Colloid Surf. A-Physicochem. Eng. Asp.* **2001**, *191*, 97-105.

[58] Schrick, B.; Blough, J. L.; Jones, A. D.; Mallouk, T. E. Hydrodechlorination of trichloroethylene to hydrocarbons using bimetallic nickel-iron nanoparticles *Chem. Mat.* **2002**, *14*, 5140-5147.

[59] Miehr, R.; Bandstra, J. Z.; Po, R.; Tratnyek, P. G. In *225th National Meeting, 23-27 March 2003*; American Chemical Society: New Orleans, LA, 2003; Vol. 43, No. 1, pp 644-648.

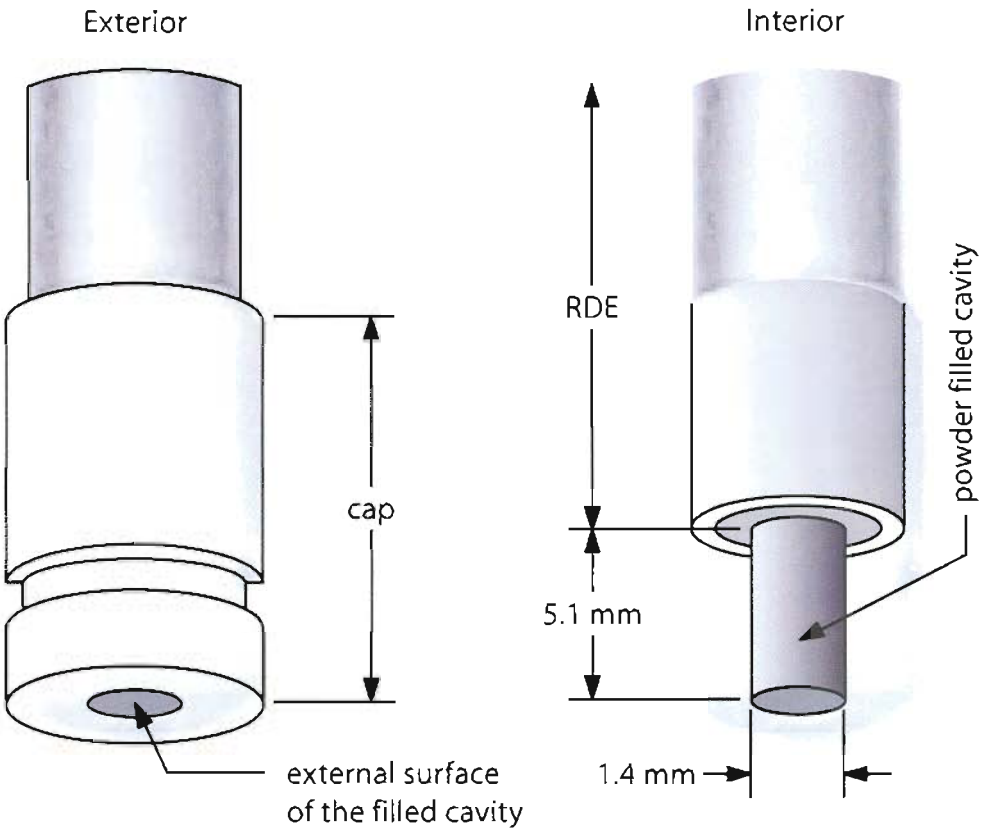

Figure 3.1. Diagram of the exterior and interior dimensions of the powder disk electrode (PDE) developed for use in this study.

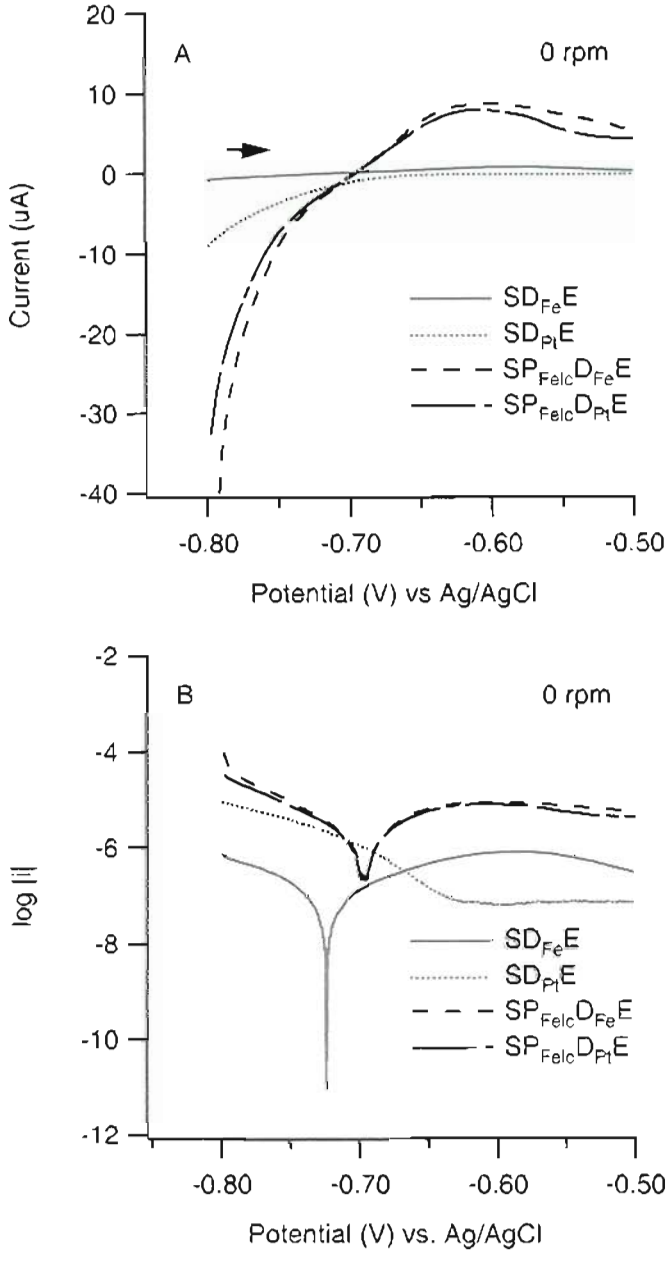

Figure 3.2. A. Current vs. potential plot of anodic polarization curves for conventional stationary disk electrodes ($SD_{Fe}E$ and $SD_{Pt}E$), and two stationary powder disk electrodes ($SP_{FeIc}D_{Fe}E$ and $SP_{FeIc}D_{Pt}E$) in anaerobic aqueous borate (pH = 8.4, 0.19 M). Scan rate = 0.1 mV/s. B. Same data plotted as log absolute current vs. potential.

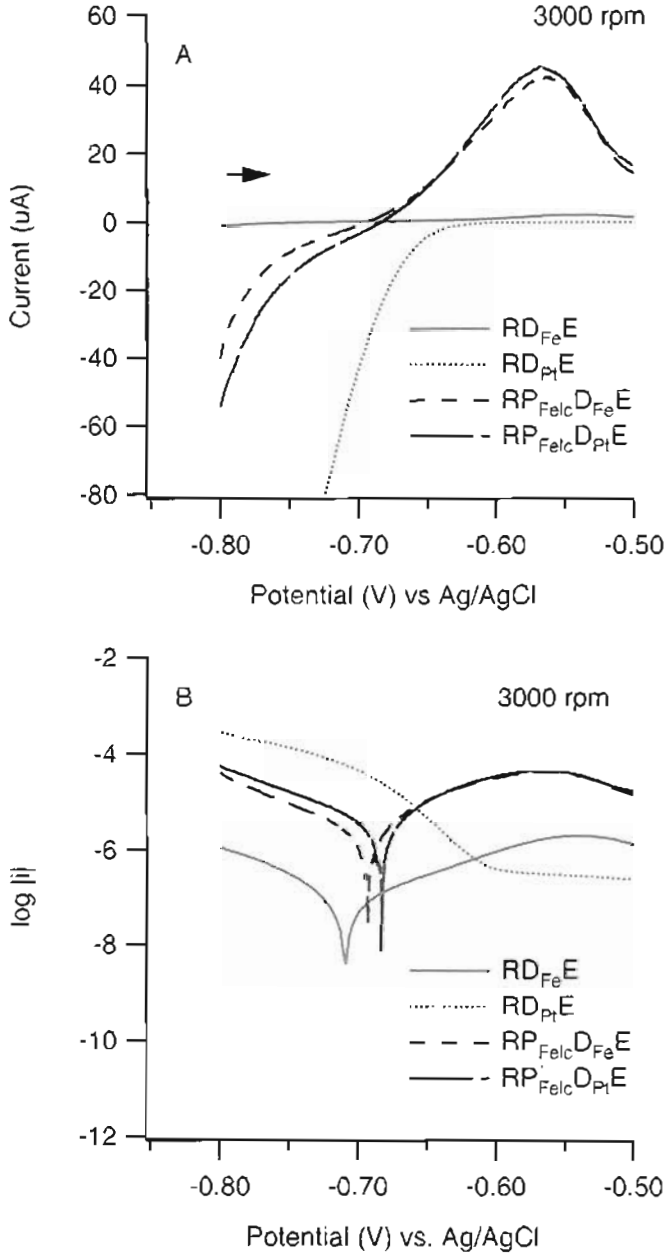

Figure 3.3. A. Current vs. potential plot of anodic polarization curves for conventional rotating disk electrodes ($RD_{Fe}E$ and $RD_{Pt}E$), and two rotating powder disk electrodes ($RP_{FeIc}D_{Fe}E$ and $RP_{FeIc}D_{Pt}E$) in anaerobic aqueous borate (pH = 8.4, 0.19 M). Scan rate = 0.1 mV/s. Rotation = 3000 rpm B. Same data plotted as log absolute current vs. potential.

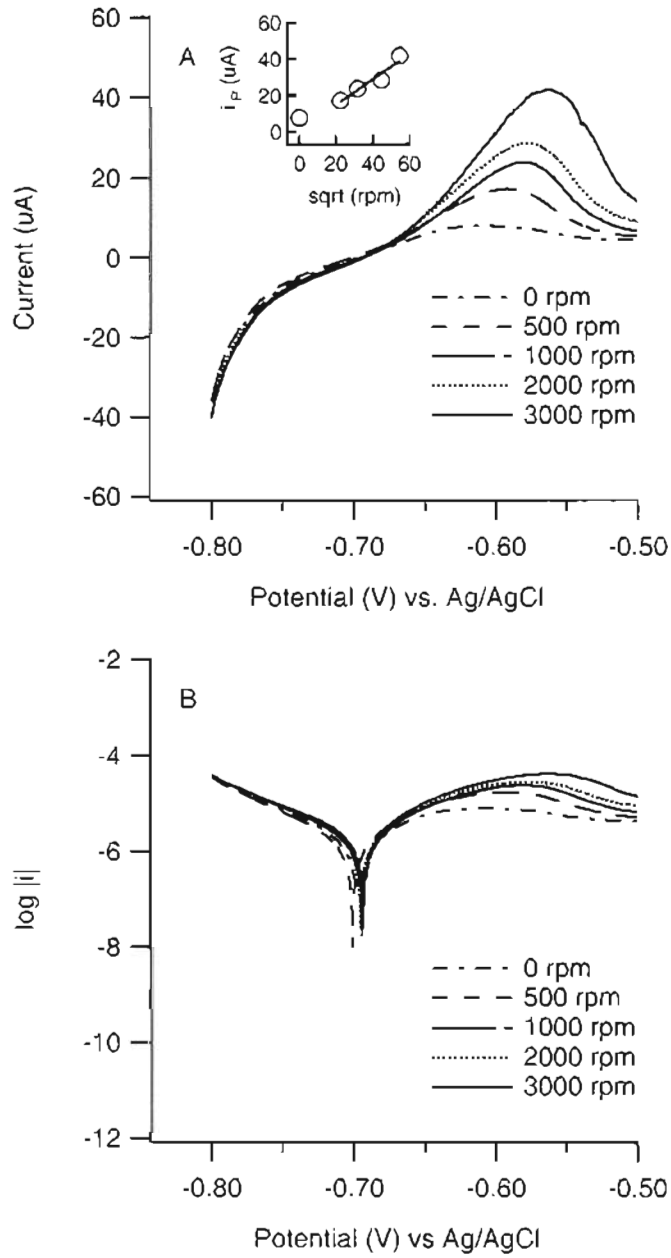

Figure 3.4. A. Current vs. potential plot of anodic polarization curves for the $RP_{Felc}DE$ in anaerobic aqueous borate (pH = 8.4, 0.19 M) and various rotation rates. Scan rate = 0.1 mV/s. Inset: peak current (iP) vs. square root of the rotation rate. B. Same data plotted as log absolute current vs. potential.

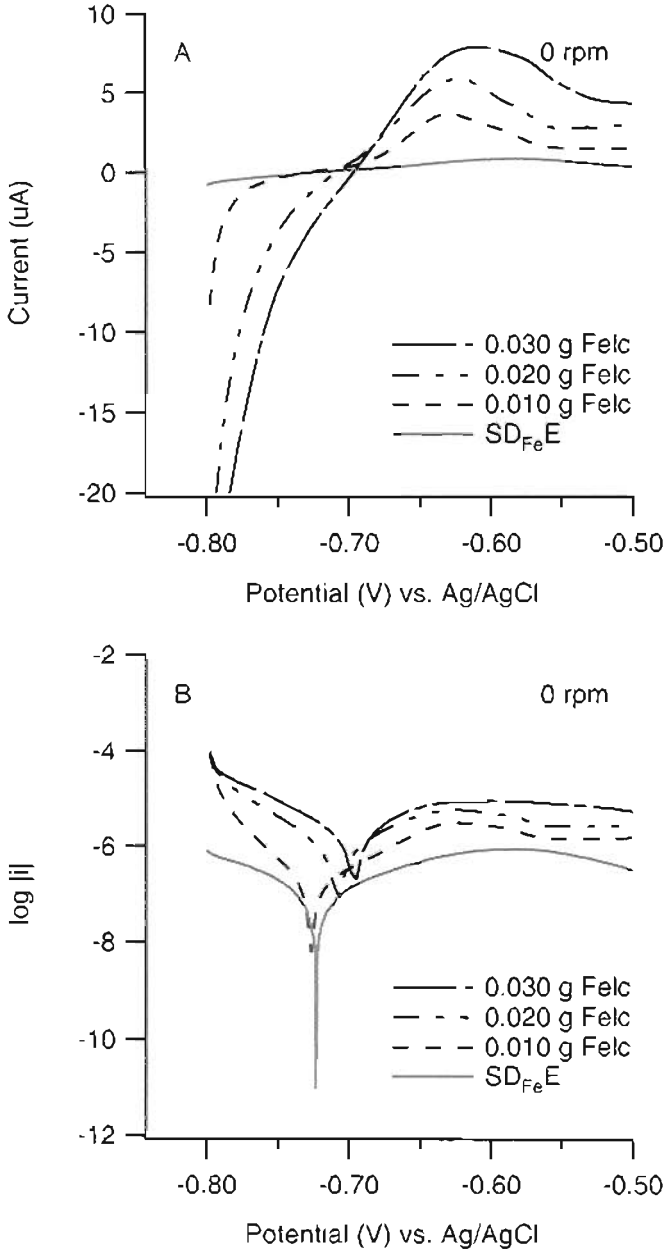

Figure 3.5. A. Current vs. potential plot of anodic polarization curves for the $RP_{Felc}DE$ in anaerobic aqueous borate (pH = 8.4, 0.19 M) using various amounts of iron powder under stationary conditions (0 rpm). Scan rate = 0.1 mV/s. B. Same data plotted as log absolute current vs. potential.

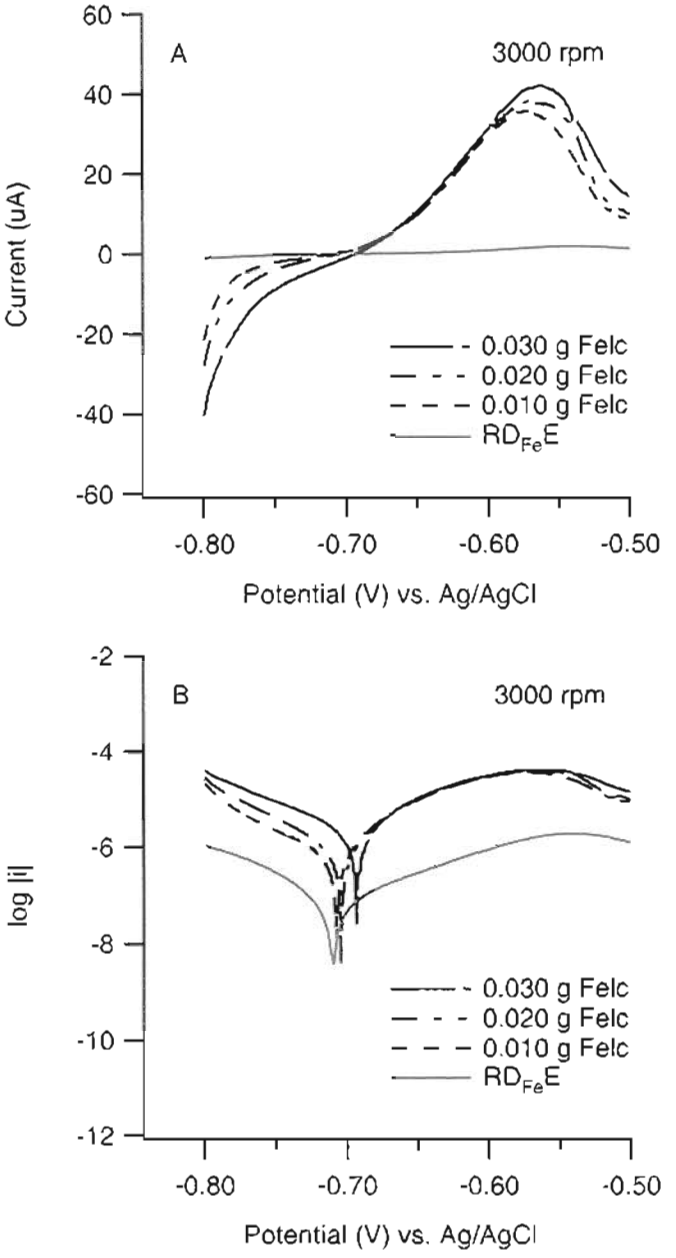

Figure 3.6. A. Current vs. potential plot of anodic polarization curves for the $RP_{Felc}DE$ in anaerobic aqueous borate (pH = 8.4, 0.19 M) using various amounts of iron powder under hydrodynamic conditions (3000 rpm). Scan rate = 0.1 mV/s. B. Same data plotted as log absolute current vs. potential.

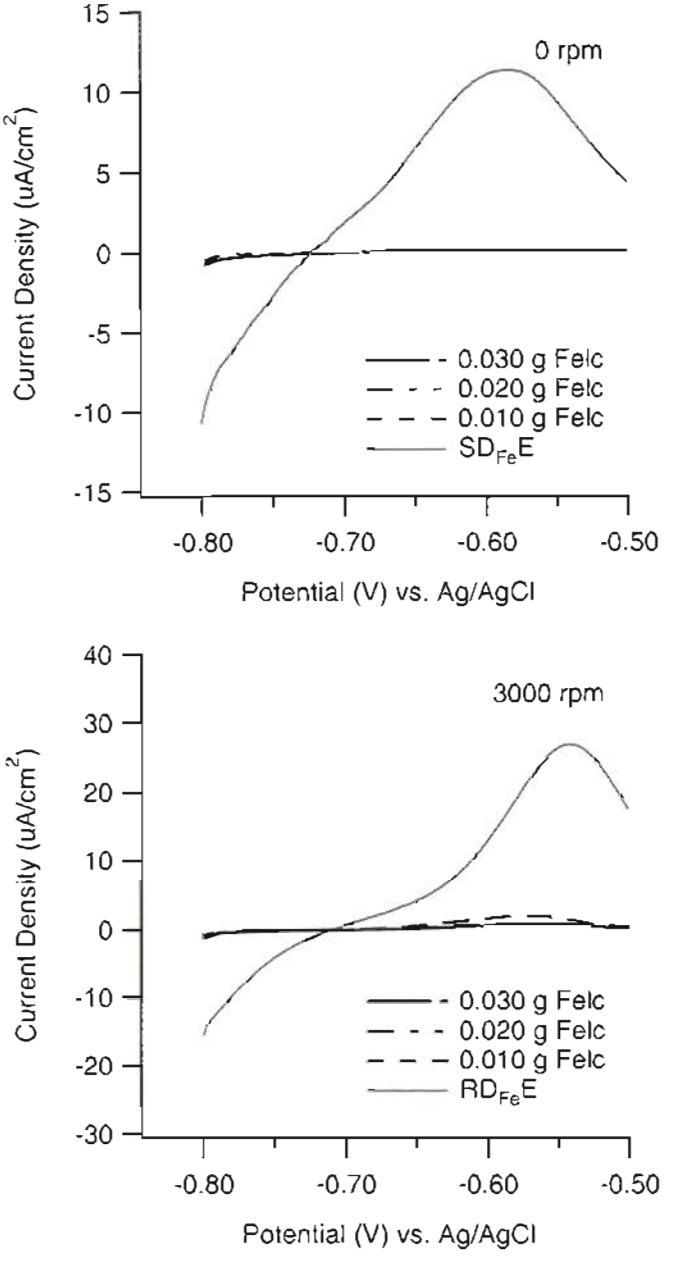

Figure 3.7. A. Current density (μA cm-2) vs. potential plot of anodic polarization curves for the $RP_{Felc}DE$ in anaerobic aqueous borate (pH = 8.4, 0.19 M) under stationary conditions (0 rpm). Scan rate = 0.1 mV/s. B. Current density (μA cm-2) vs. potential plot of anodic polarization curves for the $RP_{Felc}DE$ in anaerobic aqueous borate (pH = 8.4, 0.19 M) under hydrodynamic conditions (3000 rpm). Scan rate = 0.1 mV/s.

3.2. Characterization and Properties of Metallic Iron and Iron-Oxide Nanoparticles: Spectroscopy, Electrochemistry, and Kinetics [1]

3.2.1. Abstract

There are reports that nano-sized zero-valent iron (Fe^0) exhibits greater reactivity than micro-sized particles of Fe^0, and it has been suggested that the higher reactivity of nano-Fe^0 may impart advantages for groundwater remediation or other environmental applications. However, most of these reports are preliminary in that they leave a host of potentially significant (and often challenging) material or process variables either uncontrolled or unresolved. In an effort to better understand the reactivity of nano-Fe^0, we have used a variety of complementary techniques to characterize two widely studied nano-Fe^0 preparations: one synthesized by reduction of goethite with heat and H_2 (Fe^{H2}) and the other by reductive precipitation with borohydride (Fe^{BH}). Fe^{H2} is a two-phase material consisting of 40 nm α-Fe^0 (made up of crystals approximately the size of the particles) and Fe_3O_4 particles of similar size or larger containing reduced sulfur; whereas Fe^{BH} is mostly 20-80 nm metallic Fe particles (aggregates of <1.5 nm grains) with an oxide shell/coating that is high in oxidized boron. The Fe^{BH} particles further aggregate into chains. Both materials exhibit corrosion potentials that are more negative than

[1] Reproduced with permission from Nurmi, J. T.; Tratnyek, P. G.; Sarathy, V.; Baer, D. R.; Amonette, J. E.; Pecher, K.; Wang, C.; Linehan, J. C.; Matson, D. W.; Penn, R. L.; Driessen, M. D. Characterization and properties of metallic iron nanoparticles: spectroscopy, electrochemistry, and kinetics *Environ. Sci. Technol.* **2005**, *39*, 1221-1230.

nano-sized Fe_2O_3, Fe_3O_4, micro-sized Fe^0, or a solid Fe^0 disk, which is consistent with their rapid reduction of oxygen, benzoquinone, and carbon tetrachloride. Benzoquinone—which presumably probes inner-sphere surface reactions—reacts more rapidly with Fe^{BH} than Fe^{H2}, whereas carbon tetrachloride reacts at similar rates with Fe^{BH} and Fe^{H2}, presumably by outer-sphere electron transfer. Both types of nano-Fe^0 react more rapidly than micro-sized Fe^0 based on mass-normalized rate constants, but surface-area-normalized rate constants do not show a significant nano-size effect. The distribution of products from reduction of carbon tetrachloride is more favorable with Fe^{H2}, which produces less chloroform than reaction with Fe^{BH}.

3.2.2. Introduction

There are many variations on the use of granular zero-valent iron metal (Fe^0) for removal of contaminants from soil and water [1]. Among these, the use of nano-sized particles of Fe^0 (or bimetallic combinations of Fe^0 and catalytic metals such as Pd) is currently getting the most attention [2]. Two potential advantages of nano-sized Fe^0 over the construction-grade scrap Fe^0 used in conventional permeable reactive barriers (PRBs) are that nanoparticles may be delivered to deep contamination zones by injection and nano-sized Fe^0 may be more effective at degrading some contaminants. The appeal of this technology has led to rapid adoption by the engineering community, and a number of field demonstrations have already been completed and described in the literature [3, 4].

There is, however, not yet consensus on a number of fundamental issues regarding the potential effectiveness of nano-Fe^0 for environmental engineering applications. In particular, issues that are current subjects of research include: (*i*) the mobility of nanoparticles under subsurface conditions, (*ii*) the kinetics and products of contaminant degradation by nano-Fe^0, and (*iii*) the persistence of nano-Fe^0 as a reactive phase during the time period of treatment. The first issue is being addressed by others, such as those involved in the field sites noted above. With respect to the issue of reactivity, many studies have concluded that nano-Fe^0 degrades contaminants more rapidly than conventional forms of granular Fe^0 [2, 5-13], although the basis for these

comparisons has not always been clear. Another reactivity issue is that nano-Fe^0 might produce different distributions of products, but this possibility does not appear to have been thoroughly investigated. On the issue of longevity, it is clear that the reactivity of nano-Fe^0 suspensions can persist for at least 6-8 weeks [14], but there does not appear to have been a detailed characterization of the "diagenesis" of nano-Fe^0 or how diagenetic processes (e.g., alterations resulting from exposure to groundwater) affect reactivity with contaminants.

One reason that nano-sized Fe^0 particles might exhibit greater rates of reaction with contaminants is simply that their large specific surface area provides more of the sites on which reaction occurs. For contaminants that are degraded by micro-sized Fe^0—such as trichloroethylene or carbon tetrachloride—there is a well documented dependence of contaminant reduction rate with surface area of Fe^0 [1, 15]. However, increased surface area alone is not adequate to explain why nano-Fe^0 apparently reduces some compounds that exhibit negligible reactivity with micro-Fe^0 particles (such as polychlorinated biphenyls [9, 10]). Other possible reasons for why nano-Fe^0 might exhibit enhanced reactivity include higher density of reactive surface sites and greater intrinsic reactivity of surface sites.

There are several reasons that smaller particle size might result in a greater density of reactive surface sites or surface sites of higher intrinsic reactivity [16, 17]. Below about 10 nm, properties such as the free energy and work function change significantly with particle size, following classical equations such as the Gibbs-Thompson relation between particle size and energy [18]. As particle size decreases, particle dimensions approach the size of certain physical length scales—such as the electron mean-free path and the electron wavelength—and this results in quantum size effects that alter the electronic structure of the particle [19-21]. For metal particles, quantum effects influence physical and chemical properties when the particle size is less than about 5 nm [18, 22-25]. Similar effects will arise at larger particle sizes (10-150 nm) for materials with lower electron density, such as oxides and semiconductors [26, 27].

These quantum effects cause changes in the Fermi level and band gap, which lead to increases in reactivity with decreasing particle size [28].

Nanoparticles containing Fe^0 must be surrounded by some type of passivating layer—such as a shell of oxide—under environmental conditions. Although an Fe^0 core may exhibit some of the quantum effects that are characteristic of entirely metallic nanoparticles, the particle as a whole will exhibit properties of the core and the shell [17]. Recent studies of core-shell Fe^0 nanoparticles have shown that the composition of the oxide shell—and therefore the nature of its surface sites—is influenced by particle size [29] and the particle's environment [30]. In addition to the bulk composition of the shell, impurities (e.g., dopants) will affect the reactivity of particle surface [31]. Furthermore, assuming that the reactivity of core-shell nanoparticles is driven by oxidation of the Fe^0 core, then charge and mass transport through the shell will be necessary for sustained reaction, and the kinetics of these transport processes may be important determinants of adsorbate (contaminant) reduction kinetics.

In addition to core-shell structure, another important characteristic of reactive nanoparticles is their strong tendency to aggregate in solution. Although there are ways to form stable suspensions of dispersed nanoparticles in laboratory or engineered media [e.g., 32, 33, 34], aggregation of nanoparticles is difficult to avoid under environmental conditions. One consequence of the aggregation of nanoparticles into larger clusters is ambiguity regarding whether a property of the material reflects the aggregates or their nano constituents. This issue is especially important with respect to the determination of surface area because the reactive surface area of highly aggregated nanoparticles suspended in solution is likely to be very different from the surface area measured on dry, dispersed nano-sized powders.

As part of an effort to determine which of the above size and structure effects control the reactivity of nano-Fe^0 under environmental conditions, we arranged to have sub-samples of two types of nano-Fe^0 characterized by a comprehensive array of complementary methods. The two types of nanoparticles used in this study were selected

because they represent distinct and prototypical methods of synthesis, and they have been used in both laboratory and field studies for contaminant degradation. The methods used to characterize these particles gave size, shape, surface area, composition and crystallinity of the bulk and surface material, corrosion potential, and reactivity with respect to two model contaminants (benzoquinone and carbon tetrachloride). The study demonstrates both similarities and fundamental differences in the physical structure and reaction pathways of the two types of nano-sized iron particles.

By necessity, this study also addresses some of the many methodological issues associated with the study of highly reactive nano-sized materials that change over time, with handling, and during analysis. Because nano-Fe^0 is often stabilized for distribution in aqueous suspensions or pastes, and these materials do not allow accurate and reproducible dispensation of quantities of particles for experimentation, we investigated a procedure we call "flash-drying" to remove water (and associated solutes) while minimizing other changes in the particle composition. Another major methodological issue that we address is the determination of the particle surface area that is relevant to quantifying their reactivity in solution. This issue proved to be a major obstacle in making quantitative comparisons of reactivity among nano- and micro-sized Fe^0 particles.

3.2.3. Experimental

Reagents. All chemicals were obtained in high purity and were used as received, including boric acid (Fisher, Certified A.C.S), sodium borate (Fisher, Certified A.C.S), benzoquinone (Acros, 99+%), hydroquinone (Fisher, Laboratory Grade), N-[2-hydroxyethyl] piperazine-N'-[3-propanesulfonic acid] (Sigma, 99.5%), carbon tetrachloride (Sigma, HPLC grade), chloroform (Sigma, HPLC grade), and argon (Airgas, UHP). All stock solutions were prepared with N_2-sparged deionized water and stored in an anaerobic chamber. Borate buffer (pH = 8.4) was made from 0.15 M H_3BO_3 and 0.0375 M $Na_2B_4O_7$. EPPS buffer was made from 0.01M N-[2-hydroxyethyl] piperazine-N'-[3-propanesulfonic acid], by titrating with NaOH to pH 8.4.

Iron Samples. The iron and iron oxide powders characterized in this study were from five sources. Characteristics provide by the suppliers are summarized in Table 3.1. Nano-sized metallic iron was obtained from Toda America, Inc. (Schaumberg, IL) and W.-X. Zhang (Lehigh University). The material from Toda (Fe^{H2}) was the commercial product known as RNIP-10DS, which is produced by reduction of goethite and hematite particles with H_2 at high temperatures (200-600 °C) [35]. Two samples of this material were received, and proved to be similar, but all the data presented here are from the second lot. Fe^{H2} is known to be a two-phase material consisting of Fe_3O_4 and α-Fe^0 [35]; however, no effort was made to assure "uniform" mixing of the two phases. This material has been used in previous laboratory studies [9, 36] and at least one field test [37]. The material from Zhang (Fe^{BH}) was synthesized by reductive precipitation of $FeCl_3$ with $NaBH_4$ [5]. Three different batches of this material were provided and they proved to be substantially similar. This material should be similar to the nano-Fe^0 used by Zhang in previous laboratory studies [5, 6, 8] and at least one field test [5, 38]. Other recent studies that have used nano-Fe^0 prepared by reductive precipitation with $NaBH_4$ include [9, 12, 34, 39-41].

Nano-sized magnetite (Fe_3O_4) was synthesized by rapid thermal decomposition of solutes (RTDS), a flow through hydrothermal method [42, 43]. Maghemite (Fe_2O_3) was purchased from Nanophase Corp. (NanoTek, Romeoville, IL, Catalog no. Fe-0800-007-025). The micro-sized electrolytic Fe^0 powder (Fe^{EL}) was from Fisher (Pittsburgh, PA, 99%, Catalog no. I60-3). Nano iron powders were not sieved or polished before use. Some experiments were performed with nano iron powders that were "flash-dried" by rinsing with acetone/water during suction filtration (as described previously [44]), because preliminary experiments suggested that this process can facilitate sample handling and increase reproducibility without significantly altering the reactivity of the particles. Except where noted otherwise, all handling of these materials was done under anoxic conditions (e.g., in an anoxic chamber containing 5% H_2 in N_2). The Fe^{EL} was seived with a 200 mesh seive, and the fines were discarded. The remaining iron powder

(100-200 mesh) was then washed with water, ultrasonicated for 15 min until the supernatant water showed no color or turbidity (3 times was always sufficient), and then flash dried. The resulting material was stored under anoxic conditions.

Transmission Electron Microscopy (TEM). High-resolution TEM was performed using either a Jeol JEM 2010F operated at 200 kV or a Tecnai 12ST (Cs of 2 mm) operated at 120 kV. All images were digitally recorded using slow scan 1024 x 1024 CCD cameras and processed using Digital Micrograph (Gatan). Pre-reaction samples were mounted on carbon-coated TEM grids in an anaerobic chamber but were exposed to air briefly during transfer from the anaerobic chamber to the microscope. Prior to insertion into the microscope, post-reaction samples were mounted on carbon-coated TEM grids inside an anaerobic glove bag.

X-ray Photoelectron Spectroscopy (XPS). Samples for XPS were mounted on double-sided adhesive tape in an anaerobic chamber and transferred into the instrument without exposure to air via a N_2-purged glove bag attached to the sample entry system. The XPS measurements were performed using a Physical Electronics Quantum 2000 Scanning ESCA Microprobe with a focused monochromatic Al Kα X-ray (1486.7 eV) source for excitation, a spherical section analyzer, and a 16-element multichannel detection system. The X-ray beam was 105 W with a 100 μm spot rastered over a 1.4 mm x 0.2 mm rectangle on the sample surface. The X-ray beam was incident normal to the sample and the X-ray photoelectron detector was at 45° off normal. Data were collected using a pass energy of 23.5 eV. For the Ag 3d5/2 line, these conditions produced a full width at half maximum (FWHM) of 0.77 eV. The binding energy scale was calibrated using the Cu 2p3/2 feature at 932.62 ± 0.05 eV and Au 4f at 83.96 ± 0.05 eV for known standards. 1 eV, 20 uA electrons and low energy Ar^+ ions were used to minimize charging.

X-Ray Diffraction (XRD). Specimens were prepared for XRD analysis by spreading ~25 mg of Fe^{H2} or Fe^{BH} on a zero-background slide and allowing it to dry for 2-3 days in an anaerobic chamber that was constantly purged with N_2. The dried

specimens were protected from oxygen by applying a few drops of 10% glycerol in 95% ethanol, and allowed to dry for 1-2 more days. The glycerol-coated specimens were then analyzed in ambient air with Cu-K_α radiation using a Philips X'Pert MPD diffractometer (PW3040/00) operated at 40 KVP and 50 mA. Continuous scans from 2-75 °2θ were collected at a scan rate of about 2.4 °2 θ min^{-1}. Successive scans, as well as scans taken after 24 h of exposure to ambient air, showed no change in the structural properties of the glycerol-coated specimens, verifying the protective effect of the glycerol film with respect to oxidation. The mean crystallite dimension was estimated using the Scherrer equation, after correction for instrumental broadening.

Scanning Transmission X-ray Microscopy (STXM). X-ray absorption measurements were done at the Advance Light Source (Lawrence Berkeley National Laboratory) on beam line 11.0.2. For end station and beam line details see: http://www-als.lbl.gov/als/microscopes/ scope11.0.2.html. All samples were prepared inside an anaerobic chamber (<0.1 ppm O_2) by dipping carbon-coated TEM grids into dried powder samples and mounting the grids onto aluminum sample holders. Transfer of these holders into the microscope resulted in short (<30 s) exposure of the sample to air. Details regarding the methods used for data acquisition and analysis have been described previously [45].

Surface Area by Gas Adsorption. BET (Brunauer-Emmett-Teller) surface areas were determined from N_2 physisorption with an RXM-100 advanced catalyst characterization system (ASDI, Inc), using the BJH (Barrett-Joyner-Halenda) and multi-point BET methods. Samples were loaded in a anaerobic chamber and evacuated at specified temperatures between 50 C and 150 C for 4 hr before each measurement.

Electrochemical Experiments. Powder disk electrodes (PDEs) were prepared by pressing the powders into the electrode cavity (this compression was sufficient to hold most Fe powders in the cavity). Details of the design and application of these electrodes, including extensive validation and analysis of their response with Fe^{EL}, has been reported previously [46]. In this study, we used only high purity iron as the underlying disk

material, in order to avoid any possibility of galvanic processes. Electrode potentials and currents were recorded with a potentiostat (Autolab PGSTAT30, EcoChemie, Utrecht, The Netherlands). Electrochemical experiments were performed using the methods, solutions, and electrodes described above, in various permutations. All potentials are reported relative to a Ag/AgCl reference, and currents are reported in accord with IUPAC convention (anodic currents are positive and cathodic currents are negative). All polarization experiments were done at a scan rate of 0.1 mV/s, which should give approximately steady-state conditions at the working electrode [47].

Batch Experiments (Benzoquinone). Benzoquinone (BQ) batch experiments were performed in an anaerobic chamber with a 3.4% H_2 in N_2 atmosphere. Particle samples (flash-dried Fe^{BH}, flash-dried Fe^{H2}, and as-received Fe^{EL}) were weighed into 40-mL amber reaction vials and suspended in 20.0 mL of deoxygenated, deionized water. After $\geq$ 4 hr exposure, 5.0 mL of BQ stock solution was added to each of the reaction vials (final concentration = 0.2-2 mM). The vials were sealed and removed from the anaerobic chamber and placed on a shaker table (200 rpm). Periodically, vials were moved back into the anaerobic chamber and sampled for analysis by high-performance liquid chromatography (HPLC). HPLC was done with a Sorbax C18 StableBond column (at 30 °C), 40 mM aqueous acetate buffer (pH 5) and ~35% acetonitrile, with a UV-absorbance detector at λ = 235 nm.

Batch Experiments (Carbon Tetrachloride). Three complementary procedures were used for the batch experiments with carbon tetrachloride (CT). The first was optimized for routine determination of CT disappearance kinetics and the yield of chloroform (CF); the second gave full time-series data on all products, and therefore mass balance, but was only done for a few samples of Fe^0; and the third gave the yield of all products and mass balance readily but without the time-series data needed for full kinetic analysis.

For the first and second procedures, experiments were performed in well-mixed, 120-mL, zero-headspace reactors. Target quantities of Fe^0 (3.00 g Fe^{EL}, 0.15 or 0.30 g

Fe^{H2}, and 0.15 or 0.30 g Fe^{BH}) were selected to give roughly equal surface areas (~6 m^2 L^{-1}). The Fe^0 was exposed to deoxygenated, deionized water or buffer for 24 hours, and then CT-saturated deoxygenated water was added to give an initial CT concentration (C_0) of 4.0 μM for the first procedure and 862 μM for the second procedure. During reaction, vials were covered with foil to exclude light, and they were mixed on a rotary shaker at 24 rpm at room temperature (~22°C). Samples were taken periodically and analyzed for CT, CF, $HCOO^-$, and Cl^-. Controls were prepared without Fe^0 (for leakage of CT or volatile products) and without CT (for leaching of $HCOO^-$ or Cl^-). Concentrations of CT and CF were measured by gas chromatography with a headspace autosampler, DB-624 column, and electron capture detector. Chloride was analyzed using ion chromatography, using an Allsep Anion A2 column with carbonate-based eluant. Formate was analyzed with an assay based on photoluminescence, as described elsewhere [48]. Methane and carbon monoxide were detected by headspace analysis using gas chromatography with thermal conductivity detection with a GS-GASPRO capillary column operated at -80^0 C.

For the third procedure, experiments were performed in 12-mL headspace reactors. Target quantities of each sample (10 mg) were exposed to deoxygenated deionized water overnight. Then, CT-saturated deoxygenated water was added (giving initial concentrations of 2.4 mM CT and 0.2 g L^{-1} Fe^0), the vials were crimp-sealed with Teflon-lined septa, and the sealed vials were gently agitated in the dark using a mechanical shaker until analysis. Concentrations of chlorinated methane species were analyzed by gas chromatography with a DB-1 column and a mass spectrometric detector. Analysis for non-chlorinated gas species was performed with gas chromatography using thermal conductivity detection (TCD).

3.2.4. Results and Discussion

Structure and Composition. Particle shape, size, and composition are important properties that affect the chemical and physical properties of nanoparticles. To provide primary characterization of these properties, XRD, TEM, and XPS measurements were made on specimens of Fe^{H2} and Fe^{BH}, as received and after flash-drying. In addition,

STXM and BET measurements were made on selected samples. The results of these analyses are summarized in Table 3.2.

XRD on the as-received Fe^{H2} showed two phases, α-Fe^0 and Fe_3O_4, with the proportion of metal and oxide ranging from 70 to 30% metal (and 30 to 70% oxide). The proportions of α-Fe^0 and Fe_3O_4 agree well with the manufacturer's description of this product [35]. The mean crystallite dimension (from the Scherrer equation) for the metal grains was ~30 nm while that for the oxide was ~60 nm. In contrast, Fe^{BH} yielded very broad peaks for α-Fe^0 with mean crystallite dimensions <1.5 nm. The non-Lorentzian shape of these peaks (Supporting Information, Figure S1) suggests a distribution of crystallite dimensions. In addition to the much smaller crystallite size, the XRD patterns for Fe^{BH} differ from those for Fe^{H2} by having no reflections for oxide phases. Flash-drying had essentially no effect on the XRD patterns for both Fe^{H2} and Fe^{BH}.

The TEM data (Figure 3.8A) show that as-received Fe^{H2} is composed of aggregates of faceted plates and smaller irregular particles. The plates—which appear to be oxide—are usually larger than the particles and vary in size and quantity. The small irregularly shaped particles consist of a nearly single crystal Fe^0 core with a polycrystalline oxide shell, as shown in Figures 3.8B and C. Flash-dried Fe^{H2} is similar, except that more large oxide plates are shown in Figure 3.8D (however, this difference could be due to sampling bias).

The TEM images of the three batchs of Fe^{BH} appear similar to one another (Figure 3.9). The material is comprised of <1.5 nm crystals that are aggregated into approximately spherical 20-100 nm diameter particles, and these particles are further aggregated into the chains shown in Figure 3.9A. Electron diffraction from the particle cores indicates that the cores are made up of either very small grains or are amorphous. For several particles, however, small discrete spots are visible on the diffraction patterns, which indicate crystalline material (Figures 3.9B and 3.9C). Dark-field imaging (Figure 3.9C) of these particles clearly reveals crystallites that are only a few nanometers in size. This is consistent with the average crystallite size of <1.5 nm measured from diffraction

peak broadening in the XRD data. The spherical particles appear to be coated with a shell of apparently amorphous material, which partially decomposed after 1 min under the 200 V electron beam of the TEM (Supporting Information, Figure S2). Flash-dried Fe^{BH} is similar to as-received Fe^{BH}, except for variations in the distribution of the material coating the particles (Figures 3.9D and 3.9E).

The TEM images were used to determine particle size (Supporting Information, Figure S3), from which specific surface areas (ρ_a, $m^2\ g^{-1}$) were calculated assuming that the particles have spherical geometry and density equal to that of Fe^0 (9.49 g cm^{-3}). For Fe^{H2}, the average particle size was 38 nm as received and 45 nm after flash-drying. Calculating ρ_a for each particle and averaging gives 25 and 30 $m^2\ g^{-1}$, respectively. However, because the particle size distributions are skewed by a small number of large particles (they appear to be log-normally distributed, Figure S3), smaller estimates of ρ_a (11 and 3.5 $m^2\ g^{-1}$, respectively) are obtained by dividing the total surface area of the particles by their (calculated) mass. This procedure is comparable to the property that is measured by BET gas adsorption, and the value of ρ_a calculated from total surface area agrees well with the value we measured for flash-dried Fe^{H2} by BET (3 $m^2\ g^{-1}$). The calculated values of ρ_a are inversely proportional to the assumed density of the particles, so using the average density of magnetite and Fe^0 ($\approx$ 6.7 g cm^{-3}) would increase the estimated values of ρ_a by 14%. Overall, our values are consistent with the low end of the range of BET-determined ρ_a values given by the manufacturer of Fe^{H2} (4-60 $m^2\ g^{-1}$, [35]).

For Fe^{BH}, the TEM data gave average particles sizes of 59 nm and 67 nm, for the as-received and flash-dried samples, respectively (Figure S3). Calculating ρ_a for each measured particle and averaging gives 19 and 14 $m^2\ g^{-1}$; whereas, dividing the total surface area of the particles by their mass gives ρ_a = 7 and 8.5 $m^2\ g^{-1}$. The latter value agrees well with the value of ρ_a that we measured for flash-dried Fe^{BH} by BET gas adsorption (5 $m^2\ g^{-1}$). Even if a particle density closer to that of magnetite is assumed in the calculations, our estimates of ρ_a for Fe^{BH} are lower than the BET-determined values that have been reported previously for this material (33.5-35 $m^2\ g^{-1}$ [5, 8]).

XPS showed that the Fe^{H2} surfaces are made up of mostly Fe and O with small amounts of S, Na, and Ca (Table 3.3). The presence of sulfur is expected due to the use of $FeSO_4$ as a precursor in the synthesis of this product, and the manufacturer claims that reduced S plays an important role its reactivity [35]. The Fe/O ratio observed by XPS varied from 0.72 to 1.15, which is consistent with a mixture of metallic iron and iron oxide (c.f., the Fe/O ratio for Fe_2O_3, which would be □0.67). In contrast to the composition of Fe^{H2}, Fe^{BH} contains significantly less Fe and S, more B, and the Fe/O ratio varies from 0.4 to 0.55. The relative amounts of Fe, O, B and Na appear to be consistent with the presence of a metal core, a thin iron oxide layer, and an outer layer that is predominantly a sodium borate phase. The XPS spectra of the as-received samples of Fe^{BH} suggest mostly oxidized B (borate) with some reduced B (boride), as might be expected based on previous work showing that iron borides can be formed from reduction of aqueous Fe^{2+} with borohydride [49]. In the air-exposed and flash-dried samples, the surface contained less Na than B, but the data are still consistent with a borate component in the shell. Most of the B we see is located in the surface layer of the particles, as has been observed previously [50]; however, others have described Fe^{BH} type particles as doped with B [9], and our measurements do not exclude that possibility.

The Fe 2p XPS data give Fe^0 and Fe-oxide peaks for Fe^{H2} and Fe^{BH} (Supporting Information, Fig S4). We have not attempted to quantify the ratios of Fe^{+2} and Fe^{+3} from these spectra, but it is evident from the data presented in Table 3.3 that the ratio of Fe^0 to oxide signal varies with the sample type and history. Because XPS is sensitive to the outer 3-5 nm of the particles, the presence of a peak for Fe^0 confirms that the shell is less than a few nanometers thick. Exposure of the nanoparticles to air caused the Fe^0 peak in the XPS spectra to decrease or disappear. Flash-drying decreased the Fe^0 to oxide signal strength, but Fe^0 was always present. It may prove to be significant that the S on the Fe^{BH} is in an oxidized form while the S on the Fe^{H2} appears to be in a reduced form.

STXM was used to measure the L-edge X-ray absorption near edge structure (XANES) to give spatially resolved chemical state information on the Fe absorbers in the

samples. The spectral information obtained by this method is particularly sensitive to oxidation states, because of the strong dipole-allowed L-edge 2p→3d electronic transition. The XANES data (Supporting Information, Figure S5) show that Fe^{BH} is similar to the Fe^0 standard, with little oxide peak area (which would appear at slightly higher energy), whereas the XANES for Fe^{H2} has broader peaks that suggest iron oxide as well as Fe^0. In addition, the area-to-area variation of the XANES was greater for Fe^{H2} than for Fe^{BH}, which is consistent with the XRD and TEM data (Table 3.2), confirming that there are separate metal and oxide iron phases in the Fe^{H2} material.

Electrochemical Properties. During preliminary testing of the reproducibility of anodic polarization voltammograms obtained with our powder disk electrodes (PDEs), we found that Fe^{H2} that had been allowed to dry under our glovebox atmosphere gave currents that declined steadily over a period of 14 days (Figure S6). However, flash-dried Fe^{H2} gave anodic polarization voltammograms that were reproducible over 20 days (Figure S7), so all further electrochemical characterizations were performed with PDEs made from flash-dried powders. Even with flash-dried Fe^{H2}, consecutive voltammograms obtained with the same PDE showed a decreasing current response. To determine if this behavior is due to passivation by reaction with the electrolyte or potential driven transformation of the electrode material, we exposed the PDE packed with Fe^{H2} to borate solution (pH = 8.4) for various amounts of time before recording the anodic polarization voltammogram. After one hour of exposure in borate, the current response decreased, indicating that the loss of electrochemical response was due to solution driven passivation (Figure S8). Since solution driven passivation cannot be overcome in our system, all further polarization experiments were initiated immediately after the electrode was put in solution

All of the above experiments provide a baseline from which we can interpret and compare the electrochemical results of the nano-Fe^0 materials. Figure 3.10 shows the anodic polarization voltammograms obtained with PDEs of the nano-Fe^0 materials, several powder iron oxides, and Fe^{EL}. For reference, data obtained with a polished disk

Fe^0 electrode are also included in the figure. As expected, the conventional Fe^0 disk electrode and Fe^{EL} PDE gave anodic polarization voltammograms that reflect the transition from the active to passive state of iron as the potential becomes more anodic, which is typical for Fe^0 in borate buffer [51-54]. A prominent feature of the log current vs. potential plot for these electrodes is the singularities where net current is zero, i.e., the corrosion potential (E_{corr}). The conventional Fe^0 disk and the Fe^{EL} PDE give E_{corr}'s that are very similar to each other and also to the literature value for Fe^0 in borate [51-54]. The anodic polarization voltammograms for Fe_3O_4 and Fe_2O_3 PDE's give E_{corr}'s more anodic than the Fe^0 disk and Fe^{EL} PDE. This is not surprising, given that Fe_3O_4 is a mixed oxide containing Fe^{2+} and Fe^{3+} and Fe_2O_3 contains only Fe^{3+}. Thus, it appears that our experimental design is sensitive to the oxidation state of the iron used in the fabrication of the working electrode in that the material with the most oxidized iron gives the most anodic E_{corr} relative to Fe^0 and Fe^{EL}.

Figure 3.10 also shows two sets of anodic polarization voltammograms for the two nano-Fe^0 materials (Fe^{H2} and Fe^{BH}). The solid lines represent Fe^{H2} and Fe^{BH} after they were dried in the anaerobic chamber. The most striking difference is that the E_{corr}'s for both materials are shifted cathodically relative to the E_{corr} of Fe^0 and Fe^{EL} and that the E_{corr}'s for the nano materials are very similar to one another. Recall, from experiments mentioned above that Fe^{H2} dried in the anaerobic chamber gave decreasing current response, and therefore, more stable and representative results are expected with flash-dried material. The E_{corr}'s for flash-dried Fe^{H2} and Fe^{BH} are shifted even more cathodically relative to the Fe^0 and Fe^{EL} electrodes (Figure 3.10). The shift in E_{corr} must reflect disproportionate changes in the kinetics of the coupled half-reactions that determine E_{corr} in this system: anodic dissolution of Fe^0 and the reduction of water. Exactly how electrode material (i.e., conventional Fe^0 disk vs. our nano-Fe^0 PDE) affects the kinetics of these half-reactions is still under investigation, but it is likely to involve the high surface areas of the nano-Fe^0 powders, which often have large surface concentrations of edges, corners, and other defect sites.

Batch Results. Two model contaminants were used as probe compounds to investigate the reactivity of nano-Fe^0 with solutes: benzoquinone (BQ) and carbon tetrachloride (CT). BQ was chosen because it is a well established probe for the reactivity of iron oxides [55, 56], and CT has been used in many detailed studies of the reactivity of iron and iron oxides [e.g., 57, 58-64]. BQ is likely to form comparatively strong inner-sphere complexes on iron and iron oxides (at pH > 7, as is relevant to this study [56]), whereas CT is believed to form weak and outer-sphere complexes with oxide-coated iron [65]. BQ is labile to reduction by electron transfer (ET) and hydrogen atom transfer (HT), and both pathways will produce mainly hydroquinone (HQ). In contrast, while CT is believed to react mainly by ET in systems containing Fe^0 [66, 67], branching among two pathways of ET produces diagnostic products: chloroform (CF) for the "1-electron pathway" and methane, carbon monoxide, or formate for the "2-electron pathway" [61, 68]. Since the latter are the preferred products—from the perspective of remediation—any nano-size effect on branching between these two reaction pathways is of practical, as well as fundamental, interest.

For BQ, pseudo-first-order disappearance rate constants were obtained from the concentration vs. time data (not shown), and the results were used to calculate mass normalized rate constants (k_M, L g^{-1} min^{-1}). Assuming a range of ρ_a for each type of nano-Fe^0, we calculated surface area normalized rate constants (k_{SA}, L m^{-2} min^{-1}) for each value of k_M. The results are summarized in Figure 3.11, which allows comparisons between types of iron, over ranges of ρ_a (note that changes in assumed ρ_a causes points to move vertically on the plot) and variations in experimental conditions for a particular type of iron (initial C_0's, pH, mixing rate, etc., which cause the data to distribute diagonally along the contour for the assumed value of ρ_a). For the whole range of conditions tested, the trend in k_M is $Fe^{EL} < Fe^{H2} < Fe^{BH}$. With respect to k_{SA}, the data in Figure 3.11 show that $Fe^{EL} \approx Fe^{H2} < Fe^{BH}$ for the whole range of plausible values of ρ_a. The greater reactivity of Fe^{BH} (vs. Fe^{H2}) with BQ is consistent with the more metallic composition of Fe^{BH}, but the role of other factors (e.g., the B-rich shell material and very small crystallite

size) is unknown. The products formed from BQ were the same for all three types of iron: HQ was the only identified product, and it gave mass balance with respect to the amount of BQ reacted.

Figure S9 shows TEM micrographs of flash-dried Fe^{BH} (A and B) and Fe^{H2} (C and D) after reaction with BQ. The lower magnification images (A and C) demonstrate that some particles appear unaltered even after substantial reaction with BQ (c.f., Figures 3.8-3.9). Of particular note is that the thickness of the coating on the Fe^{BH} particles appears similar to what was observed before reaction, and none of the unreacted particles show "disrupted" shells. It is likely that the microstructure of the B-rich shell material plays a key role in the relative reactivity of Fe^{BH}. Higher-resolution images (Fig. S9, B and D) demonstrate that the solid-state reaction products are nanocrystalline and appear to be well separated from the parent particles, which suggests that the products are formed by oxidative dissolution followed by precipitation. Lattice fringe measurements and diffraction patterns show that the main product is maghemite/magnetite (with some goethite, in the case of Fe^{BH}).

The kinetic data obtained with CT show somewhat different trends than were obtained with BQ. Figure 3.12 shows k_{SA} vs. k_M for CT, calculated with the same ranges of ρ_a that were used for Figure 3.11. Clearly, k_M for reduction of CT is larger with nano-Fe^0 than micro-Fe^0 ($Fe^{EL} < Fe^{H2} \approx Fe^{BH}$). The relative values of k_{SA} vary, however, depending on the assumed values of ρ_a. For high ρ_a, it appears that $Fe^{EL} > Fe^{H2} \approx Fe^{BH}$; but for low ρ_a, $Fe^{EL} \approx Fe^{H2} \approx Fe^{BH}$. Thus, given the difficulties in determining accurate (and relevant) values of ρ_a for nano-Fe^0, it is unclear whether there is a nano-size effect on the surface area normalized rate constants for reduction of CT. This conclusion holds over the whole range of experimental conditions tested (initial CT concentration, buffer type, pH, and sample handling), the effects of which are represented by the range of data along the contours in Figure 3.12. The conclusion that nano-Fe^0 may not be more reactive than micro-Fe^0 on a surface area normalized basis does not necessarily contradict prior claims that nano-Fe^0 is more reactive than micro-Fe^0 on a per mass basis. It does, however, demonstrate the importance of clearly defining the basis of comparison. Of

course, if mass transport (across the stagnant boundary layer or some passivating surface layer) were rate limiting under the conditions of the batch experiments performed in this study, this could mask differences in the intrinsic reactivity of surface sites. We do not think mass transport effects are significant in this study because we observed no change in k_{SA} with rpm > 15 (data not shown); however, subtle mass transport effects might be revealed by further study with more sensitive methods [63, 69].

Figure 3.13 shows the yield of CF (Y_{CF})—one measure of the branching between the one- and two-electron pathways for reduction of CT—for the same experiments included in Figure 3.12. In general, the values of Y_{CF} are > 0.4 for Fe^{EL} and Fe^{BH} but are < 0.4 for Fe^{H2}. It is not yet clear why Fe^{H2} gives such a low, and favorable, Y_{CF}, but this result is likely to be due to (*i*) the Fe_3O_4 shell on Fe^{H2}, (*ii*) the reduced S on the surface of Fe^{H2}, and/or (*iii*) the B associated with Fe^{BH}. The first possibility is supported by the low values of Y_{CF} that have been reported for suspensions of nano-sized Fe_3O_4 [61]. Previous studies of CT reduction by FeS [70], showed that CF was a major product, with CS_2 being a notable minor product, neither of which were observed in this study with Fe^{H2}. In Figure 3.13, as in Figure 3.12, the range of results for each type of Fe^0 reflects the effects of buffer type, pH, and sample handling, which helps to establish the significance of the difference between Y_{CF} for Fe^{H2} relative to the two other types of Fe^0.

To determine what products other than CF were formed, it was necessary to perform batch experiments at high initial CT concentration (0.86-2.4 mM) with a variety of analytical methods, as appropriate for the range of anticipated products. Typical results from headspace GC/MS, shown in Table 3.4, suggest that CF was the major product for Fe^{H2} and Fe^{BH}, CH_2Cl_2 is a minor product, and a significant portion of the CT reacted to undetermined products. Although not reflected in Table 3.4, GC/TCD analysis of these samples also showed trace quantities of CH_4 (<0.1% by volume) in the Fe^{BH} samples, whereas no CH_4 was detected in the Fe^{H2} samples. No CS_2, CO_2 or CO was detected in the headspace products of either material. Little difference was noted between the as-received and flash-dried samples. In other experiments (not shown), small amounts of formate (1-5 μM at C_0 = 4 μM, 5-11 μM at C_0 = 862 μM) were detected, but these

quantities are not enough to close the mass balance for CT degraded. Recall that formate is produced through the "2-electron" pathway. This data indicates that at low C_0's, the "2-electron" pathway may be favored over the "1-electron" pathway. We are still left with a large fraction of carbon that has not been detected, however, and further studies are on-going to determine all of the products formed under these experimental conditions.

3.2.5. Implications.

Data from this paper demonstrate that the two types of nano-Fe^0 used in this study are composed of particles with a core/shell structure, and that the shells are composed of passivating or protective phases that impart stability to the particles in aqueous suspensions. For Fe^{H2}, the shell is mainly iron oxide, whereas for Fe^{BH} the shell is composed of iron and boron oxides. Flash-drying these materials—to remove water and solutes—generally had little effect on the properties studied, again suggesting passivation of the particles.

Despite their stability with respect to aqueous corrosion and other solvent-driven dissolution processes, both types of nano-Fe^0 react rapidly with BQ and CT. Although the rate constants for these reactions are large when normalized to iron mass, the surface area normalized rate constants are similar for nano- and micro-sized Fe^0. The apparent lack of an "intrinsic" nano-size effect may reflect the difficulty in defining or measuring the (relevant) specific surface area for highly reactive materials whose properties change with time and environmental conditions. Nevertheless, our results suggest that the extraordinarily high contaminant degradation rates that have often been ascribed to nano-Fe^0 are mostly due to the large amount of surface area used in laboratory tests with these materials. In contrast, it appears that nano-Fe^0 can have a profound effect on the distribution of products formed from contaminant degradation. In particular, the low yield of chloroform from carbon tetrachloride that was obtained with Fe^{H2} suggests the possibility of an effective new chemical technology for remediation of carbon tetrachloride contaminated groundwater.

3.2.6. Acknowledgments

Samples of nano iron were donated by C. Clausen (University of Central Florida), K. Okinaka (Toda Kogyo Corp.), and W.-X. Zhang (Lehigh University). This work was supported by the U.S. Department of Energy (DOE) Environmental Management Sciences Program and the Office of Energy Research, Office of Basic Energy Sciences, Chemical Sciences Division. Parts of the work were conducted in the William R. Wiley Environmental Molecular Sciences Laboratory (EMSL) and the Advanced Light Source (ALS). We thank EMSL staff Mark Engelhard, David McCready, and Cathy Chin for assistance with the XPS, XRD, and BET analysis, respectively. EMSL is a DOE User Facility operated by Battelle for the DOE Office of Biological and Environmental Research. The Pacific Northwest National Laboratory is operated for the DOE under Contract DE-AC06-76RLO 1830. The ALS is supported by DOE Contract No. DE-AC03-76SF00098 to Lawrence Berkeley National Laboratory.

3.2.7. References

[1] Tratnyek, P. G.; Scherer, M. M.; Johnson, T. J.; Matheson, L. J. In *Chemical Degradation Methods for Wastes and Pollutants: Environmental and Industrial Applications*; Tarr, M. A., Ed.; Marcel Dekker: New York, 2003; pp 371-421.

[2] Glazier, R.; Venkatakrishnan, R.; Gheorghiu, F.; Walata, L.; Nash, R.; Zhang, W.-X. Nanotechnology takes root *Civil Engineering* **2003**, *73*, 64-69.

[3] Elliott, D. W.; Zhang, W.-X. Field assessment of nanoscale bimetallic particles for groundwater treatment *Environ. Sci. Technol.* **2002**, *35*, 4922-4926.

[4] Geiger, C.; Clausen, C. A.; Brooks, K.; Clausen, C.; Huntley, C.; Filipek, L. B.; Reinhart, D. D.; Quinn, J.; Krug, T.; O'Hara, S.; Major, D. In *Chlorinated Solvent and DNAPL Remediation: Innovative Strategies for Subsurface Cleanup*; Henry, S. M., Warner, S. D., Eds.; American Chemical Society: Washington, DC, 2003; Vol. ACS Symp. Ser. 837, pp 132-140.

[5] Wang, C.-B.; Zhang, W.-X. Synthesizing nanoscale iron particles for rapid and complete dechlorination of TCE and PCBs *Environ. Sci. Technol.* **1997**, *31*, 2154-2156.

[6] Lien, H.-L.; Zhang, W.-X. Transformation of chlorinated methanes by nanoscale iron particles *J. Environ. Eng.* **1999**, *125*, 1042-1047.

[7] Xu, Y.; Zhang, W. X. Subcolloidal Fe/Ag particles for reductive dehalogenation of chlorinated benzenes *Ind. Eng. Chem. Res.* **2000**, *39*, 2238-2244.

[8] Lien, H.-L.; Zhang, W.-X. Nanoscale iron particles for complete reduction of chlorinated ethenes *Colloid Surf. A-Physicochem. Eng. Asp.* **2001**, *191*, 97-105.

[9] Lowry, G. V.; Majetich, S.; Sholl, D.; Tilton, R. D.; Matyjaszewski, K.; Liu, Y.; Sarbu, T.; Almusallam, A.; Redden, G. D.; Meakin, P.; Rollins, H. W. In *227th National Meeting, 28 March - 1 April 2004*; American Chemical Society: Anaheim, CA, 2004; Vol. 44, No. 1, pp 488-493.

[10] Lowry, G. V.; Reinhard, M. Pd-catalyzed TCE dechlorination in groundwater: solute effects, biological control, and oxidative catalyst regeneration *Environ. Sci. Technol.* **2000**, *34*, 3217-3223.

[11] Choe, S.; Chang, Y. Y.; Hwang, K. Y.; Khim, J. Kinetics of reductive denitrification by nanoscale zero-valent iron *Chemosphere* **2000**, *41*, 1307-1311.

[12] Ponder, S. M.; Darab, J. G.; Mallouk, T. E. Remediation of Cr(VI) and Pb(II) aqueous solutions using supported, nanoscale zero-valent iron *Environ. Sci. Technol.* **2000**, *34*, 2564-2569.

[13] Li, F.; Vipulanandan, C.; Mohanty, K. K. Microemulsion and solution approaches to nanoparticle iron production for degradation of trichloroethylene *Colloid Surf. A-Physicochem. Eng. Asp.* **2003**, *223*, 103-112.

[14] Zhang, W. Nanoscale iron particles for environmental remediation *J. Nanoparticle Res.* **2003**, *5*, 323-332.

[15] Johnson, T. L.; Scherer, M. M.; Tratnyek, P. G. Kinetics of halogenated organic compound degradation by iron metal *Environ. Sci. Technol.* **1996**, *30*, 2634-2640.

[16] Klabunde, K. J.; Stark, J.; Koper, O.; Mohs, C.; Park, D. G.; Decker, S.; Jiang, Y.; Lagadic, I.; Zhang, D. J. Nanocrystals as stoichiometric reagents with unique surface chemistry *J. Phys. Chem.* **1996**, *100*, 12142-12153.

[17] Mulvaney, P. In *Nanoscale Materials in Chemistry*; Klabunde, K. J., Ed.; Wiley: New York, 2001; pp 121-167.

[18] Campbell, C. T.; Parker, S. C. The effect of size-dependent nanoparticle energetics on catalyst sintering. *Science* **2002**, *298*, 811-814.

[19] Elliott, S. *The Physics and Chemistry of Solids*; Wiley & Sons: New York, 1998.

[20] Brus, L. Electronic wave functions in semiconductor clusters: experiment and theory *J. Phys. Chem.* **1986**, *90*, 2555-2560.

[21] Wang, Y.; Herron, N. Nanometer-sized semiconductor clusters: material synthesis, quantum size effects, and photophysical properties *J. Phys. Chem.* **1991**, *95*, 525-532.

[22] Klimenkow, M.; Nepijko, S. A.; Kuhlenbeck, H.; Baumer, M.; Schlogl, R.; Fruend, H. J. The structure of Pt-aggregates on a supported thin aluminum oxide film in comparison with unsupported alumina: a transmission electron microscopy study *Surf. Sci.* **1997**, *391*, 27-36.

[23] Nepijko, S. A.; Klimenkow, M.; Kuhlenbeck, H.; Zemlyanov, D.; Herein, D.; Schlogl, R.; Fruend, H. J. TEM study of tantalum clusters of Al_2O_3/NiAl(110) *Surf. Sci.* **1998**, *412/413*, 192-201.

[24] Nepijko, S. A.; Klimenkow, M.; Adelt, M.; Kuhlenbeck, H.; Schlogl, R.; Fruend, H. J. Structural investigation of palladium clusters on γ-AlO_3(111/NiAl(110) with transmission electron microscopy *Langmuir* **1999**, *15*, 5309-5313.

[25] Gan, S.; Liang, Y.; Baer, D. R.; Sievers, M. R.; Herman, G. S.; Peden, C. H. F. Effect of platinum nanocluster size and titania surface structure upon CO surface chemistry on platinum-support on TiO2(110) *J. Phys. Chem. B* **2001**, *105*, 2412-2415.

[26] Baer, D. R.; Burrows, P. E.; El Azab, A. A. Enhancing coating functionality using nanoscience and nanotechnology. *Prog. Org. Coat.* **2003**, *47*, 342-356.

[27] Punoose, A.; Magnone, H.; Seehra, M. S.; Bonevich, J. Bulk to nanoscale magnetism and exchange bias in CuO nanoparticles *Phys. Rev. B* **2001**, *64*, 174420-.

[28] Sharma, R. K.; Sharma, P.; Maitra, A. Size-dependent catalytic behavior of platinum nanoparticles on the hexacyanoferrate(III)/thiosulfate redox reaction *J. Colloid Interfac. Sci.* **2003**, *265*, 134-140.

[29] Signorini, L.; Pasquini, L.; Savini, L.; Carboni, R.; Boscherini, F.; Bonetti, E.; Giglia, A.; Pedio, M.; Mahne, N.; Nannarone, S. Size-dependent oxidation in iron/iron oxide core-shell nanoparticles *Phys. Rev. B* **2003**, *68*, 195423.

[30] Theil Kuhn, L.; Bojesen, A.; Timmermann, L.; Meedom Nielsen, M.; Morup, S. Structural and magnetic properties of core-shell iron-iron oxide nanoparticles *J. Phys.: Condens. Matter* **2002**, *14*, 13551-13567.

[31] Scherer, M. M.; Balko, B. A.; Tratnyek, P. G. In *Mineral-Water Interfacial Reactions: Kinetics and Mechanisms*; Sparks, D. L., Grundl, T. J., Eds.; American Chemical Society: Washington, DC, 1998; Vol. ACS Symp. Ser. 715, pp 301-322.

[32] Zaitsev, V. S.; Filimonov, D. S.; Presnyakov, I. A.; Gambino, R. J.; Chu, B. Physical and chemical properties of magnetite and magnetite-polymer nanoparticles and their colloidal dispersions *J. Colloid Interfac. Sci.* **1999**, *212*, 49-57.

[33] Wang, Y.; Wong, J. F.; Teng, X.; Lin, X. Z.; Yang, H. "Pulling" nanoparticles into water: Phase transfer of oleic acid stabilized monodisperse nanoparticles into aqueous solutions of α-cyclodextrin *Nano Letters* **2003**, *3*, 1555-1559.

[34] Schrick, B.; Hydutsky, B. W.; Blough, J. L.; Mallouk, T. E. Delivery vehicles for zerovalent metal nanoparticles in soil and groundwater *Chem. Mat.* **2004**, *16*, 2187-2193.

[35] Uegami, M.; Kawano, J.; Okita, T.; Fujii, Y.; Okinaka, K.; Kakuya, K.; Yatagai, S. In; Toda Kogyo Corp.: United States, 2003; p 44.

[36] Okinaka, K.; Jazdanian, A. D.; Shimizu, H.; Okita, T.; Kakuya, K. In *Proceedings of the Fourth International Conference on Remediation of Chlorinated and Recalcitrant Compounds, 24-27 May 2004, Monterey, CA*; Battelle Press: Columbus, OH, 2004.

[37] Geiger, C. L.; Clausen, C. A.; Brooks, K.; Coon, C.; Huntley, C.; Filipek, L. B.; Devor, R.; Krug, T.; O'Hara, S.; Major, D.; Quinn, J. In *225th National Meeting, 23-27 March 2003*; American Chemical Society: New Orleans, LA, 2003; Vol. 43, No. 1, pp 939-944.

[38] Lien, H.-L.; Zhang, W.-X. In *215th National Meeting*; American Chemical Society: Dallas, TX, 1998; Vol. 38, No. 1, pp 29-30.

[39] Ponder, S. M.; Darab, J. G.; Bucher, J.; Caulder, D.; Craig, I.; Davis, L.; Edelstein, N.; Lukens, W.; Nitsche, H.; Rao, L.; Shuh, D. K.; Mallouk, T. E. Surface chemistry and electrochemistry of supported zerovalent iron nanoparticles in the remediation of aqueous metal contaminants *Chem. Mat.* **2001**, *13*, 479-486.

[40] Schrick, B.; Blough, J. L.; Jones, A. D.; Mallouk, T. E. Hydrodechlorination of trichloroethylene to hydrocarbons using bimetallic nickel-iron nanoparticles *Chem. Mat.* **2002**, *14*, 5140-5147.

[41] Liu, Y.; Lowry, G. In *228th National Meeting, 22-26 August 2004*; American Chemical Society: Philadelphia, PA, 2004; Vol. 44, No. 2, pp 412-417.

[42] Matson, D. W.; Linehan, J. C.; Darab, J. G.; Buehler, M. F.; Phelps, M. R.; Neuenschwander, G. G. In *Advanced Techniques in Catalyst Preparation*; Moser, W. R., Ed.; Academic: New York, 1996; pp 259-283.

[43] Matson, D. W.; Linehan, J. C.; Darab, J. G.; Buehler, M. F. Nanophase iron-based liquefaction catalysts: synthesis, characterization, and model compound reactivity *Energy Fuels* **1994**, *8*, 10-18.

[44] Miehr, R.; Tratnyek, P. G.; Bandstra, J. Z.; Scherer, M. M.; Alowitz, M.; Bylaska, E. J. The diversity of contaminant reduction reactions by zero-valent iron: role of the reductate *Environ. Sci. Technol.* **2004**, *38*, 139-147.

[45] Pecher, K.; McCubbery, D.; Kneedler, E.; Rothe, J.; Bargar, J.; Meigs, G.; Cox, L.; Nealson, K.; Tonner, B. Quantitative charge analysis of manganese biominerals in aqueous suspension using scanning transmission x-ray microscopy (STXM) *Geochim. Cosmochim. Acta* **2003**, *67*, 1089-1098.

[46] Nurmi, J. T.; Bandstra, J. Z.; Tratnyek, P. G. Packed powder electrodes for characterizing the reactivity of granular iron in borate solutions *J. Electrochem. Soc.* **2004**, *151*, B347-B353.

[47] Drazic, D. M.; Zecevic, S. K. Transient phenomena during the anodic polarization of iron *Corr. Sci.* **1985**, *25*, 209-216.

[48] Vaughan, G. M.; Mopper, K. Determination of nanomolar levels of formate in natural-waters Based on a luminescence enzymatic assay *Anal. Chim. Acta* **1990**, *231*, 299-303.

[49] Glavee, G. N.; Klabunde, K. J.; Sorensen, C. M.; Hadjipanayis, G. C. Chemistry of borohydride reduction of iron(II) and iron(III) ions in aqueous and nonaqueous media - formation of nanoscale Fe, FeB, and Fe_2B powders *Inorg. Chem.* **1995**, *34*, 28-35.

[50] Carpenter, E. E.; Calvin, S.; Stroud, R. M.; Harris, V. G. Passivated iron as core-shell nanoparticles *Chem. Mat.* **2003**, *15*, 3245-3246.

[51] Sato, N. In *Passivity of Metals*; Frankenthal, R. P., Kruger, J., Eds.; Electrochemical Society: Princeton, NJ, 1978; pp 29-58.

[52] Cohen, M. In *Passivity of Metals*; Frankenthal, R. P., Kruger, J., Eds.; Electrochemical Society: Princeton, NJ, 1978; pp 521-545.

[53] Jovancicevic, V.; Kainthla, R. C.; Tang, Z.; Yang, B.; Bockris, J. O. M. The passive film on iron: an ellipsometric-spectroscopic study *Langmuir* **1987**, *3*, 388-395.

[54] Oblonsky, L. J.; Devine, T. M. A surface enhanced Raman spectroscopic study of the passive films formed in borate buffer on iron, nickel, chromium and stainless steel *Corr. Sci.* **1995**, *37*, 17-41.

[55] Stack, A. G.; Eggleston, C. M.; Englehard, M. H. Reaction of hydroquinone with hematite. I. Study of adsorption by electrochemical-scanning tunneling microscopy and X-ray photoelectron spectroscopy *J. Colloid Interfac. Sci.* **2004**, *274*, 433-441.

[56] Kung, K.-H.; McBride, M. B. Electron transfer processes between hydroquinone and hausmannite (Mn_3O_4) *Clays Clay Miner.* **1988**, *36*, 303-309.

[57] Balko, B. A.; Tratnyek, P. G. Photoeffects on the reduction of carbon tetrachloride by zero-valent iron *J. Phys. Chem. B* **1998**, *102*, 1459-1465.

[58] Elsner, M.; Haderlein, S. B.; Kellerhals, T.; Luzi, S.; Zwank, L.; Angst, W.; Schwarzenbach, R. P. Mechanisms and products of surface-mediated reductive dehalogenation of carbon tetrachloride by Fe(II) on goethite *Environ. Sci. Technol.* **2004**, *38*, 2058-2066.

[59] Gaspar, D. J.; Lea, A. S.; Engelhard, M. H.; Baer, D. R.; Miehr, R.; Tratnyek, P. G. Evidence for localization of reaction upon reduction of CCl_4 by granular iron *Langmuir* **2002**, *18*, 7688-7693.

[60] Logue, B. A.; Westall, J. C. Kinetics of reduction of nitrobenzene and carbon tetrachloride at an iron-oxide coated gold electrode *Environ. Sci. Technol.* **2003**, *37*, 2356-2362.

[61] McCormick, M. L.; Adriaens, P. Carbon tetrachloride transformation on the surface of nanoscale biogenic magnetite particles *Environ. Sci. Technol.* **2004**, *38*, 1045-1053.

[62] Pecher, K.; Haderlein, S. B.; Schwarzenbach, R. P. Reduction of polyhalogenated methanes by surface-bound Fe(II) in aqueous suspensions of iron oxides *Environ. Sci. Technol.* **2002**, *36*, 1734-1741.

[63] Scherer, M. M.; Westall, J. C.; Ziomek-Moroz, M.; Tratnyek, P. G. Kinetics of carbon tetrachloride reduction at an oxide-free iron electrode *Environ. Sci. Technol.* **1997**, *31*, 2385-2391.

[64] Támara, M.; Butler, E. C. Effects of iron purity and groundwater characteristics on rates and products in the degradation of carbon tetrachloride by iron metal *Environ. Sci. Technol.* **2004**, *38*, 1866-1876.

[65] Johnson, T. L.; Fish, W.; Gorby, Y. A.; Tratnyek, P. G. Degradation of carbon tetrachloride by iron metal: Complexation effects on the oxide surface *J. Contam. Hydrol.* **1998**, *29*, 377-396.

[66] Scherer, M. M.; Westall, J. C.; Tratnyek, P. G. Discussion on "Electrochemical and Raman spectroscopic studies of the influence of chlorinated solvents on the corrosion behaviour of iron in borate buffer and in simulated groundwater" [*Corrosion Science* 42 (2000) 1921-1939] *Corr. Sci.* **2001**, *44*, 1151-1157.

[67] Li, T.; Farrell, J. Electrochemical investigation of the rate-limiting mechanisms for trichloroethylene and carbon tetrachloride reduction at iron surfaces *Environ. Sci. Technol.* **2001**, *35*, 3560-3565.

[68] Tratnyek, P. G.; Amonette, J. E.; Bylaska, E. J. In *227th National Meeting, 28 March - 1 April 2004*; American Chemical Society: Anaheim, CA, 2004; Vol. 44, No. 1, pp 456-460.

[69] Scherer, M. M.; Johnson, K.; Westall, J. C.; Tratnyek, P. G. Mass transport effects on the kinetics of nitrobenzene reduction by iron metal *Environ. Sci. Technol.* **2001**, *35*, 2804-2811.

[70] Kriegman-King, M. R.; Reinhard, M. Transformation of carbon tetrachloride by pyrite in aqueous solution *Environ. Sci. Technol.* **1994**, *28*, 692-700.

Table 3.1. Supplier Characteristics of Iron Particles.

Name	Source	Method	Particle Size (dia.)	BET Surface Area	Major Phase	Minor Phase
Fe^{H2}	Toda Americas, Inc.	High temp. reduction of oxides with H_2	70 nm	29 m^2/g	α-Fe^0	Magnetite
Fe^{BH}	W.-X. Zhang, Lehigh Univ.	Precip. w/ $NaBH_4$	10-100 nm	33.5 m^2/g	Fe^0	Goethite, Wustite
Fe^{EL}	Fisher Scientific	Electrolytic	150 μm	0.1-1 m^2/g	99% Fe^0	
Fe_3O_4	PNNL	Precip from $FeSO_4$ w/ KOH	30-100 nm	4-24 m^2/g	Fe_3O_4	
Fe_2O_3	Nanotek, Corp.	Physical Vapor Synthesis (PVS)	23 nm	50 m^2/g	γ-Fe_2O_3	

Table 3.2. Summary of Physical Properties.

Name	Sample History	Mean Particle Size from TEM (nm)	Shell Thickness (nm)	TEM Structure	XRD (Grain Size nm)	XPS	STXM
Fe^{H2}	As-received	~38 Fe^0 ≥60 nm oxide plates	Fe-Oxide ~3.4	"large"plates (oxide) and smaller Fe^0 irregularly shaped particles with crystalline oxide shell	Fe^0 (~30) oxide (~60)	Fe^0+Fe^{+3}	Fe^0 + oxide
Fe^{H2}	Flash-dried	~44 Fe^0		As above with more large plates		Less Fe^0	
Fe^{BH}	As-received	~59 (20-100)	~2.3	Three levels of structure: i) small crystallites (<1.5 nm), ii) 20-100 nm spherical aggregates with an amorphous coating, and iii) chains of 20-100 nm particles	Mostly Fe^0 (<1.5)	Fe^0+Fe^{+3} + B and Na	Mostly Fe^0
Fe^{BH}	Flash-dried	~67 (20-100)	~3.2	As above with thicker coating		Less Fe^0 +B and Na	

Table 3.3. Particle Surface Compositions Determined by XPS.

	Fe/O	Fe	O	B	Na	S	Ca
Fe^{H2}							
As-received (Fresh)	1.15	50.9	44.2	0.0	3.0	1.9	0.0
Air-exposed	0.89	45.7	51.5	0.0	1.7	1.1	0.0
As-received (Aged)	0.72	37.9	52.3	0.0	8.1	1.3	0.4
Flash-dried	0.85	45.0	52.9	0.0	0.7	0.9	0.5
Fe^{BH}							
As-received (Fresh)	0.41	20.0	49.1	16.0	14.5	0.5	0.0
Air-exposed	0.40	23.5	59.2	12.0	4.8	0.5	0.0
As-received (Aged)	0.56	29.2	52.4	16.2	2.2	0.0	0.0
Flash-dried	0.55	30.8	56.4	12.3	0.5	0.0	0.0

In atomic %.

Table 3.4. Mass balance data for CT and products.

Particle Prep.	CCl_4	$CHCl_3$	CH_2Cl_2	Unknown
Fe^{H2}				
As-received	54.2	21.7	0.0	24.1
Flash-dried	58.3	18.4	0.0	23.3
Fe^{BH}				
As-received	28.8	34.8	0.7	36.7
Flash-dried	15.8	39.3	2.4	42.5

% of initial CT concentration (2.4 mM) at t = 27 hr.

Figure 3.8 (A-B)

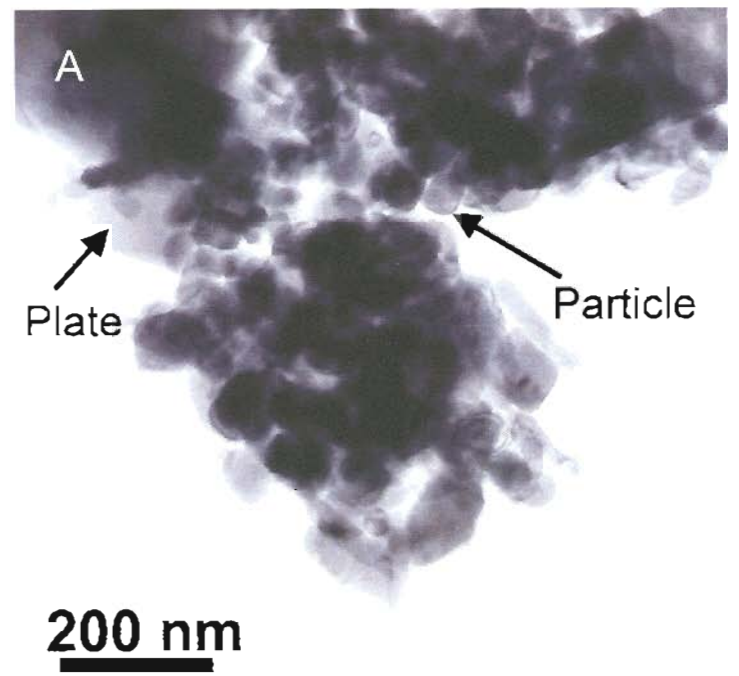

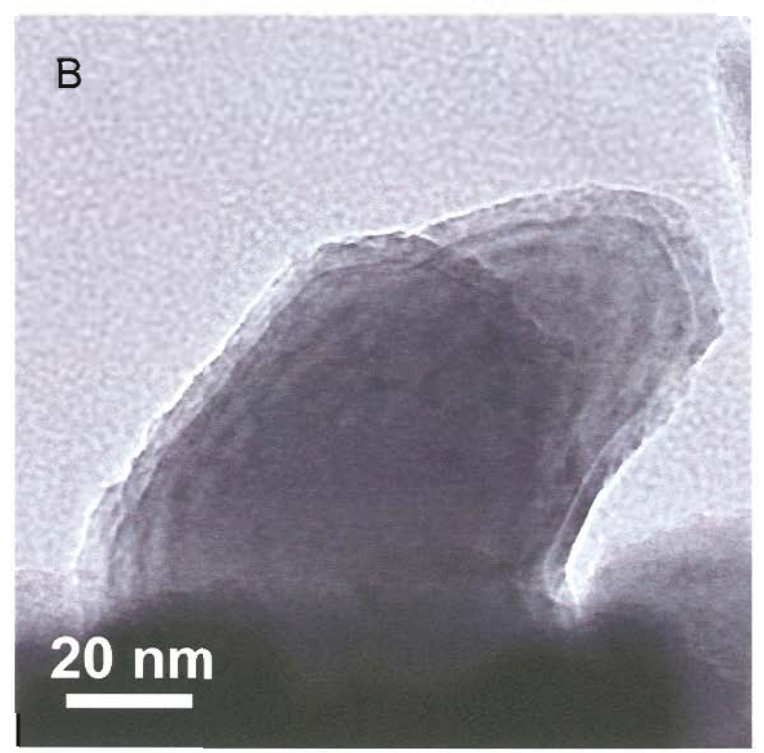

Figure 3.8 (C-D)

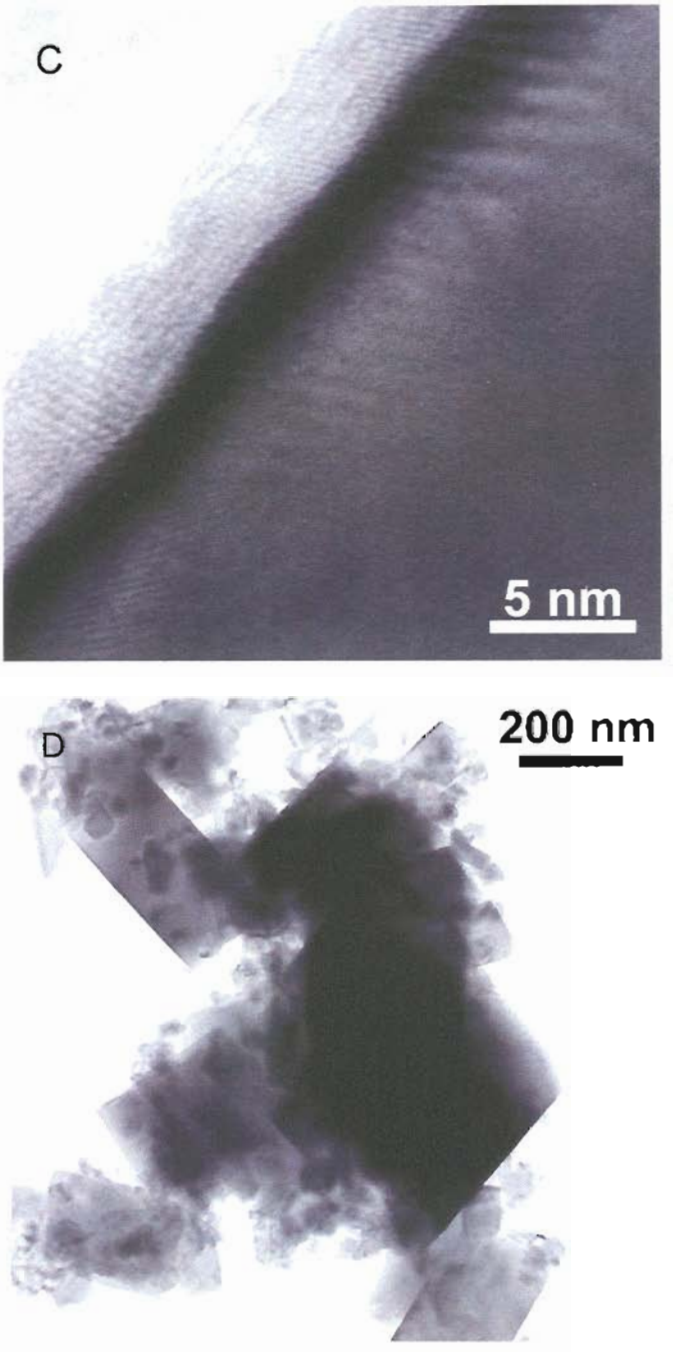

Figure 3.8. TEMs of Fe^{H2}. (A) Low magnification image of as-received sample, (B) Higher resolution of image of irregularly-shaped metal particle, (C) Higher resolution image of oxide shell around metal particle, (D) Low resolution image of flash-dried sample.

Figure 3.9 (A)

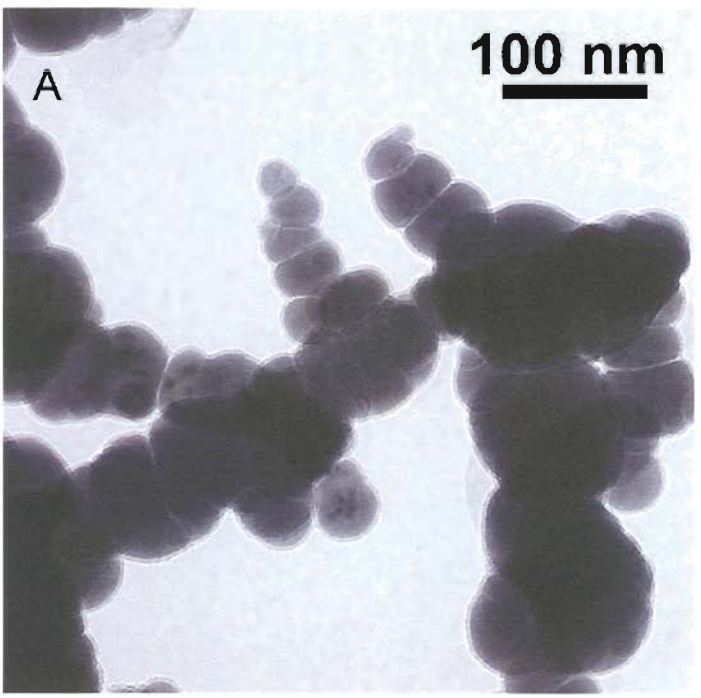

Figure 3.9 (B-C)

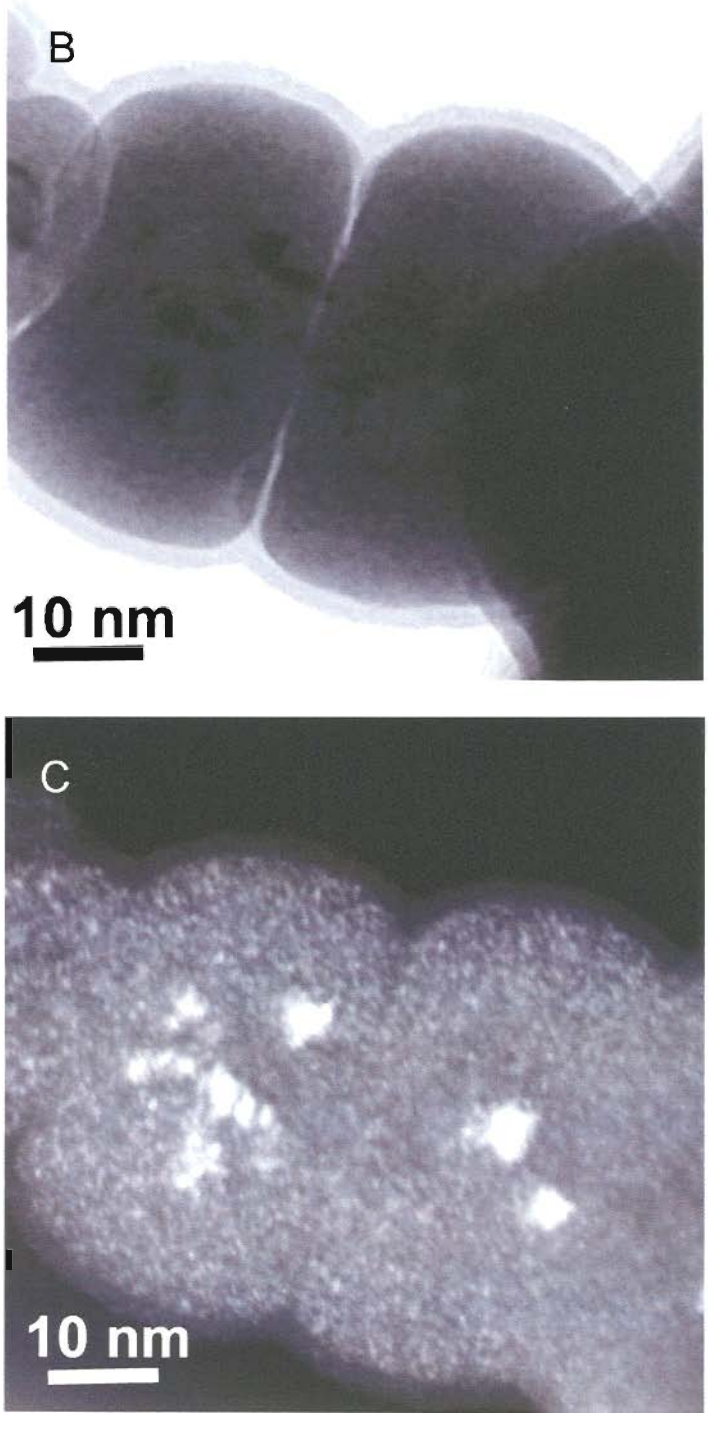

Figure 3.9 (D-E)

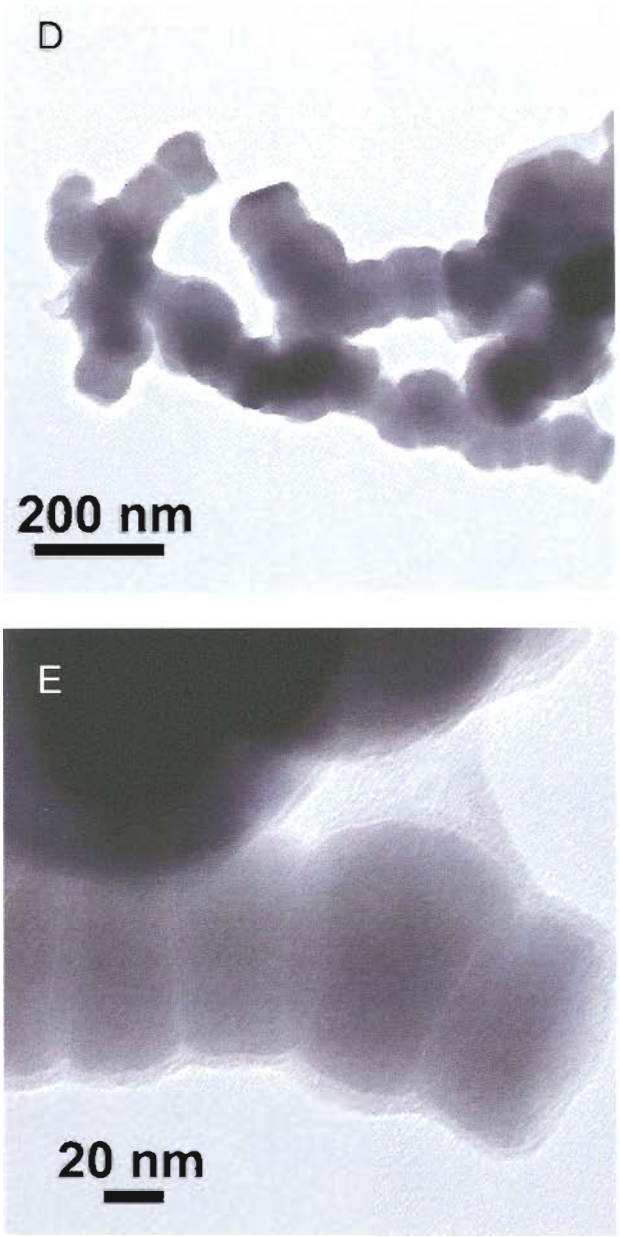

Figure 3.9. TEMs of Fe^{BH}. (A) Low magnification image of as-received sample, (B) Higher resolution image of metal particle, (C) Dark field image of metal particle highlighting small metal crystallites in particle, (D) Low resolution image of flash-dried sample. (E) higher resolution image of flash-dried sample showing spreading of coating layer between particles.

Figure 3.10

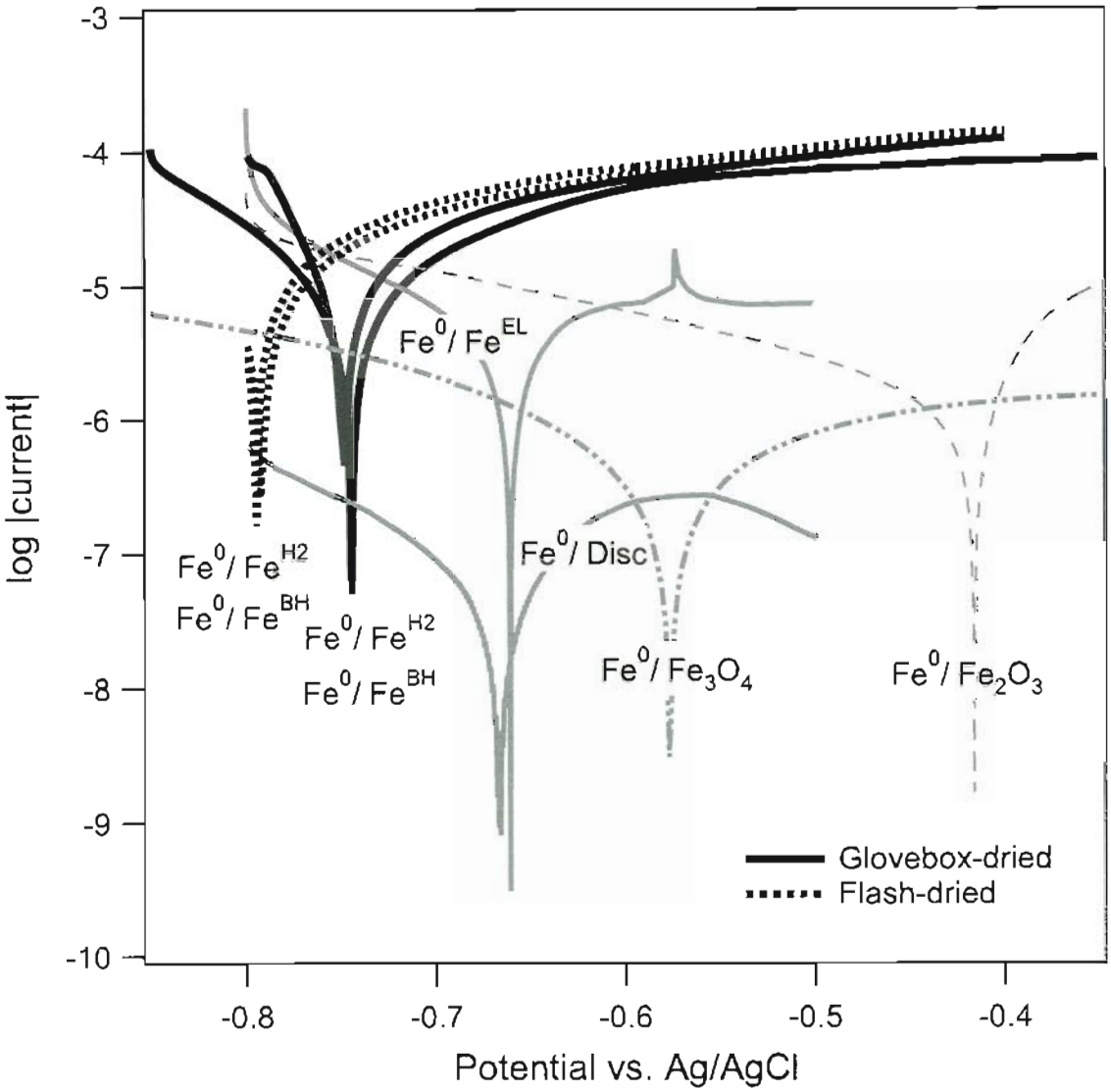

Figure 3.10. Log absolute current vs. potential plot from anodic polarization of stationary powder disk electrodes packed with various iron and iron oxide powders. At scan rate = 0.1 mV/s in anoxic aqueous borate (pH = 8.4).

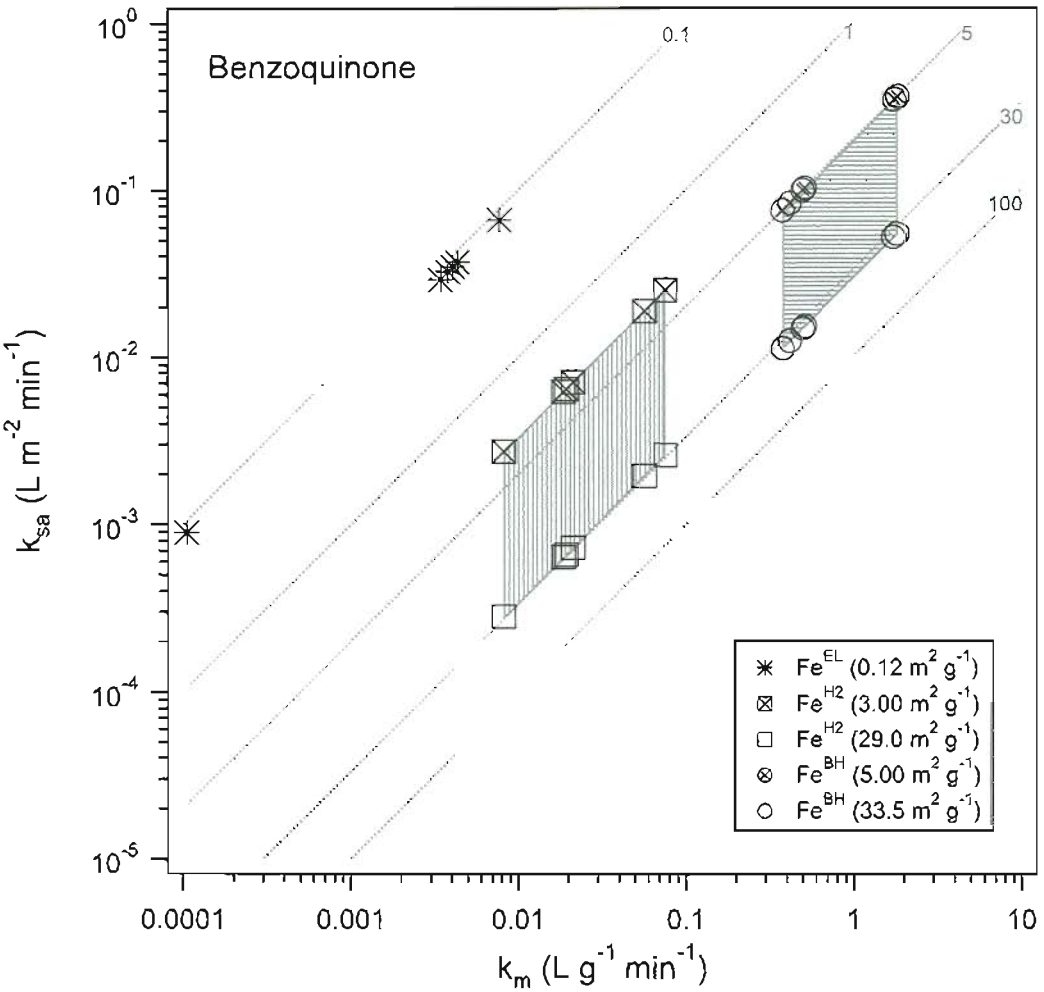

Figure 3.11. Surface area normalized rate constants (k_{SA}) vs. mass load normalized rate constants (k_M), for disappearance of benzoquinone (BQ) in batch experiments. Diagonal lines are contours for representative values of ρ_a (m^2 g^{-1}). For both types of nano-Fe^0, k_{SA} is shown for high and low ρ_a values (given in the legend). High values of ρ_a are from Table 3.1, Low values or ρ_a are BET measurements from this study. The resulting ranges of rate constants are shaded.

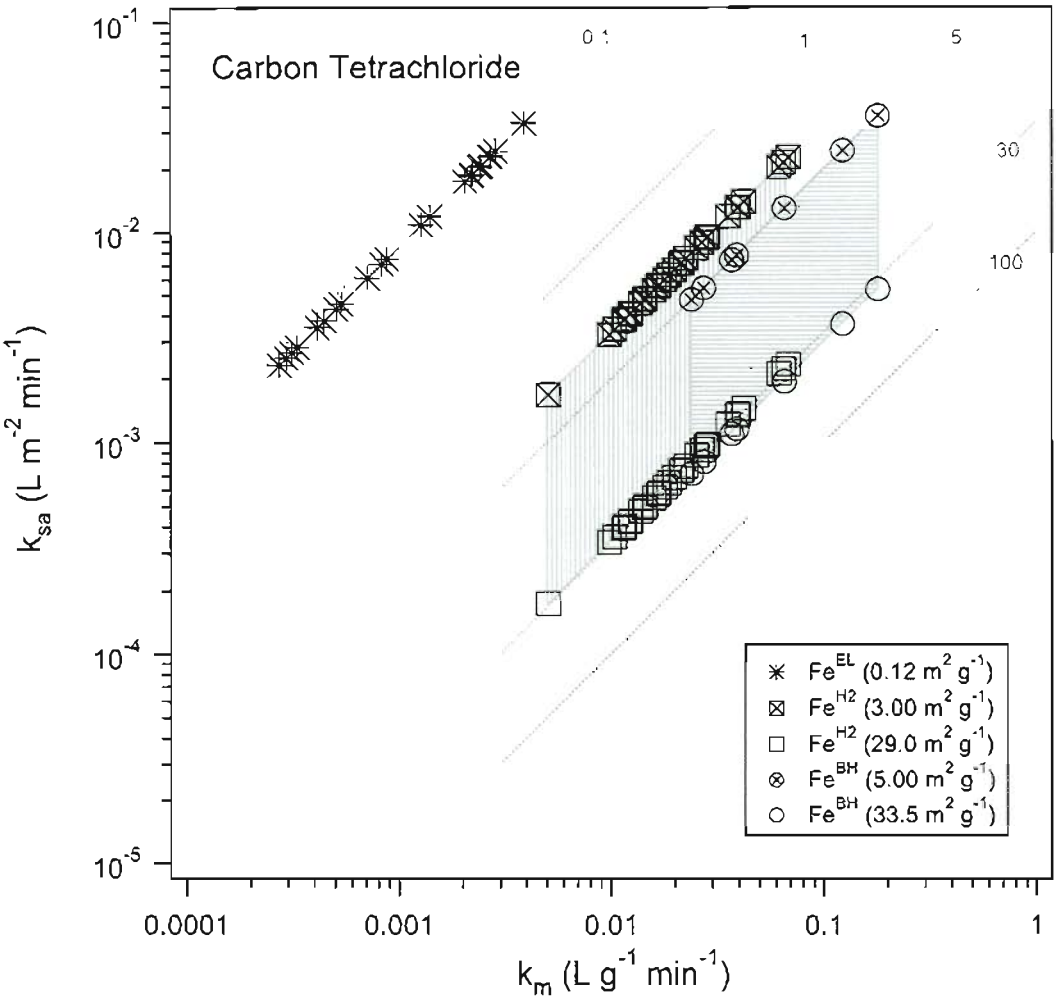

Figure 3.12. Surface area normalized rate constants vs. mass load normalized rate constants, for the disappearance of carbon tetrachloride (CT). Diagonal lines are contours for representative values of ρ_a (m^2 g^{-1}). For both types of nano-Fe^0, k_{SA} is shown for high and low ρ_a values (given in the legend). High values of ρ_a are from Table 3.1, Low values or ρ_a are BET measurements from this study. The resulting ranges of rate constants are shaded.

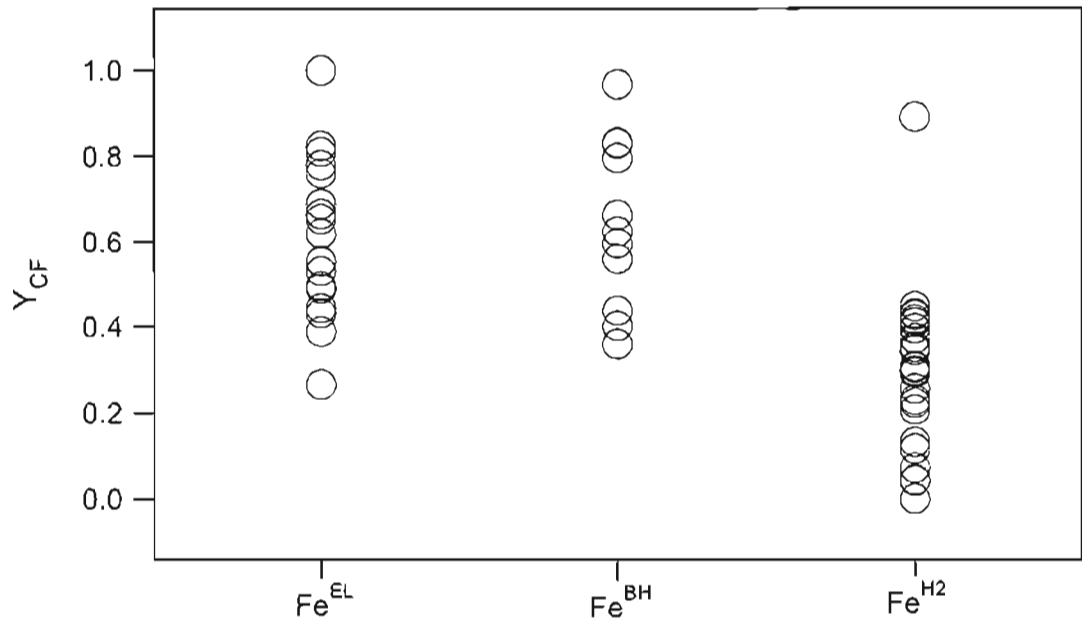

Figure 3.13. Yield of chloroform (Y_{CF}) vs. iron type (Fe^{EL}, Fe^{BH}, Fe^{H2}). The range of Y_{CF} for each iron type reflects the wide range of experimental conditions tested (pH, buffer, age and handling of the iron, etc.).

3.2.7. SUPPORTING INFORMATION

Characterization and Properties of Metallic Iron Nanoparticles: Spectroscopy, Electrochemistry, and Kinetics

James T. Nurmi, Paul G. Tratnyek, Vaishnavi Sarathy,
Donald R. Baer, James E. Amonette, Klaus Pecher, Chongmin Wang,
John C. Linehan, Dean W. Matson, R. Lee Penn, and Michelle D. Driessen

Figure S1. XRD patterns for as-received Fe^{H2} and Fe^{BH}.

Figure S2. TEMs showing beam damage of shell on Fe^{H2}.

Figure S3. Particle size distributions obtained from TEM.

Figure S4. XPS photoemission spectra for Fe^{H2} and Fe^{BH}.

Figure S5. L-edge XANES spectra from as-received Fe^{BH}, Fe^{H2}, and a Fe^{0} standard.

Figure S6. Anodic polarization voltammograms for stationary powder disk electrodes packed with Fe^{H2} that was dried and allowed to age under a glove-box atmosphere.

Figure S7. Anodic polarization voltammograms for stationary powder disk electrodes packed with Fe^{H2} that was flash-dried and then aged under a glove-box atmosphere.

Figure S8. Anodic polarization voltammograms for a stationary powder disk electrode packed with flash-dried Fe^{H2} as a function of pre-exposure time to aqueous borate.

Figure S9. TEMs of Fe^{H2} and Fe^{BH} after reaction with benzoquinone.

A.

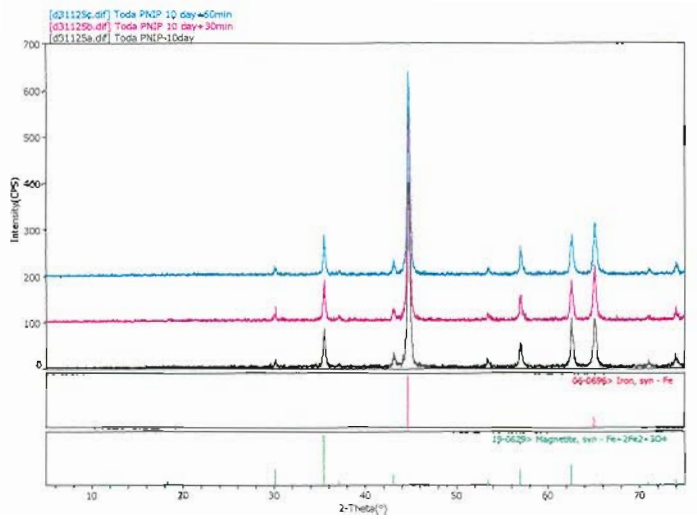

B.

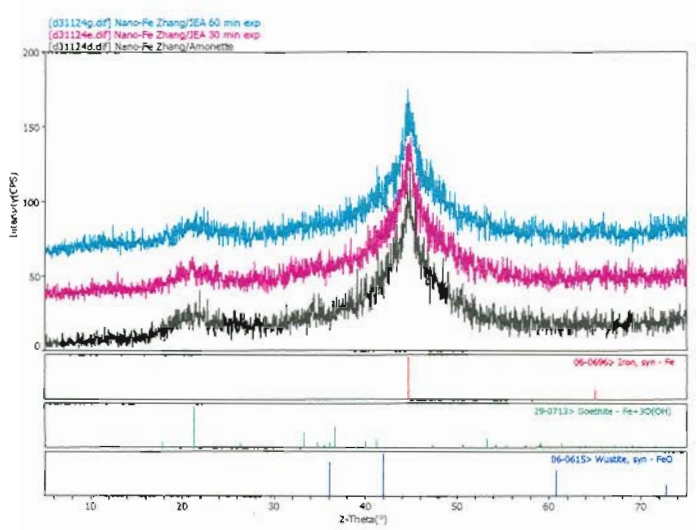

Figure S1. XRD patterns produced from as-received (A) Fe^{H2} and (B) Fe^{BH}. The narrow peaks from the Fe^{H2} are from both Fe^0 with a 30 nm grain size and magnetite with a 50 nm grain size. The metal-to-oxide ratio in this Fe^{H2} sample is about 70% metal and 30% oxide. In other samples the ratio is reversed. The diffraction peaks observed from the Fe^{BH} are from Fe^0 crystallites with an average crystallite or grain size of 1.5 nm.

A.

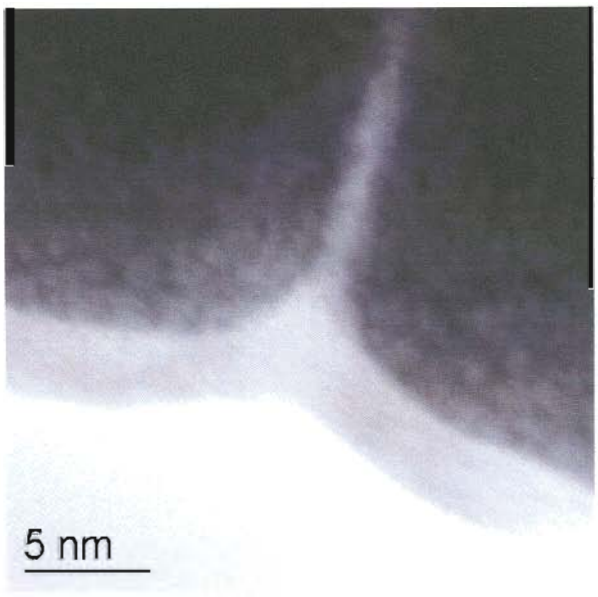

B.

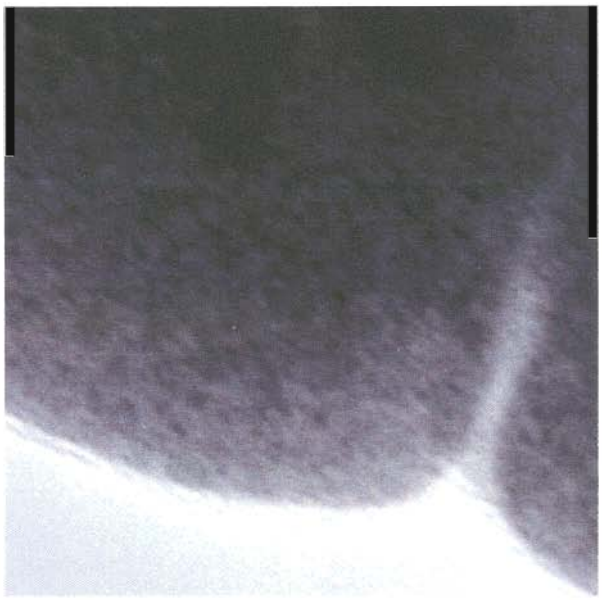

Figure S2. TEMs showing beam damage of shell on Fe^{BH}. Top: image taken as quickly as possible after loading. Bottom: after 1 min expsoure to the 200 V electron beam.

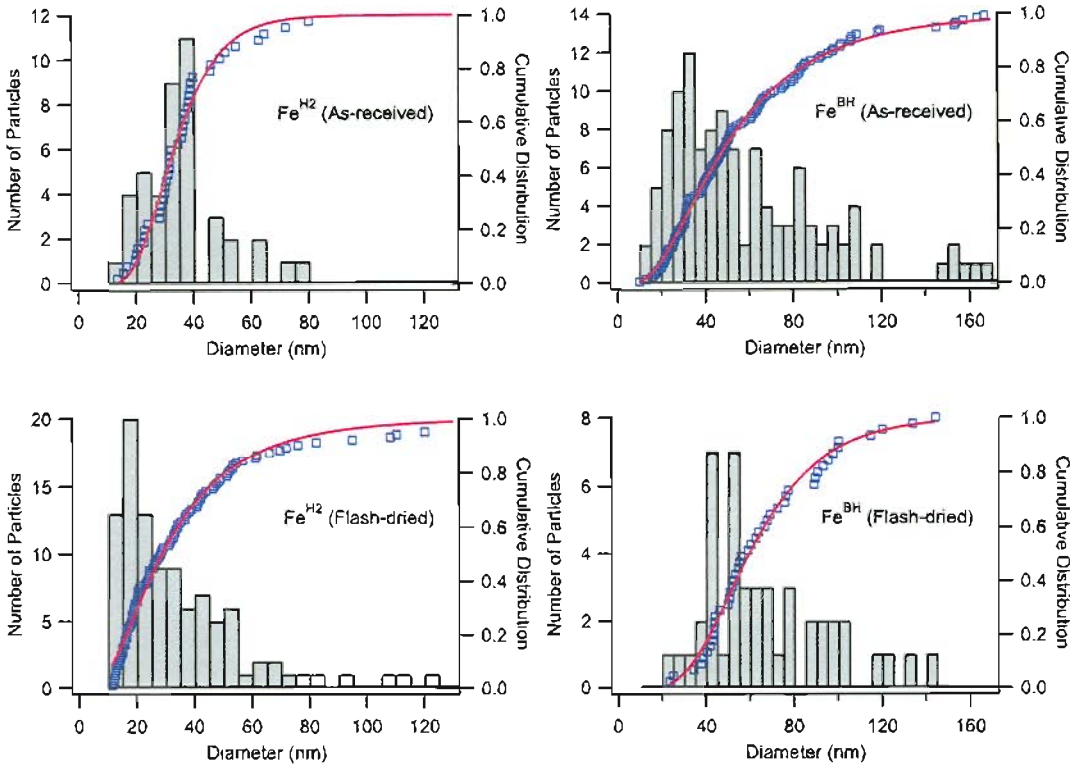

Figure S3. Particle size distributions obtained from TEM. Left axes (number of particles counted) go with the histograms. Right axes (cumulative distribution) go with the squares (individual particles measured) and the solid lines (fits of these data to a log-normal distribution function). In all cases, the log-normal distribution gave a better fit than a normal distribution (not shown).

A.

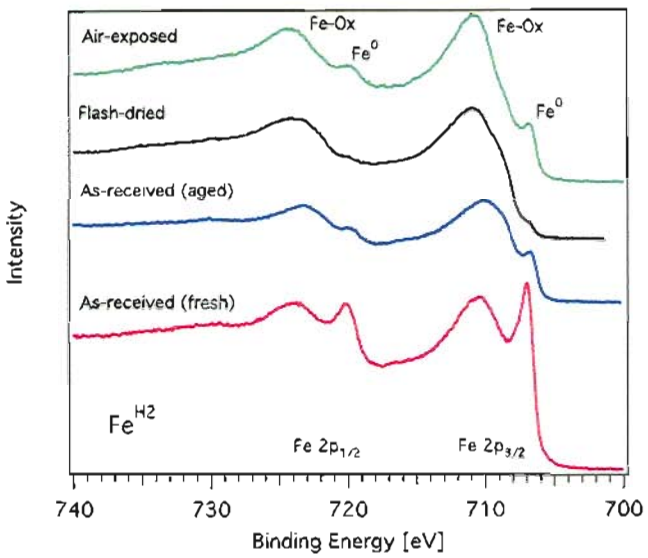

B.

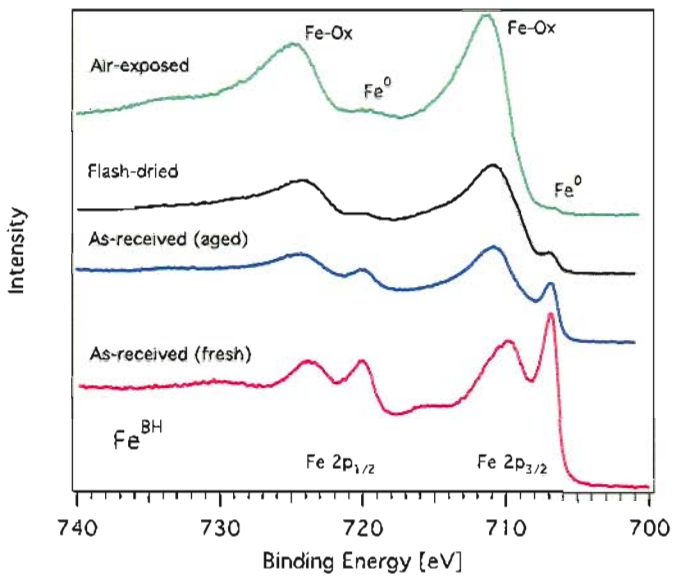

Figure S4. XPS photoemission spectra of the Fe $2p^{3/2}$ and $2p^{1/2}$ regions for Fe^{H2} (top) and Fe^{BH} (bottom). Binding energies are scaled to 707.0 eV for Fe^0. In most cases both metallic (Fe^0) and oxide states (Fe-Ox) are observed, consistent with an oxide coating on a metallic core.

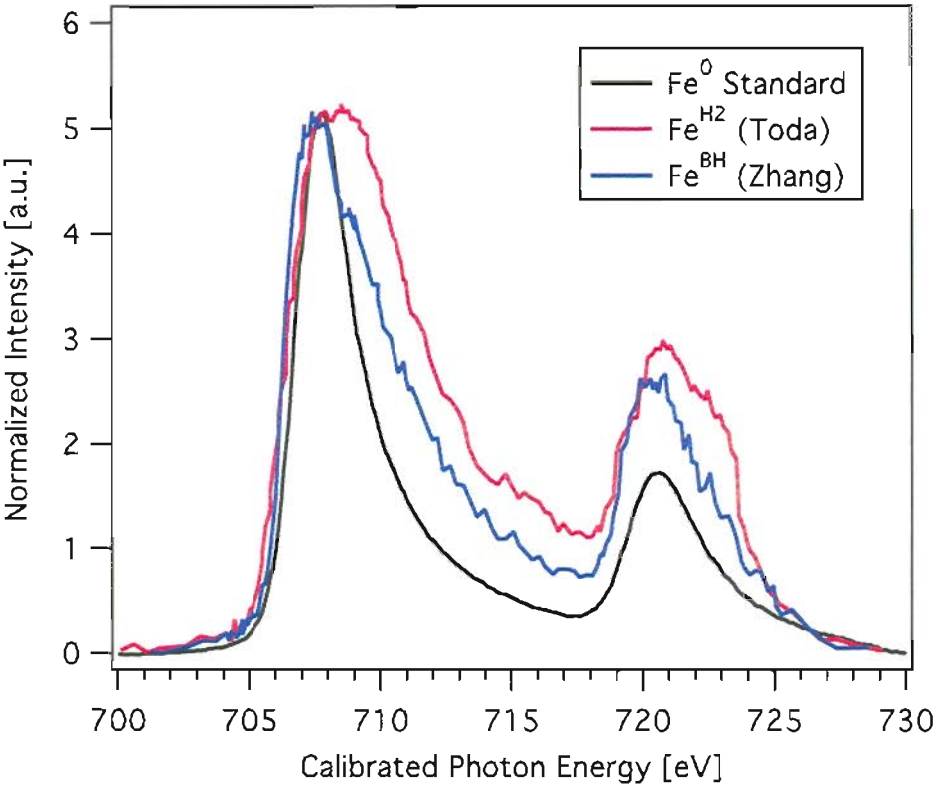

Figure S5. Area averaged L-edge XANES extracted from STXM and TEY (Total Electron Yield) measurements produced from as-received Fe^{BH}, Fe^{H2}, and a Fe^{0} standard. (Fe^{0} standard spectrum provided by T. Droubay).

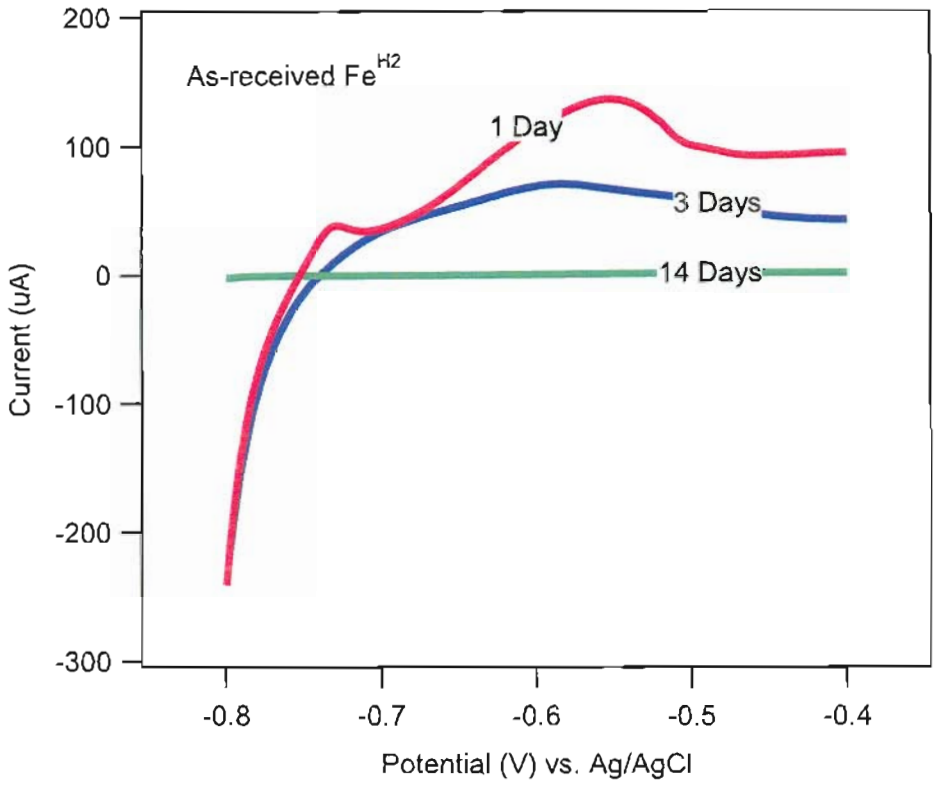

Figure S6. Anodic polarization voltammograms for stationary powder disk electrodes packed with Fe^{H2} that were dried and allowed to age under a glove-box atmosphere. At scan rate = 0.1 mV/s in anaerobic aqueous borate (pH = 8.4).

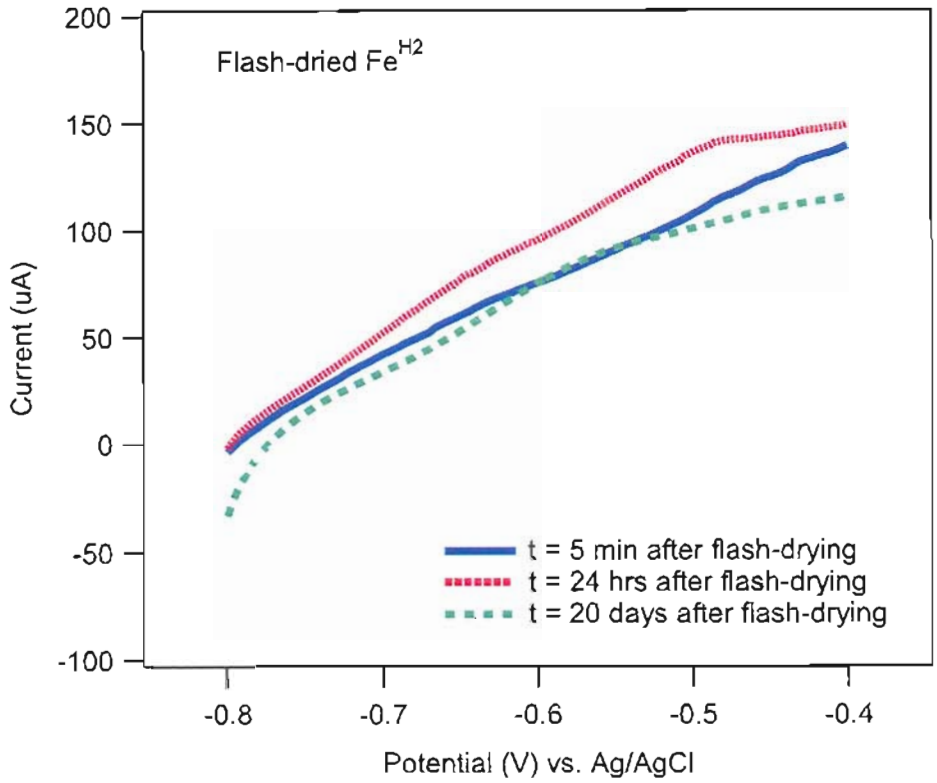

Figure S7. Anodic polarization voltammograms for stationary powder disk electrodes packed with Fe^{H2} that was flash-dried and then aged under a glove-box atmosphere. At scan rate = 0.1 mV/s in anaerobic aqueous borate (pH = 8.4).

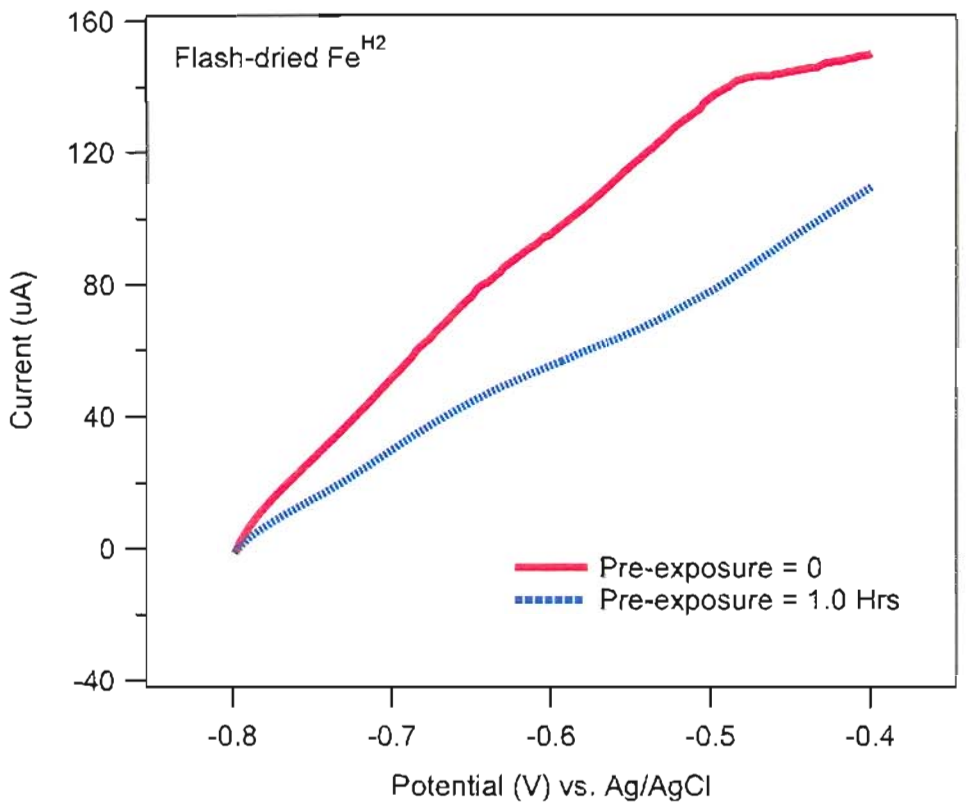

Figure S8. Anodic polarization voltammograms for a stationary powder disk electrode packed with flash-dried Fe^{H2} as a function of pre-exposure time to aqueous borate. At scan rate = 0.1 mV/s in anaerobic aqueous borate (pH = 8.4).

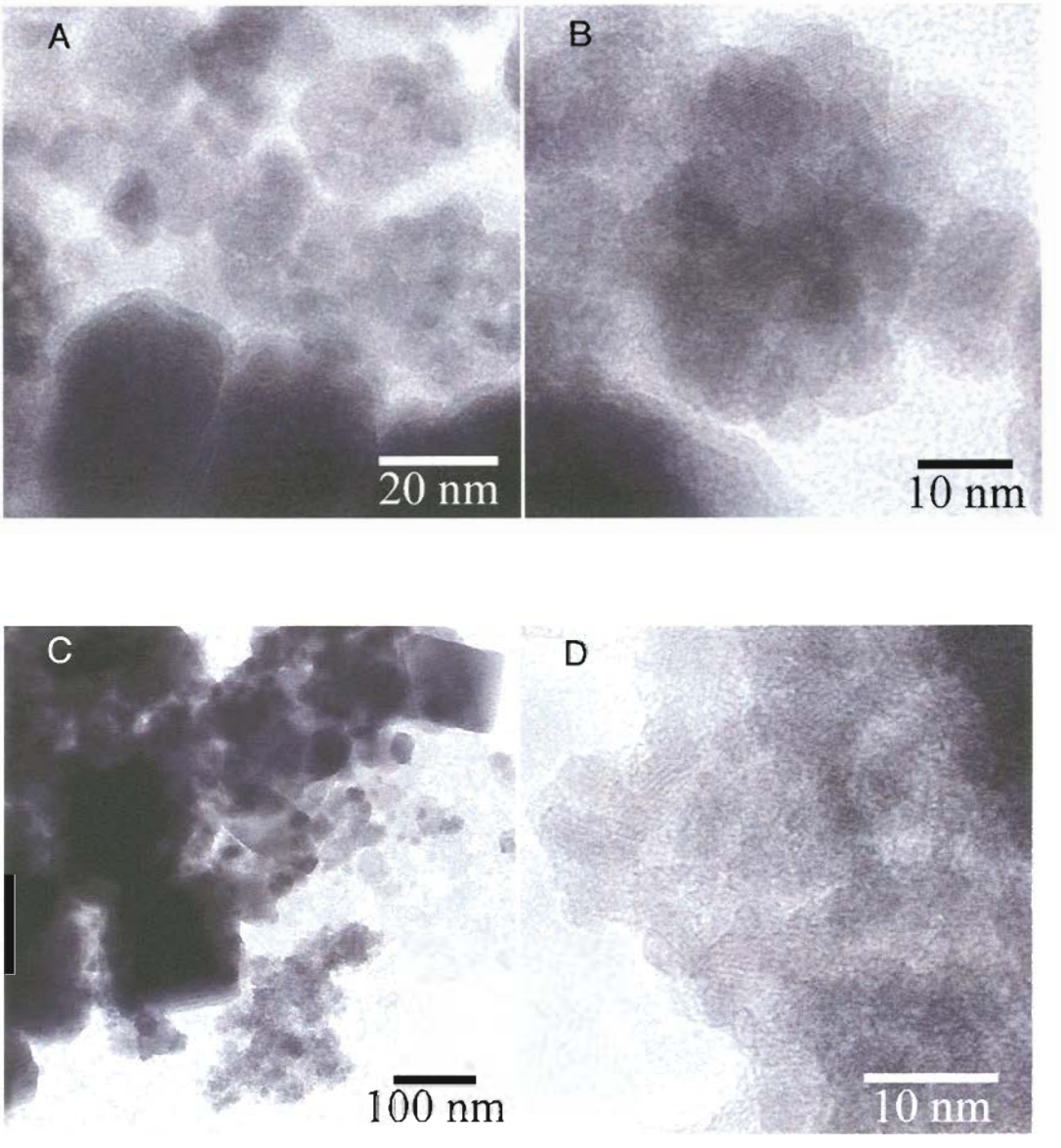

Figure S9. TEMs after reaction with benzoquinone: (A-B) Fe^{BH}, (C-D) of Fe^{H2}. For both types of iron, two types of material are observed after the reaction: larger particles that appear essentially unaltered, and smaller oxide particles, which are shown at higher magnification in B and D. Diffraction patterns taken from the smaller particles produced from Fe^{BH} are consistent with maghemite/magnetite and goethite and from Fe^{H2} are consistent with magnetite/maghemite.

Biographical Sketch

Jim was born in Springfield, MA on March 14th, 1975. Before turning two, his parents packed a red pickup truck with a dog and two beehives and settled in Hastings, MN. In 1997, Jim graduated from Gustavus Adolphus College with a B.A. in Biology. He went to work at Argonne National Laboratory working with a novel ceramic called Ceramicrete which was being used to physically and chemically stabilize low-level mixed wastes. Jim then moved to Oregon in 1999 and started a non-thesis masters program at OGI, got married to Amber Shockey, and adopted a couple of cats and a dog. After working with Himalayan blackberries and tobacco smoke, he ended up in Dr. Paul G. Tratnyek's lab studying the electrochemical properties of natural organic matter and iron particles. Months prior to defending his dissertation, Jim and Amber had a son whose name is James Daniel Nurmi. Jim successfully defended his PhD dissertation on September, 28th, 2005. Jim's awards and publications include;

2003 Graduate Student Paper Award, Division of Environmental Chemistry, American Chemical Society

2003 Paul Clayton Student Award, OGI School of Science and Engineering, Oregon Health & Science University

2001 Graduate Student Award in Environmental Chemistry, Division of Environmental Chemistry of the American Chemical Society.

Nurmi, J. T.; Tratnyek, P. G. Electrochemical properties of natural organic matter (NOM), fractions of NOM, and model biogeochemical electron shuttles *Environ. Sci. Technol.* **2002**, *36*, 617-624.

Nurmi, J. T.; Bandstra, J. Z.; Tratnyek, P. G. Packed powder electrodes for characterizing the reactivity of granular iron in borate solutions *J. Electrochem. Soc.* **2004**, *151*, B347-B353.

Nurmi, J. T.; Tratnyek, P. G.; Sarathy, V.; Baer, D. R.; Amonette, J. E.; Pecher, K.; Wang, C.; Linehan, J. C.; Matson, D. W.; Penn, R. L.; Driessen, M. D. Characterization and properties of metallic iron nanoparticles: spectroscopy, electrochemistry, and kinetics *Environ. Sci. Technol.* **2005**, *39*, 1221-1230.